FACULTE DES SCIENCES
Institut de Physique des Hautes Energies (IPHE)

A luminosity monitor for LHC

Thèse de doctorat

présentée à la

Faculté des Sciences de
l'Université de Lausanne

par

Anne-Laure Perrot

Ingénieur physicien
Ecole Polytechnique Fédérale de Lausanne

Jury

Prof. Jean-Claude Bünzli, Président
Prof. Aurelio Bay, Directeur de thèse
Dr. Sylvain Weisz, Expert
Dr. Léonard Studer, Expert

LAUSANNE
2001

To
my parents,
my brother, Jean-Philippe and my sister, Isabelle

Abstract

The Large Hadron Collider (LHC) under construction at CERN will give high luminosities to experiments covering six orders of magnitude from of 10^{28} $cm^{-2}s^{-1}$ to 10^{34} $cm^{-2}s^{-1}$. A new approach is needed to measure the LHC luminosity. This work reports the study of a LHC luminosity monitor based on the concept of Secondary Emission Chamber (SEC). The main request for such a detector is to cover the six orders of magnitude of the LHC luminosity range. Its precision is expected to be of the order of 2 %. The TOTEM collaboration proposes to calibrate the monitor at low luminosity.

The construction of the detector based on the previous SECs developed years ago at CERN is presented. The performances of the new prototype are determined for incident currents between ~10^{-12} A and 10^{-13} A. The tests lead to conclude that at the LHC the SEC will be able to measure luminosity with a precision of 3 % within 1 s for luminosity above 10^{31} $cm^{-2}s^{-1}$. A conversion of the SEC into an Ionisation Chamber (IC) is proposed to cover the LHC low luminosity region. It is achieved by filling the SEC with argon at atmospheric pressure. The IC response is found to be linear with the foreseen precision over the full experimental range of intensity corresponding to currents between 10^{-15} A and 10^{-12} A. The linear continuity between the responses of the monitor in the SEC and the IC modes is observed.

We propose to use, at the LHC, the detector in the IC mode at low luminosity and in the SEC mode at high luminosity with a switch in mode at a luminosity of ~ 10^{31} $cm^{-2}s^{-1}$.

Résumé

Ce travail consiste à étudier si un détecteur basé sur le concept des chambres à émission secondaire (SEC) pourra être employé pour la mesure de la luminosité du futur LHC (Large Hadron Collider). Dans ce contexte, le détecteur devra couvrir une gamme de six ordres de grandeur i.e. des luminosités allant de 10^{28} $cm^{-2}s^{-1}$ à 10^{34} $cm^{-2}s^{-1}$ et devra résister au champs de rayonnement intense engendré lors du fonctionnement de la machine. Il est prévu de l'installer dans la caverne expérimentale de CMS (Compact Muon Solenoid), autour du tube à vide, à 19 mètres du point d'interaction et dans un domaine de pseudo-rapidité s'étendant de 5 à 7. Dans ces conditions expérimentales, la SEC devra être sensible à des courants minimum de l'ordre de 10^{-15} A. L'expérience TOTEM qui sera insérée dans CMS propose de calibrer le détecteur dont la précision de mesure est espérée atteindre les 2 %.

Comme les SECs utilisées au CERN possèdent un seuil de détection de l'ordre de 10^{-12} A, de nouveaux prototypes ont été construits dans l'optique d'abaisser cette limite et, en particulier, de minimiser les courants de fuite, les boucles de masse et différents bruits d'origine électronique. La conception et l'élaboration de ces prototypes sont basés sur ceux des précédentes SECs. Deux améliorations notables ont été apportées. L'ajout, à l'intérieur du tank à vide, d'un cylindre d'acier inoxydable isolé de la terre et l'utilisation de connexions triaxiales. Ainsi, maintenant, le tank externe joue le rôle de cage de Faraday et isole efficacement les électrodes du bruit électromagnétique externe. Le cylindre intérieur, quant à lui, constitue pour les électrodes un 'bouclier flottant' par rapport à la terre. Deux prototypes ont été développés. La résistivité du second prototype a été augmentée afin d'abaisser le courant de fuite du détecteur au-dessous de 10^{-15} A. Dans cette dernière version, le seuil de détection du moniteur est limité par le bruit électronique et non pas par le courant de fuite de la chambre elle-même

La nouvelle SEC a été testée en comparant sa réponse à celle d'un détecteur de référence, sur les lignes d'extraction du PS et du SPS du CERN pour des intensités allant de $5\ 10^5$ à $6\ 10^7$ particules incidentes par extraction correspondant à des courants incidents de l'ordre de ~ 10^{-13} A à ~ 10^{-12} A. Au-dessus de $3\ 10^6$ particules incidentes par extraction la réponse de la SEC est linéaire et entachée d'une erreur maximale de 3 %. Le calcul montre que la SEC pourra au LHC mesurer des luminosités supérieures à 10^{31} $cm^{-2}s^{-1}$ avec une incertitude de 3 %.

Afin de couvrir la région des basses luminosités, la SEC est convertie en chambre à ionisation (IC) par remplissage avec de l'argon à pression atmosphérique. Les performances de la IC ont été déterminées dans des conditions expérimentales semblables à celles des tests de la SEC. La réponse de la IC est linéaire sur la gamme d'intensité à disposition i.e. entre $9\ 10^4$ et $6\ 10^7$ particules incidentes par extraction correspondant à des courants de l'ordre de 10^{-15} A à 10^{-12} A avec une incertitude de l'ordre recherché.

La transition entre les modes IC et SEC a été étudiée. Il sera possible connaissant la réponse du détecteur à basse luminosité d'extrapoler la normalisation à haute luminosité.

En conclusion, le détecteur pourra fonctionner au LHC en mode IC à basse luminosité et en mode SEC à haute luminosité avec l'électronique actuelle. Le changement de régime IC-SEC sera effectué à une luminosité de l'ordre de 10^{31} $cm^{-2}s^{-1}$.

Summary

The main goal of this work was to study if a detector based on the concept of Secondary Emission Chamber (SEC) could be used as a luminosity monitor for the Large Hadron Collider (LHC). The requests for such a monitor (not fulfilled by the actual detectors) are a dynamic range of six orders of magnitude which extends from a luminosity of 10^{28} $cm^{-2}s^{-1}$ to 10^{34} $cm^{-2}s^{-1}$ and a good tolerance to the LHC radiation. Our monitor will be installed at 19 meters from the interaction point 5 (CMS experimental Hall) surrounding the vacuum tube in the pseudo-rapidity range from 5 to 7. For these experimental conditions, calculations show that the SEC should be able to detect minimum currents of ~ 10^{-15} A. The TOTEM experiment which will be inserted inside the CMS experiment proposes to calibrate the monitor at low luminosity by means of the "luminosity independent method". The uncertainty of the monitor is expected to be close to 2 %.

The detection threshold of SECs used at CERN is about 10^{-12} A. Thus, new prototypes have been built in view to improve this parameter and, in particular, to minimise leakage currents, mass loops and various electronic noise pick-ups. Their conception and design are based on those of previous SECs with two main upgrades. First, the addition of a ground insulated stainless steel cylinder inside the vacuum tank. Second, the use of triaxial connections. With this set-up the external tank acts as a Faraday cage, it isolates the electrodes from the external electromagnetic noise while the internal cylinder acts as a "floating" shield. Two prototypes have been built. They differ by the insulation between consecutive electrodes. The resistivity has been increased in the second version in view to minimise the leakage current. This last is estimated to be now less than 10^{-15} A. The limitation of the SEC response comes only from the associated electronics.

The performances of the new prototype were determined comparing its response with a reference detector. Tests were carried out at CERN on the PS and the SPS extraction beam lines with intensity between 5 10^{5} and 6 10^{7} incident particles per burst corresponding to incident current of the order of 10^{-13} A and 10^{-12} A. Above 3 10^{6} incident particles per burst corresponding to an incident current of ~10^{-13} A, the SEC response is a linear function of the number of incident particles and its uncertainty is lower than 3 %. At the LHC, calculation shows that the SEC will be able to measure the luminosity with a precision of ~ 3 % within 1 s for luminosity above 10^{31} $cm^{-2}s^{-1}$.

A conversion of the SEC into an Ionisation Chamber (IC) is proposed to cover the LHC low luminosity region. We have transformed the SEC into IC by filling the chamber with argon at atmospheric pressure. The performances of the IC monitor have been determined in the same experimental conditions as for the SEC. The IC response is linear over the full available experimental range of incident particles i.e. from 9 10^{4} to 6 10^{7} incident particles per burst corresponding to incident current of the order of 10^{-15} A and 10^{-12} A. Its uncertainty is ~ 1 %.

Some runs were dedicated to the transition from the SEC to the IC mode. Knowing the monitor response at low luminosity it should be possible to extrapolate the calibration to high luminosity.

In conclusion, as LHC luminosity monitor, our detector with the actual electronics can be used in IC mode at low intensity and in SEC mode at high intensity with a switch at a luminosity of ~10^{31} $cm^{-2}s^{-1}$.

Contents

List of symbols

Latin letters

$( )^*$	Value at the interaction point
A	Area
	Atomic weight
A_{eff}	Effective area
A_i	Radioactivity
$\vec{B}$	Magnetic field vector
c	Light velocity
	Capacity
C	Machine circumference
D	Diffusion coefficient
e	Elementary charge
eV	Electron volt
E	Energy
	Electric field strenght
$\vec{E}$	Electric field vector
f	Frequency
f_{RF}	Radio frequency cavity frequency
F	Reduction factor caused by crossing angle
$\vec{F}$	Force vector
G	Gain
h	Harmonic number
	Vertical separation between beams
h_{eff}	Effective height of beam collision
I	Current
I_b	Circulating current/beam
Im( )	Imaginary part
J	Current density
k	Bunch number
k^+	Positive charge mobility
l	Lenght
L	Luminosity
m	Mass
n^+, n^-	Positive, negative charged densities
N	Particle number
	Particle density
N_{el}	Elastic rate
N_{inel}	Inelastic rate

p	Particle relativistic momentum
p-p	proton-proton
P_i	Radionucleid period
P	Pressure
P( )	Poisson distribution
Q	Machine tune
r.m.s.	Root mean square
R	Reaction rate
R^2	Correlation factor
Re( )	Real part
R_T	Total rate
s	Longitudinal particle coordinate
t	Momentum transfer
	Time
t_{irr}	Irradiation time
T_i	Activation period
v	Particle velocity
V	Voltage
W_i	Ionisation energy
x, z	Horizontal, vertical (respectively) transverse particle coordinate
x', z'	Horizontal, vertical (respectively) divergence angle
Z	Atomic number

Greek letters

η	Pseudo-rapidity
β	Betatron function
	v/c, relativistic velocity factor
σ	Cross section
	Standard deviation
σ_{tot}	Total cross section
σ_x, σ_z	Horizontal, vertical (respetively) beam r.m.s. radius
ρ	Density
	Charge density
	ReF(0)/ImF(0) i.e. real to imaginary part of the forward elastic amplitude
	Radius of curvature
	Resistivity
γ	Relativistic mass factor
ε	Beam emittance
	Detector efficiency
ε_0	Space permitivity
ε_n	Normalised transverse beam emittance
α	Angle (often used in accelerator for beams crossing angle)
	Recombination coefficient
α_r	Recombination coefficient

δ	Efficiency or yield (detector)
λ	Mean free path
μ	Mobility (for particle)
ϕ	Flux
ϕ_s	Synchronous particle phase
$\phi(t)$	Particle phase at time t
$\Delta(\ )$	Interval value
τ	decay time

Acronyms

ALICE	A Large Ion Collider Experiment
ATLAS	A Toroidal LHC ApparatuS
CDF	Collider Detector at Fermilab
CERN	European organisation for nuclear research
CESR	Cornell Electron Storage Ring
CMS	Compact Muon Solenoid
CP	Charge conjugaison, Parity
CTM-10	Counter Timer Monitor-10
EBCR	East Beam Control Room
ECAL	Electromagnetic CALorimeter
FET	Field Effect Transistor
FWHM	Full Width at the Half Maximum
HCAL	Hadronic CALorimeter
HV	High Voltage
IC	Ionisation Chamber
IP	Interaction Point
ISR	Intersecting Storage Rings
LEP	Large Electron Positron collider
LHC	Large Hadron Collider
LHCb	Large Hadron Collider beauty experiment
MSGC	MicroStrip Gas Chamber
MWPC	Multi-Wire Proportional Chamber
PIC	Precision Ionisation Chamber
PM	PhotoMultiplier
PS	Proton Synchrotron
RF	Radio Frequency
RHIC	Relativistic Heavy Ion Collider
SEC	Secondary Emission Chamber
SEE	Secondary Electron Emission
SEM	Secondary Emission Monitor
SPS	Super Proton Synchrotron
SNR	Signal to Noise Ratio
TOTEM	TOTal and Elastic Measurement
UHV	Ultra High Vacuum
UV	Ultraviolet

Introduction

CERN is building a new accelerator, the Large Hadron Collider (LHC). Due to switch on in 2005, it will collide beams of protons with energies of 7-on-7 TeV and provide beam crossing points of unsurpassed brightness and thus experiments with high interaction rates and luminosity. Whereas in past and present colliders the luminosity culminates around 10^{32} $cm^{-2}s^{-1}$, in the LHC it will reach 10^{34} $cm^{-2}s^{-1}$ providing in particular the opportunity to look for the rare Higgs boson and "supersymmetric" particles. The most important parameter of the LHC, apart from the energy of the colliding beams, will be its luminosity. The luminosity relates the reaction rate of a process to its cross-section and is of most immediate interest for the high energy physicists as it allows them to normalise their measurements. For the people running the machine, the luminosity measurement permits them to optimise the beams collisions and the machine performances.

However, the precise measurement of the luminosity, L, is difficult on this p-p collider. A direct evaluation with the beam parameters (intensity and emittance) or with the "van der Meer" method developed twenty years ago at the proton-proton ISR collider will lead to a great uncertainty. The TOTEM (TOTal and Elastic Measurement) collaboration will measure the p-p cross-section with high precision using the "luminosity independent method". It proposes to calibrate a LHC luminosity monitor around $10^{28}cm^{-2}s^{-1}$. The challenge for such a detector is the coverage of the dynamic range of six orders of magnitude (L between 10^{28} $cm^{-2}s^{-1}$ and 10^{34} $cm^{-2}s^{-1}$). Planned to be installed close to the interaction point in the CMS cavern with the TOTEM experiment, such a monitor must provide a good tolerance to radiation. As these requirements are not fulfilled by detectors currently in use, it is proposed to study whether a detector based on the concept of Secondary Emission Chamber (SEC) developed years ago and still in use at CERN could be a luminosity monitor for LHC.

After an introduction to the experimental environment of the future luminosity monitor, the luminosity is defined. Different techniques for the evaluation of the luminosity are presented. The need of a new monitor luminosity for the LHC is then explained at the end of chapter 1. Chapter 2 introduces briefly the physics of accelerators

and gives the general characteristics of particles detectors. The principles of Ionisation Chamber (IC) and Secondary Emission Chamber (SEC) are explained in chapter 3. There, the construction of a new prototype, its improvements with respect to the SECs used at the PS and the SPS and the associated electronics are reported. Chapter 4 reports the experimental set-up with specifications on the beam lines used during the tests and the acquisition system whilst chapter 5 presents the setting of a reference detector dedicated to the calibration of the new prototype. The settings and performances of the new prototype working as SEC are reported in chapter 6, in particular, its linearity as function of the number of incident particles, its yield and its saturation threshold. The SEC is converted in IC by filling it with argon at atmospheric pressure. The performances of the IC are reported in chapter 7. Finally, the transition between SEC and IC modes and some performances of the prototype as a LHC luminosity monitor are discussed.

Chapter 1 Introduction to experimental environment

1.1 CERN: the european laboratory for particle physics

At CERN and in many other high-energy physics laboratories, particle beams are used to probe the heart of matter and take us back to the beginning of time, the Big Bang. By accelerating particles to very high velocities and smashing them onto targets, or into each other (in colliders), physicists can unravel the forces acting between them and produce new particles[1]. In the quest for higher interaction energies, CERN has played a leading role in developing colliding beams machines. Notable "firsts" were the Intersecting Storage Rings (ISR) proton-proton collider commissioned in 1971, and the proton-antiproton collider at the Super Proton Synchrotron (SPS), commissioned in 1976, which produced the massive W and Z particles two years later, confirming the unified theory of electromagnetic and weak forces. At the Large Electron Positron collider (LEP), stopped at the beginning of December 2000, measurements unsurpassed in quantity and quality have tested our best description of sub-atomic Nature, the Standard Model, to a fraction of 1% soon to reach one part in a thousand. By 1996, the LEP energy was doubled to 90 GeV per beam in LEPII and then increased in 2000 until 104 GeV opening up an important new discovery domain. Data from the LEP experiments are so accurate that they are sensitive to phenomena that occur at energies beyond those of the machine itself [2]. All evidence indicates that new physics, and answers to some of the most profound questions of our time, lie at energies around 1 TeV. The current description of matter and force, the so-called Standard Model, has withstood experimental testing for twenty years. It leaves many questions unanswered. Why do particles have mass? Are the forces of Nature just different aspects of the same thing? Is there really no antimatter left in the Universe? CERN is building a new accelerator, the Large Hadron Collider (LHC) which will probe deeper into matter than ever before to tackle these important questions [1]. It will recreate the conditions prevailing in the Universe just 10^{-12} second after the Big Bang when the temperature was 10^{16} degrees. It will reveal behaviour of fundamental particles of matter that has never been studied

before. The aim is to produce, not only high energy but a higher luminosity, or probability of collision, than existing hadrons colliders [3]. This challenging machine is designed to use the actual 27 kilometres LEP tunnel and be fed by existing particle sources and pre-accelerators. It will use the most advanced superconducting magnet and accelerator technologies ever employed.

1.1.1 LHC, accelerator environment of the monitor

Due to switch on in 2005, the LHC will ultimately collide beams of proton with energies of 7-on-7 TeV and provide beam crossing points of unsurpassed brightness and thus experiments with high interaction rates. Beams of lead nuclei will also be accelerated, smashing together with a collision energy of 1250 TeV, about thirty times higher than at the Relativistic Heavy Ion Collider (RHIC) been commissioned at the Brookhaven Laboratory in the USA. In these last collisions a large energy density could be obtained over a wide enough region to cause phase transition of nuclear matter into quark-gluon plasma.

For LHC there are many challenges in accelerator physics among which the high luminosity, the fact that the beam-beam effect limits the bunch density, the control of the collective instabilities, the long time stability of the beam, the prevention of the magnets quenching, the flexibility of the lattice and the significant synchrotron radiation.

In the LHC the energy available in the collisions between the constituents of the protons (the quarks and gluons) will reach the TeV range, that is about 10 times that of LEP and of the Fermilab Tevatron. In order to maintain an equally effective physics programme at a higher energy, E, the luminosity of a collider (a quantity proportional to the number of collisions per second) should increase in proportion to E^2. This is because the De Broglie wavelength associated to a particle decreases as 1/E and hence the cross-section of the particle decreases as $1/E^2$. Whereas in past and present colliders the luminosity culminates around $L=10^{32}cm^{-2}s^{-1}$, in the LHC it will reach $L=10^{34}cm^{-2}s^{-1}$. This will be achieved by filling each of the two rings with 2835 bunches of 10^{11} particles each. This resulting large current (I_b=0.53 A) is a particular challenge in a machine made of sensitive superconducting magnets operating at cryogenic temperatures.

A limit to luminosity comes from the beam-beam effect. When two bunches cross in the interaction point only a tiny fraction of the particles collide head-on to produce the wanted events. All the other particles undergo the strong electromagnetic field from the opposing bunch. The machine tune is increased, one speaks of “tune spread” (see § 2.1). This and the effects due to the instabilities and resonances along the lattice lead to a beam loss turn after turn. This beam-beam effect was studied in previous colliders, where experience showed that one cannot increase the bunch density beyond a certain beam-beam limit to preserve a sufficiently long beam lifetime. In order to reach the desired luminosity the LHC has to operate as close as possible to this limit. Its injectors, the Proton Synchrotron (PS) and the Super Proton Synchrotron (SPS), are being refurbished to provide the required beam density.

While travelling along the LHC beam pipe at a speed close to the speed of light, each of the 2835 proton bunches leaves behind an electromagnetic wake-field which perturbs the succeeding bunches. In this way any initial disturbance in the position or energy of a bunch is transmitted to its companions, and under certain phase conditions their oscillations can be amplified and lead to beam loss. These collective instabilities can be severe in the LHC because of the large beam current needed to provide high luminosity. Their effect is minimised by the control of the electromagnetic properties of the elements surrounding the beam.

The beam will be stored at high energy for about 10 hours. During this time the particles will make four hundred millions revolutions around the machine. Meanwhile the amplitude of their natural oscillations around the central orbit should not increase significantly, because this would dilute the beam and degrade the luminosity. This is difficult to achieve since, in addition to the beam-beam interaction, tiny spurious non linear components of the guiding and focusing magnetic fields of the machine can render the motion slightly chaotic, so that after a large number of turns the particles may be lost. For the time being, despite theories describing beam stability in accelerators, no one permits an analytical calculation. Instead fast computers track hundreds of particles step by step through the thousands LHC magnets for up to a million turns. Results are used to define tolerances for the quality of the magnets at the design stage and during production. Despite all precautions the beam lifetime will not be infinite, in other words a fraction of the particles will diffuse towards the beam pipe wall and be lost. In this event the particle

energy is converted into heat in the surrounding material and it can induce a quench of the superconducting magnets. To avoid this, a collimation system will catch the unstable particles before they can reach the beam pipe wall, so as to confine losses in well shielded regions far from any superconducting elements. The LHC combines for the first time a large beam current at very high energy with a sophisticated superconducting technology. As a consequence it needs a much more efficient collimation system than the previous machines.

The technical choices made in the LHC to deliver high performance while minimising cost could drastically reduce the adaptability of the machine, since most of its elements are closely packed and embedded in a continuous cryostat.

In electron-positron colliders the particles lose energy through synchrotron radiation. This loss must be continuously compensated by the RF system, and as a consequence this phenomenon limits the attainable energy while providing damping of particles oscillations. These effects are smaller in the LHC owing to the larger mass of the proton the energy radiated during the same time is a tiny fraction of the beam energy. They will become significant in proton machines around 100 TeV. However, in the LHC the power emitted, about 3.7 kW, cannot be neglected as it has to be absorbed by the beam pipe walls as a large number of hard UV photons. These release absorbed gas molecules, which then increase the residual gas pressure, and liberate photoelectrons, which are accelerated across the beam pipe by the strong positive electric field of the proton bunches. These photoelectrons add to cryogenic load and may induce an instability of transverse coupled bunch modes [2]. When they hit the opposite wall, they generate secondary electrons which can in turn be accelerated by the next bunch if they are slow enough to survive. Depending on surface reflectivity, photo-emission and secondary emission yields, this mechanism can lead to the fast build-up of an electron cloud with potential implications for beam stability [4].

The LHC will provide huge detectors to study beams collisions. Four experiments will take place around the machine: ALICE, ATLAS, CMS and LHCb. The quarks and gluons, which in today's cold Universe are locked up inside protons and neutrons, would have been too hot to stick together at the Big Bang time. Matter in this state is called Quark Gluon Plasma (QGP). Physicists believe that the head-on collisions of lead ions at

the LHC energies will be ideal for making QGP, allowing ALICE to study its properties in detail. ATLAS and CMS goals are the same: detection of Higgs boson and search of "supersymmetric" particles. For these purposes, each experiment will develop "multi-purpose" detectors. Their experimental techniques are quite complementary. The LHCb collaboration is interested by the CP violation and the understanding of the difference between matter and anti-matter. For that purpose it will study the b-quarks creations and desintegrations.

The basic layout of the machine mirrors that of LEP, with eight straight sections each approximately 528 meters long, available for experimental insertions or utilities. The two high-luminosity insertions are located at diametrically opposite straight sections, point 1 (ATLAS) and point 5 (CMS) (see figure 1.1). Two more experimental insertions are

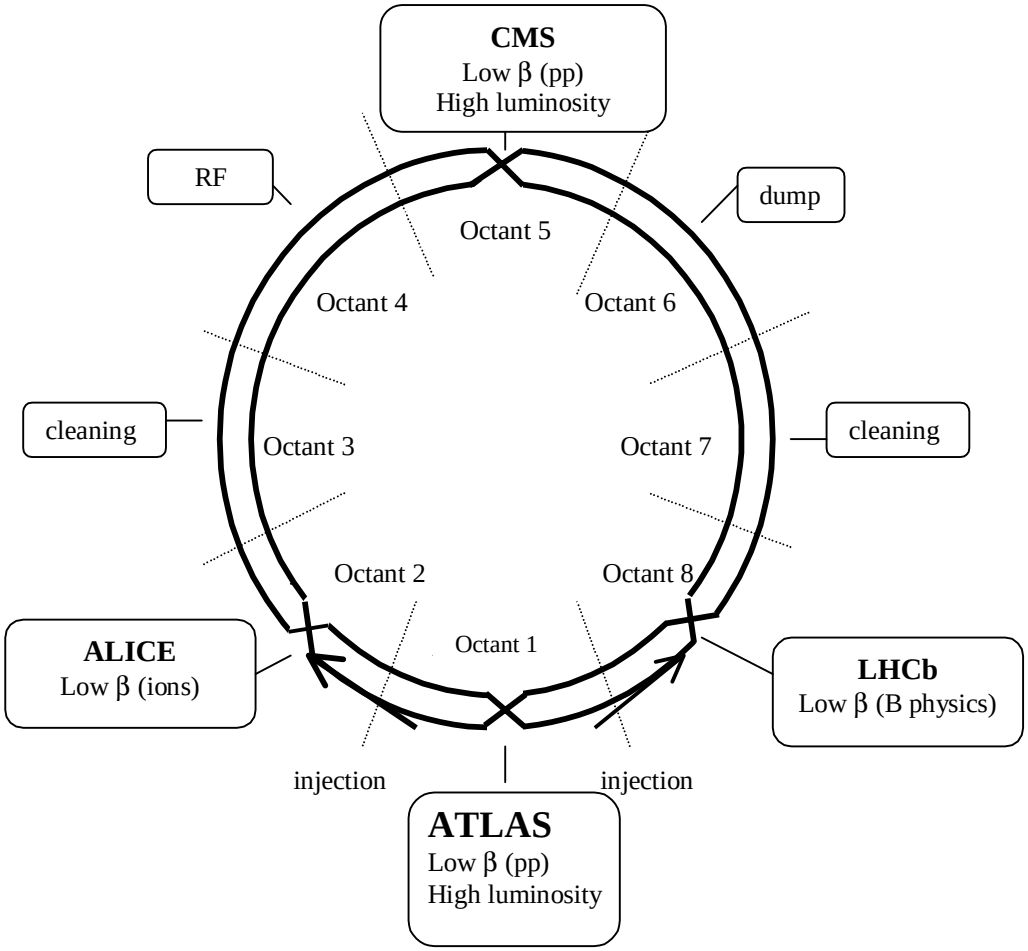

Figure 1.1 *Basic layout of the LHC machine* [6]

located at point 2 (ALICE) and point 8 (LHCb). These latter straight sections also contain the injection systems. The beams cross from one ring to the other only at these four locations. The remaining four straight sections do not have beam crossings [6]. Another collaboration will work on the LHC: TOTEM. It will be introduced in the CMS experimental hall. Its goal is to determine the total cross-section, the elastic scattering and the diffraction dissociation at the LHC [5].

1.1.2 CMS, experiment in which the luminosity monitor will be installed

The concept of a compact detector for the LHC based on a solenoid, the Compact Muon Solenoid (CMS) detector was presented in October 1990, its technical proposal in 1994. For a high luminosity proton-proton machine one thinks first to optimise the muon detection system. All types of magnetic configurations were studied. The requirement for a compact design led to the choice of a strong magnetic field. The design goals of CMS were defined as follows: a very good and redundant muon system, the best possible electromagnetic calorimeter (ECAL) consistent with such a muon system and a high quality central tracking [7].

CMS is a large technologically advanced detector made up of many layers. Each of these is designed to perform a specific task and all together they will allow CMS to identify and precisely measure the energies and momenta of all the particles produced in the LHC proton-proton collisions. The layers of the CMS detector are arranged like a cylindrical onion around the collision point. Central to the design of CMS is the biggest superconducting solenoid magnet with the highest field and stored energy ever made. The solenoid will be 13 metres long and with an inner diameter of 6 metres. It will generate a field of 4 Tesla (T), which means that the energy stored will be 2.5 Giga Joules, enough to melt 18 tons of gold.

A particle emerging from the collision and travelling outwards will first encounter the tracking system, a collection of three different detectors: Silicon pixels and Silicon strips. These will measure precisely the positions of passing charged particles allowing physicists to reconstruct their tracks. Charged particles will follow spiralling paths in the CMS magnetic field and the curvature of their path will reveal their momenta. The

energy of the particles will be measured in the next layer of the detector, the so-called calorimeters. The first calorimeter layer is designed to measure the energy of electrons and photons with great precision. Since these particles interact electromagnetically, it is called an electromagnetic calorimeter (ECAL). Particles which interact by the strong interaction, hadrons, deposit most of their energy in the next layer, the hadronic calorimeter (HCAL). The only particles that penetrate beyond the HCAL are the muons and the neutrinos. Muons are charged particles which will be tracked further in dedicated muon chamber detectors. Their momenta will also be measured from the bending of their paths in the CMS magnetic field. Neutrinos, however, are neutral and since their interaction in matter is very weak they will escape direct detection. Their presence can nevertheless be inferred. By adding up the momenta of all the detected particles the CMS physicists will be able to tell where the neutrinos were, if they have taken some energy and their momenta and direction.

All in all, CMS will have 15 10^6 individual detectors channels, all of which will be controlled by computers. These will synchronise the detector with the LHC accelerator making sure that CMS is ready to record any interesting collisions. In the LHC, bunches of protons will pass through each other 40 millions times a second, and with each bunch crossing 20 proton-proton collisions will occur on average making 800 million collisions per second. Not all of these will produce interesting results. Most of the time protons will just graze past each other. Head-on collisions will be quite rare, and the processes which produce new particles scarcer still. The Higgs boson, for example, is expected to appear in just one of every 10^{13} collisions. That means that even with 8 10^8 collisions a second, a Higgs boson would only appear about once every day [8]. Notice that the Higgs production cross-section is mass dependant.

The luminosity detector that we will study is planned to be installed in the CMS cavern with the TOTEM experiment. It will be at about 19 metres from the interaction point (IP) surrounding the vacuum tube in the pseudo-rapidity range of around 5 to 7. At that location the expected absorbed dose will be around 10^6 Gray (Gy) for an integrated luminosity of 5 10^5 pb^{-1} [9].

1.1.3 TOTEM, experiment which will permit the calibration of the luminosity monitor

The TOTEM collaboration proposes to measure the total cross section, elastic scattering and diffraction dissociation at LHC. Its aim is to obtain accurate information on the basic properties of proton-proton collisions at the maximum accelerator energy. For these measurements, particles emitted in the very forward region have to be detected. The measurement of interest for us is the total cross section one because it will provide an accurate absolute calibration for our luminosity monitor. This calibration will take place when TOTEM is running, i.e. under low luminosity conditions. The way proposed to measure the total cross section is by means of the so-called "luminosity independent method". In fact if no accurate and reliable measurements of the machine luminosity is available, this will be the only method of practical use. With the relation between the total cross section and the integrated luminosity of the machine and with the optical theorem relating the total cross section to the imaginary part of the forward amplitude, one may deduce the total cross section. This method based on the simultaneous measure of elastic scattering at low momentum transfer, t, and of the number of inelastic interactions will be presented more precisely in the section 1.3.3 on the luminosity monitoring [10].

The TOTEM experiment does not require high luminosities. It is therefore suited for running at the beginning of LHC operation. The first objective is to measure the total cross section at the earliest stage of the machine operation [11]. A sketch of the experimental apparatus is shown in figure 1.2**.** ***Elastic scattering detectors*** of small size and high spatial resolution are placed symmetrically on both sides of the crossing region inside "roman pots" which will approach the beam from above and below. Three Roman pot stations with a dipole magnet in between will be used to detect the proton which is scattered quasi-elastically in diffraction dissociation and measure its momentum. The three Roman pot stations will be placed inside the LHC tunnel at, respectively, about 94 m, 154 m and 180 m from the Interaction Point (IP). *A* ***forward inelastic detector*** will be used for the measurement of the inelastic rate including events of single diffractive type. Split into 2 units, telescopes T1 and T2 (see figure 1.3), it will cover, on both sides of the crossing, an interval of nearly four pseudo-rapidity units (between 3 and 7) in the

forward direction with full azimuthal acceptance. T1 will be placed inside the end cap region of CMS at a distance between 7.5 m and 10.5 m from the IP while T2 will be placed inside the rotating shielding of CMS at a distance between 15 m and 18 m from the IP. The forward inelastic detector is needed for the measurement of the total cross section and diffraction dissociation.

The "luminosity independent method" allows to measure the total cross section and to calibrate simultaneously the TOTEM inelastic detector in an absolute way. The apparatus will detect particles in the forward or very forward cone, an angular region not covered by the large CMS sub-detectors. At high energy, elastic scattering is confined too such small angles that the measurement is possible only in a special insertion with high β-optics. The whole equipment is of small size in the direction transverse to the beam. It will be placed far away from the CMS crossing point as specified here above and will easily fit inside the existing tunnel without any need for civil engineering. During the normal LHC runs TOTEM will run in parasite mode for setting up. While it is desirable to have independent runs at the beginning, it is equally important to be able to run both experiments together. Speaking about the TOTEM operation, one has to notice that the measurement of the total cross section and diffractive processes at low-t can be performed only with special optics at high-β (β*=1000-1500 m) (see § 2.1) which allows detection of particles emitted at very small angles. High-β optics leading to large beam size imply relatively low luminosity. TOTEM proposes to run with a luminosity around 10^{28} cm^{-2} s^{-1} and a reduced number of bunches compatible with the LHC injection scheme. The large bunch spacing permits zero crossing angle and there is no time overlap between incoming and outgoing bunches as seen by the Roman pots. The large bunch separation also simplifies the detectors and the associated electronics. To summarise the special operation conditions for TOTEM are the high-β, the large bunch spacing and the zero crossing angle [10,11] .

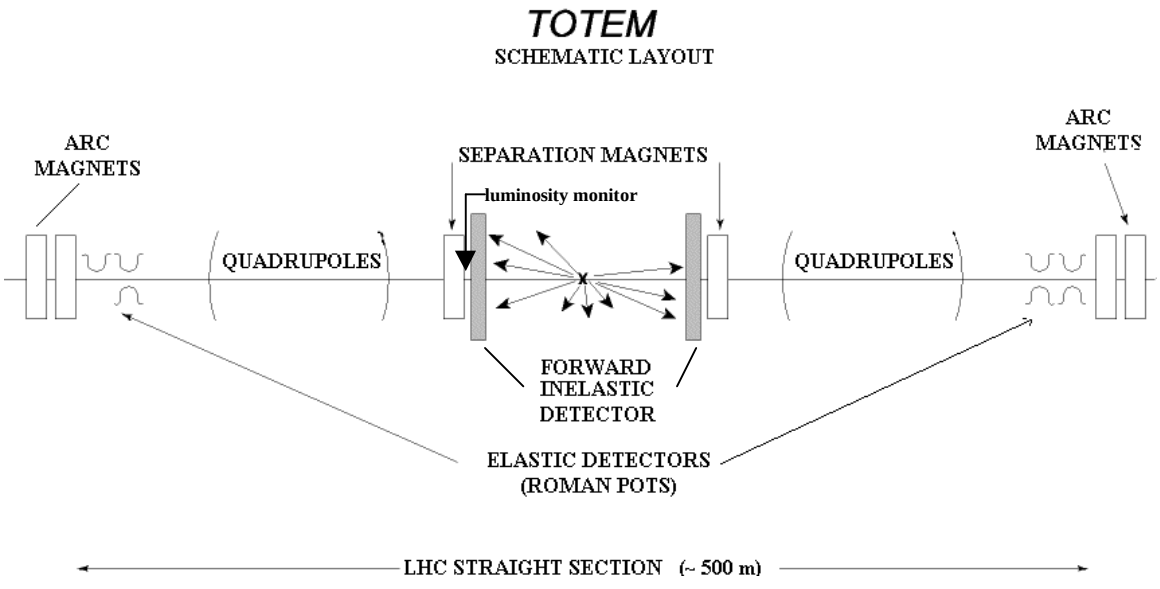

Figure 1.2 *Sketch of the experimental apparatus of TOTEM* [10]

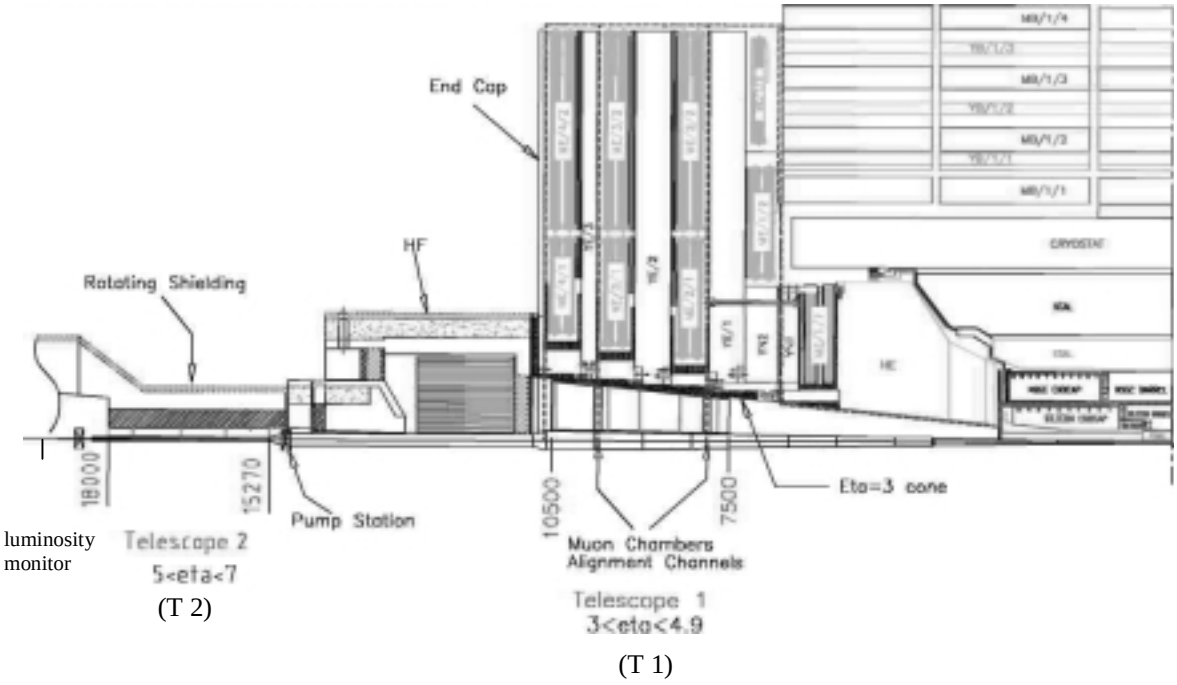

Figure 1.3 *Section of the CMS experimental apparatus showing the integration of TOTEM telescopes T1 and T2* [11]

1.2 Definition of luminosity

The most important parameter of the LHC, apart from the energy of the colliding beams, will be its luminosity, a quantity of most immediate interest for the high energy physicists. The luminosity, L, relates the reaction rate R of a process to its cross section, σ, and is defined by

$$R = L\sigma \tag{1.1}$$

with L normally expressed in units of cm^{-2} s^{-1}. The highest instantaneous L achieved to date (1998) is about 4.5 10^{32} cm^{-2} s^{-1} at CESR, and for protons, 2.3 10^{32} $cm^{-2}s^{-1}$ at the now-decommissioned ISR [12]. The critical quantity for the high energy physicists is the integrated L, often stated in pb^{-1} (pb stands for picobarn, 1 barn = 10^{-28} m^2). For example, during the most-recent two-years Tevatron run, an integrated luminosity of 150 pb^{-1} was obtained [12]. For experiments in which a beam hits a stationary target ("fixed target experiments") the luminosity has usually a simple form. Assuming that the transverse size of the beam is much smaller than that of the target, it follows from the definition of the cross section and equation 1.1 that

$$L = \rho d \frac{\Delta N}{\Delta t} \tag{1.2}$$

where ρ is the number of target particles per unit volume (ρ is assumed to be constant throughout the target), d is the effective length of the beam path within the target, ΔN is the number of beam particles hitting the target and Δt is the considered time interval. In such a case the luminosity measurement just requires the measurements of ρ, d and $\Delta N/\Delta t$ [13].

In a colliding beam machine the expression for L is more complicated because the target is moving and we can not always assume that the target is wider than the beam [14]. Consider first a single ring collider with N particles per beam and r.m.s radii of σ_x (horizontal) and σ_z (vertical). The cross sectional area of the beam is then $\pi\sigma_x\sigma_z$ and the

number of particle of one beam that one particle of the other beam encounters during one turn of the machine, assuming the beams follow identical paths, is

$$\frac{\sigma}{4\pi\sigma_x\sigma_z}N \tag{1.3}$$

where σ is the effective cross section of the particle. The total rate of interactions, R_T, assuming f the frequency at which particles circulate in the ring is

$$R_T = \frac{N^2 f\sigma}{4\pi\sigma_x\sigma_z} \tag{1.4}$$

Notice that nothing has been said about the azimuthal distribution of the particles around the machine and for continuous or DC beams these interactions would be spread around the whole machine circumference. If there are k bunches in each beam the interaction rate per crossing, R, is given by

$$R = \frac{N^2 f\sigma k}{4\pi\sigma_x\sigma_z} \tag{1.5}$$

It follows from the luminosity definition (see equation 1.1)

$$L = \frac{N^2 fk}{4\pi\sigma_x\sigma_z} \tag{1.6 a}$$

or since it is more usual to measure beam currents I with I=Nef

$$L = \frac{kI^2}{4\pi e^2 f\sigma_x\sigma_z} \tag{1.6 b}$$

σ_x and σ_z, the r.m.s dimensions of the two beams at the crossing points, are assumed here to be constant over the effective crossing region which is a function of the bunch length. If one beam has a much larger cross section than the other then the $\sigma_x\sigma_z$ term must be replaced by an effective area A_{eff} which will be approximately the area of the larger beam. A general expression for the luminosity [15] for the collision between bunched beams is presented in appendix A. For LHC the luminosity is given by [6]

$$L = \frac{N^2 k_b f \gamma}{4\pi\varepsilon_n \beta^*} F \qquad (1.7)$$

where N is the number of proton per bunch, k_b the number of bunch, f the revolution frequency, γ the relativistic factor, ε_n the normalised transverse emittance, β^* the value of the betatron function at the IP and F (~0.9) the reduction factor caused by the crossing angle. The transverse emittance is a beam quality concept reflecting the process of bunch preparation, extending all the way back to the source for hadrons; the betatron function is a beam optics quantity and is determined by the accelerator magnet configuration. To achieve high luminosity, one wants β^* to be as small as possible; how small depends on the beam beam effects and the capability of the hardware to make a near-focus at the IP [12]. The demonstration of equation 1.7 is given in appendix A.

1.3 Luminosity monitoring

1.3.1 Direct evaluation of the luminosity

In practice two methods are used to measure the luminosity at colliders. If the geometry and particle populations of the colliding beams are known the luminosity can be calculated from equations 1.6; if the rate R of a process can be measured and its cross section is well known, the luminosity can be calculated from equation 1.1. The first method gives usually a not very precise luminosity measurement because an accurate

measurement of the beam currents and especially of the beam size at the IP is difficult. Using the second method, the uncertainty of the experimental corrections of the measured rate R is often the source of limitations for the luminosity determination. In practice, one method often supplements the other [13]. Scintillators or Si detectors are often used to measure the rate R, the faster ones are the most accurate. Transformers are often used to determine the luminosity through beam current measurement; their actual lower limit is in the range of 10^{-11} A. For the high intensities the wire-scanners often give the beam dimensions. Their resolution corresponds to their diameter; today it is in the range of 100 μm. At the LHC the beam size at the interaction points will be 15.9 μm rms in the x and the y directions which corresponds roughly to 300 μm rms in the arc sections at the positions of the wire scanners [16]. The second method is usually used at e^+e^- colliders and the luminosity measurement is based on e^+e^- Bhabha scattering. For example, in the ALEPH experiment at the LEP collider the luminosity is measured with a precision better than 1%, of which 0.3% is due to the theoretical uncertainty in calculation of the Bhabha cross section and 0.6% is due to experimental systematic errors [17]. For hadron $p\bar{p}$ high energy colliders the process of elastic electromagnetic $p(\bar{p})p \rightarrow p(\bar{p})p$ scattering is difficult to measure and therefore the first method is commonly used. Beam dimensions are usually measured a few meters from the interaction region and the specific luminosity is derived from the results of a beam transport program. Then by the measurement of the beam currents the luminosity can be determined (e.g. with the use of equations 1.6). This method is not very accurate (8% accuracy at Spp/S at CERN [18] and about 11% at Tevatron at Fermilab [19]) but in some cases the precision can be very much improved (e.g. Van der Meer method at the ISR).

1.3.2 The Van der Meer method

At the ISR collider a 0.3% error on the luminosity measurement was achieved [20] with the use of a method developed by S. Van der Meer [21]. The ISR machine was an unbunched (“coasting”) beam collider with non-zero crossing angle, and its luminosity was given by [14]

$$L = \frac{I_1 I_2}{ce^2 h_{eff} \tan(\alpha/2)} \qquad (1.8)$$

where I_1,I_2 are the total currents in the beams, e is the electron charge, h_{eff} is the effective height of the beam collision region and α is the crossing angle. Van der Meer's idea was to displace one of the two beams vertically with respect to the other one and plot the counting rate versus the displacement. He demonstrated that h_{eff} is equal, irrespective of the beam shape, to the area under the curve divided by the ordinate for zero displacement (see figure 1.4 and appendix B). With h_{eff} determined, the luminosity can be calculated using equation 1.8. The currents I_1 and I_2 can be very accurately measured using a DC transformer and the beam crossing angle is known to high precision. This method requires a very high accuracy ($\pm$ 20 μm) of the beam displacement measurement. For the LHC the beam will be bunched. Thus, contrary to the ISR situation, the crossing angle at the LHC has to be considered as a second parameter in the determination of the luminosity. When one beam is displaced in respect to the other one, it is not anymore sure that interactions occur. The counting rate is dependant on the crossing and on the relative

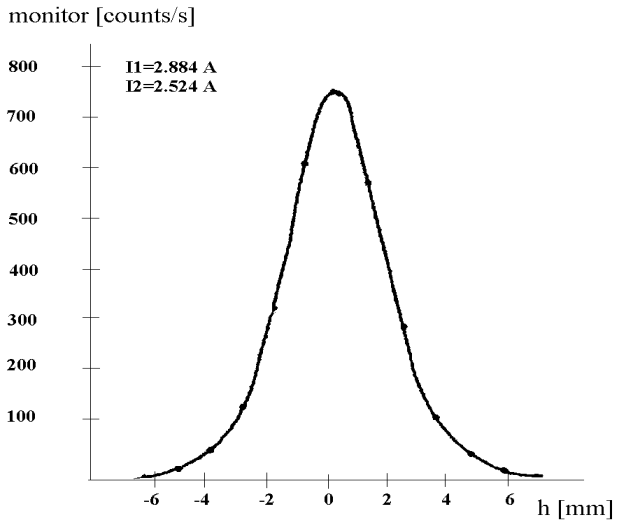

Figure 1.4 *The counting rate in a luminosity monitor as a function of the vertical separation h between the two ISR coasting beams* [14]

height of the two beams. Now two quantities, the two direction dimensions of the beams, have to be known. Thus the Van der Meer method if used for the LHC luminosity determination will require two scans, one according to the x axis and one according to the y axis. This is much complicated than for the ISR case and it will be less precise.

1.3.3 The "luminosity independent method"

The TOTEM collaboration proposes to determine the LHC luminosity thanks to the measurement of the total cross section by means of the so called "luminosity independent method" (see appendix C). This method was used in earlier experiments as by the CERN-Pisa-Roma-Stony Brook collaboration, by UA4 at the SPS collider or by E710 and CDF at the Fermilab. It is based on the simultaneous measurement of small-angle elastic scattering and of the total inelastic rate [10,22]. The total cross section, σ_{tot}, and the integrated luminosity, L, of the machine are related by the equation

$$N_{el} + N_{inel} = L\,\sigma_{tot} \tag{1.9}$$

where N_{el} and N_{inel} are the observed rates of elastic and inelastic interactions, respectively. The total cross section can be expressed in terms of the forward differential elastic rate through the optical theorem [23-25] which relates the total cross section to the imaginary part of the forward amplitude (see appendix C), as

$$\left(\frac{dN_{el}}{dt}\right)_{t=0} = L\left(\frac{d\sigma_{tot}}{dt}\right)_{t=0} = L\frac{\sigma_{tot}^2\left(1+\rho^2\right)}{16\pi} \tag{1.10}$$

where the parameter ρ is defined as the ratio of the real to the imaginary part of the forward amplitude, ρ = ReF(0)/ImF(0), and where t represents the momentum transfer. Combining equations 1.9 and 1.10 gives the total cross section as a function of measurable quantities

$$\sigma_{tot} = \frac{16\pi}{(1+\rho^2)} \frac{(dN_{el}/dt)_{t=0}}{N_{el}+N_{inel}} \quad (1.11)$$

The parameter ρ is small at high energy (~0.1-0.2), so that it does not have to be known with high precision to get an accurate value of σ_{tot}. The elastic scattering t-distribution, dN_{el}/dt, is measured at small t using the "Roman pot" system (see figure 1.2) and extrapolated to t=0, the so called "optical point". The total number of inelastic events N_{inel} will be measured by the forward inelastic detector (see figure 1.2).

1.3.4 Why a new luminosity monitor for the LHC?

The LHC will collide high energy protons creating a high radiation level[26]. The interaction of protons beams creates hadronic showers. The subsequent interaction of the secondaries with the surrounding material multiplies the number of particles (while degrading the individual energy). Nuclei in the materials can be excited and produce "evaporating neutrons" at the origin of the induced radioactivity in the surrounding structures of the interaction points. Monte-Carlo simulations give an estimation of the radioactivity thanks to the calculation of the number of inelastic interaction. The proposed luminosity monitor will be placed in the CMS experimental area at 19 meters from the interaction point. At that position the charged particles (hadrons and muons) fluxes corresponding to the LHC peak luminosity [27] (10^{34} $cm^{-2}s^{-1}$) will be around 10^6 $cm^{-2}s^{-1}$. It corresponds to an absorbed dose in the range of [10^4, 10^5] Gy (value corresponding to an integrated luminosity of 5 10^5 pb^{-1} [28]). Because of this high radiation level, the proposition of a radiation resistant luminosity monitor is obvious. The monitors used in the previous CERN accelerators (ISR, SPS, LEP) for such a measurement were almost all based on scintillators [29-32]. As they will not be resistant enough for the LHC case, the Secondary Emission Chambers (SEC), used for years at CERN and known to be radiation hard were proposed as luminosity monitors for CMS with a calibration given by the TOTEM experiment. An other request not fulfilled by the actual detectors is the coverage of six orders of magnitude. The LHC will indeed run at luminosities from

10^{28} $cm^{-2}s^{-1}$ to 10^{34} $cm^{-2}s^{-1}$ and then the new monitor must be able to work for this full range of luminosity.

Our proposal to measure luminosity in the CMS experiment is the following. First the calibration of the proposed monitor (for instance SEC) at low luminosity (~ 10^{28} $cm^{-2}s^{-1}$) using the "luminosity independent method". It will be achieved by the TOTEM experiment (see § 1.3.3). It will provide the proportionality coefficient between the LHC luminosity and the output current of our monitor. Then, at higher luminosity, as the monitor response is linear with the incident intensity (see chapters 6 and 7), the proportionality coefficient will allow us to determine the luminosity from the output current of our monitor.

Chapter 2 General characteristics of accelerators and detectors

2.1 A brief introduction to accelerators

As seen on chapter 1, the LHC luminosity is given by (see equation 1.7)

$$L = \frac{N^2 k_b f \gamma}{4\pi\varepsilon_n \beta^*} F \qquad (2.1)$$

where N is the number of proton per bunch, k_b the number of bunch, f the revolution frequency, γ the relativistic factor, ε_n the normalised transverse emittance, β^* the value of the betatron function at the interaction point and F (~0.9) the reduction factor due to the beams crossing angle. To understand the formula, in particular the meaning of emittance and betatron function, some concepts of the accelerator physics are given [33].
Both electric and magnetic fields play an important role in modern accelerators. Electric fields provide the accelerating force acting on the particles longitudinal motion. Magnetic fields guide and focus the particles acting on their transverse motion. Their combined effect may be written

$$\frac{d\vec{p}}{dt} = e(\vec{E} + \vec{v} \times \vec{B}) \qquad (2.2)$$

with $\vec{p}$, the relativistic momentum of the particle [eV/c],

$\vec{E}$, the electric field [V/m],

$\vec{B}$, the magnetic field [Tesla],

$\vec{v}$, the velocity of the particle [m/s].

For the **longitudinal motion**, tangential to beam direction, the Radio Frequency (RF) cavity is the device of first importance. Its sine wave voltage acts on the charged particles as an accelerating or decelerating electric field, depending of their phase in respect with

the so-called “synchronous particle”. This one arrives at the cavity entrance with a fixed RF phase value, ϕ_s. Its motion equation satisfies to $\phi(t) = \phi_s$ = constant. It is not obvious that the sine wave of accelerating voltage in the cavity could be kept in synchronism with the arrival of the particle each time it made a turn of the machine. Any slight mistiming of the wave might build up over many turns until particles would begin to arrive within the negative, decelerating phase of the sine wave and be left behind. Even if synchronism for the “ideal”, synchronous, particle is achieved with success, there would be other particles of slightly different momentum whose path would be different and therefore would take a different time to circulate around the machine. The fundamental principle of phase stability deals with this and ensures the stability of the particles motion avoiding them to be lost turn after turn. Before understanding this principle few technical terms, as voltage per turn, harmonic number or bunch, are introduced [33]. The **voltage per turn** is the total potential difference experienced by the particle due to the radio frequency field across all the accelerating structures in the ring. This will be just the integrated voltage as it passes through the cavity. In general, a particle circulates around a machine of circumference $C=2\pi R$ in a time τ and with a frequency f where

$$f = \frac{1}{\tau} \text{ [Hz]} \qquad (2.3)$$

The synchronous particle arrives at the same phase ϕ_s of the RF wave. For this to occur f_{RF} must be a multiple of f

$$f_{RF} = h\, f \text{ [Hz]} \qquad (2.4)$$

where h, the **harmonic number,** is an integer which defines the number of location, regularly spaced around the machine, with the stable phase ϕ_s. Particles can gather together around these positions. For big modern synchrotrons h may be very large: in the SPS, for example, h=4620 thus there are 4620 locations on the circumference where a particle can arrive synchronously. The beam could be therefore split up into as many as 4620 **bunches**, centred on these synchronous points. The particle motion in the longitudinal phase space is represented in diagrams by two parameters: ΔE and ϕ . ΔE is

the energy difference between the particle and the synchronous particle. ϕ is the relative phase between the particle phase and the RF wave phase (see figure 2.1). The phase of a particle can always be redefined with respect to the nearest rising zero-crossing to keep ϕ within the range $[-\pi, \pi]$. Particles follow either closed or, if unstable, open paths in these plane diagrams. Notice that a phase advance, ϕ, can be related to a distance on the accelerator circumference, the distance between the particle and the coordinate system origin (where $\phi=0$). Figure 2.1 describes the situation below a certain critical energy called 'transition' at which the particle velocity and trajectory variation compensate each other. The phase stability principle could be explained as follow. A late particle, B, in respect with the synchronous one, A, sees its energy increasing. Thus it overtakes the synchronous particle and its energy becomes larger than that of the synchronous particle. On the next turn the same particle arrives in advance with respect to the synchronous one and undergoes an energy gain lower than that of the synchronous particle. It will be slowed down until overtaken by the synchronous particle. Thus the particle will oscillate around the synchronous particle. Provided its amplitude is not too large, the particle follows an ellipse in the phase space describing this motion up and down the linear part of the RF wave. For particles onto the non-linear part of the RF wave and over the top,

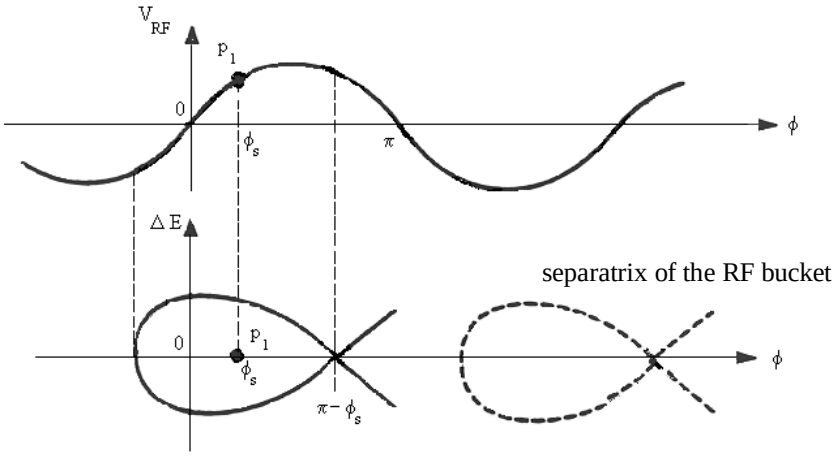

Figure 2.1 *Energy variation versus phase or principle of phase stability below transition*

the motion is no longer the simple harmonic motion ellipse but becomes a fish-shaped trajectory remaining closed for stable motion. A particle on the stability limit, starting at $\phi=\pi-\phi_s$, would trace out a limiting fish-shaped trajectory, the separatrix between stable and unstable motion. This shape is called the RF bucket.

For the **motion** [33] **transverse** to beam direction (see figure 2.2), the effects of magnetic fields produced by magnets arranged around the machine circumference are considered. The bending fields are usually verticaly directed, causing the particle to follow a curved path in the horizontal plane. The force acting on the particle is horizontal and is given by equation 2.2 with $\overline{E}=0$, $\vec{v}$, the velocity of the charged particle in the direction tangential to its path, and $\vec{B}$, the magnetic guide field. If the guide field is uniform, the ideal motion of the particle is simply a circle with radius of curvature ρ. To describe the motion in a non-uniform field a local radius of curvature ρ(s) is used. The equilibrium or closed orbit is defined as the curved path of the particle which closes on itself around the accelerator. A particle may be displaced horizontally or vertically from that ideal position. The transverse displacements are x and z, respectively. A particle may also have divergence angles horizontally and vertically, x'=dx/ds and z'=dz/ds. This would cause it to leave the vacuum pipe. Fortunately a carefully shaped field restores it back towards the

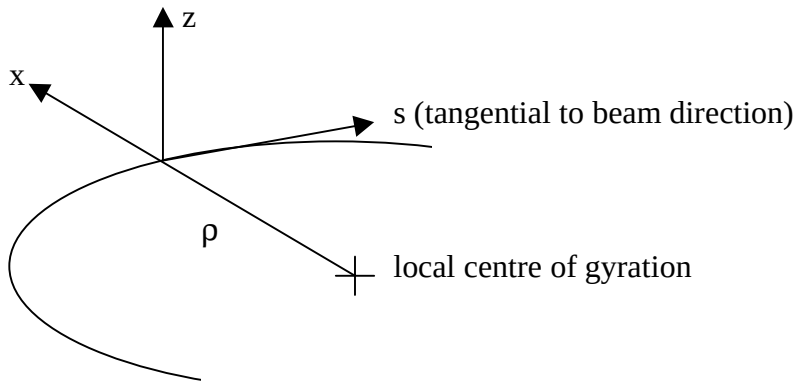

Figure 2.2 *Charged particle orbit in magnetic field*

beam centre so that it oscillates about the ideal orbit. The design of the restoring fields determines the beam transverse excursions as well as the cross section size of the magnets.

Quadrupole magnets provide the restoring fields. They are usually embedded in the sequence of bending magnets in an alternating pattern. The lattice is defined as the arrangement of magnets in a circular accelerator. For a given plane, horizontally or vertically, half focuses the beam while the other half defocuses it but the overall effect is focusing. The envelope of these oscillations follows the betatron function $\beta(s)$. Particles do not follow the $\beta(s)$ curve but oscillate within it in a form of modified sinusoidal motion whose phase advance is ϕ. Thus the betatron function describes the peak excursion of a beam. β is a property of the focusing system not of the beam. It varies around the ring. Hereafter the concept of focusing is introduced in a tangible way. For that purpose vertical motion is ignored. Consider an infinitely long quadrupole so that a particle oscillates within it exactly like a small sphere rolling down a slightly inclined gutter with constant speed. Its motion follows a periodic wave. Imagine the gutter bent into a circle rather like the brim of a hat. Suppose the displacement of the sphere from the centre of the gutter is measured each time it passes a given mark. Its transverse velocity which might be converted into its divergence angle $x' = dx/ds = v_{\perp}/v_{//}$ is measured. In figure 2.3, the phase space diagram represents x' versus x (each point corresponding to each arrival of the sphere). The sphere may have a large transverse velocity as it crosses the axis of the gutter or it might have almost zero transverse velocity as it reaches its maximum displacement. The locus will be an ellipse and the phase will advance by Q revolutions each time the sphere returns. Coming back to circular accelerators, Q, the tune of the machine, is the number of betatron oscillations performed by particles around the circumference.

In the same way a particle beam may be represented in a phase space diagram as a cloud of points within a closed contour usually an ellipse. The area of the ellipse, A, a measure of how much the particles depart from the ideal trajectory represented by the origin, is

$$A=\pi\varepsilon = \pi \int x' dx \text{ [mm x mrad]} \qquad (2.5)$$

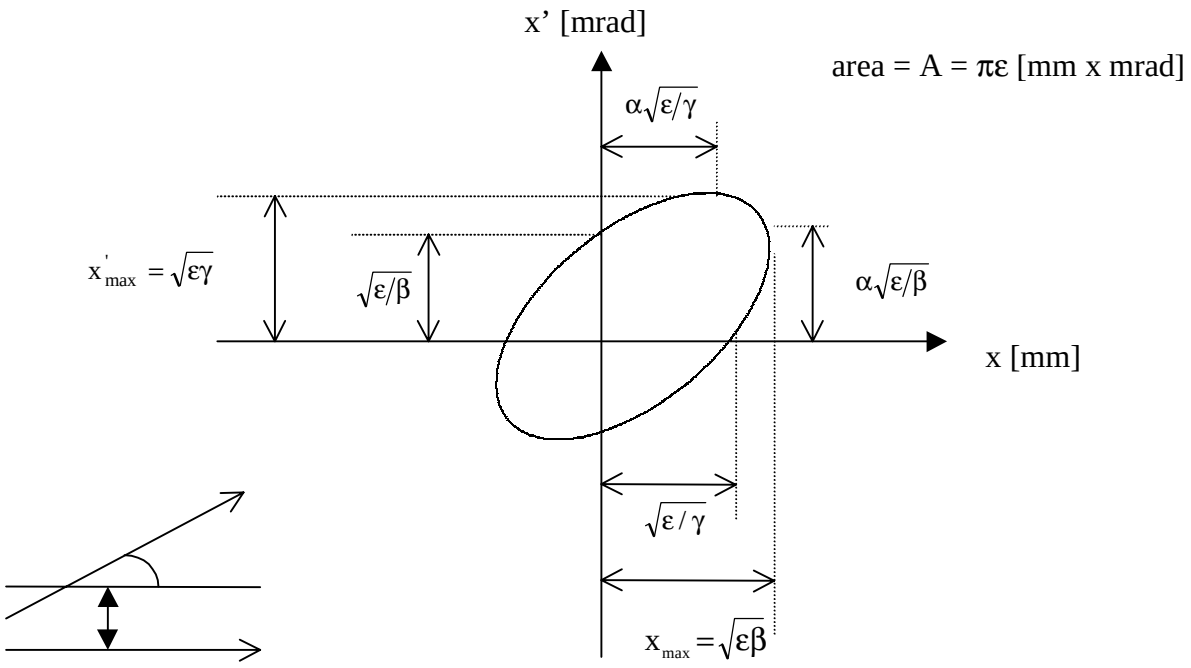

With x, the transverse particle coordinate in the x direction,

x', the particle divergence angle,

ε, the beam emittance,

α, γ, twiss parameters,

β, the betatron function.

Figure 2.3 *The elliptical locus of a particle's history in phase space as it circulates in a ring*

with ε the beam emittance. The so-called "Twiss parameters", α and γ, (see figure 2.3) are introduced to determine the shape and orientation of the ellipse at azimuthal location along the lattice. As long as the beam energy remains constant, in absence of radiation and of some collective effects, the value of ε remains constant. This is a consequence of Liouville's theorem which states that: " In the vicinity of a particle, the particle density in the phase space is constant if the particles move in an external magnetic field or in a general field in which the forces do not depend upon velocity." This definition rules out the application of Liouville's theorem to situations in which space charge forces play a

role or when particles emit synchrotron light. As already mentioned, particles circulating in a ring perform betatron oscillations around the closed orbit [33]. Therefore, when observed always at the same location around the ring, a dot representing a particle in the (x, x') diagram will move on an ellipse concentric with and similar to the emittance ellipse. As the particle trajectory evolves along the ring, the ellipse continuously changes its form and orientation but not its area. If Q=m/n is rational the particle will appear cyclically at only n points on the ellipse. If Q is irrational the particle trajectory will cover the ellipse densely.

All of this is true for a beam circulating at constant energy. During acceleration, the electric field of the RF cavities increases the particle's momentum in the s-direction, whereas the transverse (horizontal or vertical) momentum remains unchanged. In the (x, x') diagram, regarding the ellipses as the trajectories of the extreme particle before and after acceleration, the emittance shrinks as 1/p (p being the momentum in the direction of motion). Multiplication of the emittance by $\beta\gamma$ gives the normalised emittance, ε_n. Note that $\beta\gamma$ is proportional to the beam momentum and ε_n remains constant throughout acceleration [34, 35]:

$$\varepsilon_n = \varepsilon\beta\gamma = \text{constant} \qquad (2.6)$$

with $\beta=v/c$ the relative velocity

$\gamma=E/mc^2$ the relativistic factor

A more rigorous explanation for the normalised emittance introduces the fact that Liouville's theorem is related to hamiltonian mechanics. To ensure that this theorem applies during acceleration the emittance must be expressed in the canonical phase space (q, p) and related to the displacement, x and divergence, x' because the coordinates (x,x') are not "canonical" in the hamiltonian sense. An exhaustive explanation is out of our scope.

2.2 General characteristics of detectors [36, 37]

As already mentioned, the luminosity monitor will be at 19 meters from the CMS interaction point. At that location, the simulations reveal the presence of hadrons, muons, electrons and photons. So before explaining the general characteristics of detectors, the phenomena that could occur along the path of such particles through matter are introduced.

2.2.1 Passage of particles through matter[36, 37]

The knowledge of the interactions occurring when particles encounter matter is of first importance for the experimental physicist being the basis of the particle detection devices. They could however disturb the detection by, for example, causing energy information to be lost, deflecting the particle from its original path or absorbing the particle before it can be observed. Thus it is absolutely necessary to know them and their magnitude. The interactions depend, on one hand, on the energy and particle type and on the other hand, on the matter type. For charged particles and photons, the most common processes are the electromagnetic interactions with at high energy the possibility of secondary particles creation. For neutrals (except photons, Z^0 and neutrinos), processes involving the strong interaction preferentially occur. One needs to know for the detectors conception some properties of the particles, as their energy loss in the material window, their diffusion and their path if the window is thick. In general, the loss of energy and the deflection from the original direction are the two mean features to characterise the passage of charged particles though matter. These result from the inelastic collisions with the atomic electrons of the material and from the elastic scattering from nuclei. Other processes include emission of Cherenkov radiation, nuclear reactions and bremsstrahlung. In comparison to the atomic collision processes, they are extremely rare and will be ignored here. The charged particles are separated into two classes: electrons and positrons, on one hand, and particles heavier than electrons like muons, pions, kaons, protons, α-particles and other light nuclei, on the other hand.

Consider first **heavy charged particles**. Two processes are at the origin of their energy loss and their deflection when crossing the screen. Interactions with the atomic electrons are responsible for the energy loss while elastic collisions with the atomic nuclei change the particles path. The inelastic interactions with the atomic electrons can be divided into two groups. The soft collisions in which only an excitation results, and the hard collisions in which the energy transferred is sufficient to cause ionisation. In some of the hard reactions, enough energy is transferred so that the ejected electron itself causes substantial secondary ionisation. These high energy recoil electrons are sometimes referred to as δ-rays or knock-on electrons. Crossing a material with atomic number, Z, atomic mass, A, and density, ρ, a charge particle, z, with a velocity β=v/c will lose an energy per unit path of

$$-\frac{dE}{dx} = 2\pi N_A r_e^2 m_e c^2 \rho \frac{Z}{A}\frac{z^2}{\beta^2}\left[\ln\left(\frac{2m_e\gamma^2 v^2 W_{max}}{I^2}\right) - 2\beta^2\right] \qquad (2.7)$$

with dE/dx in [$MeVg^{-1}cm^2$]

$2\pi N_A r_e^2 m_e c^2 = 0.1535$ $MeVcm^2/g$

r_e: classical electron radius = 2.817×10^{-15} m

m_e: electron mass=0.510 MeV/c^2

N_A: Avogadro's number = 6.022×10^{23} mol^{-1}

I: mean excitation potential [eV]

Z: atomic number of absorbing material

A: atomic weight of absorbing material [$gmol^{-1}$]

ρ: density of absorbing material [cm^{-3}]

z: charge of incident particle in units of e

β=v/c of the incident particle

$\gamma = 1/(1-\beta^2)^{-1/2}$

W_{max}: maximum energy transfer in a single collision.

This equation, the so-called "Bethe-Bloch formula", is the basic expression used for energy loss calculations. The maximum energy transfer, W_{max}, is that produced by a

head-on collision. The mean excitation potential of the atomic electrons, I, is the main parameter of the Bethe-Bloch formula. At non-relativistic energies, dE/dx is dominated by the overall $1/\beta^2$ factor and decreases with increasing velocity until about $v \cong 0.96$ c, where a minimum is reached. Particles at this point are known as minimum ionising. As the energy increases beyond this point, the term $1/\beta^2$ becomes almost constant and dE/dx rises again due to the logarithmic dependence of equation 2.7. This relativistic rise is cancelled, however, by the density correction. At low velocities comparable to the velocity of the orbital electrons of the material, dE/dx, reaches a maximum and then drops sharply again.

Consider now **electrons and positrons**. They also suffer an energy loss due to interaction when passing through matter. However, because of their small mass, the energy loss due to the emission of electromagnetic radiation arising from scattering in the electric field of a nucleus (bremsstrahlung) becomes important. Classically, this may be understood as radiation arising from the acceleration of the particle as it is deviated from its straight-line course by the electrical attraction of the nucleus. The bremsstrahlung increases with energy and at a few 10's of MeV, loss of energy by radiation is comparable to or greater than the collision-ionisation loss. At energies above this critical energy, bremsstrahlung dominates completely. The total energy loss of electrons and positrons, therefore, is composed of two parts:

$$\left(\frac{dE}{dx}\right)_{tot} = \left(\frac{dE}{dx}\right)_{rad} + \left(\frac{dE}{dx}\right)_{coll} \qquad (2.8)$$

The basic mechanism of collision loss outlined for heavy charged particles is also valid for electrons and positrons. The Bethe-Bloch formula must however be modified for two reasons. First, because of the small mass of electrons and positrons, the assumption that their path does not change during the interaction is not valid anymore. Secondly, for electrons, the interactions are between identical particles. The emission probability due to bremsstrahlung varies as the inverse square of the particle mass. The energy loss through radiation is proportional to Z^2 and the incident particle kinetic energy, while the one through collisions is proportional to Z.

In addition to inelastic collisions with the atomic electrons, charged particles passing through matter also suffer repeated elastic Coulomb scattering from nuclei. The vast majority of these collisions result in a small angular deflection of the particle. Assuming that the nuclei are much more massive than the incident particles, thus the small energy transfer to the nucleus is negligible. The cumulative effect of these small scattering angle is a net deflection from the original particle direction.

Looking at the **photons** behaviour in matter, note that they lack an electric charge so that they are not subject to Coulomb interactions with the electrons and nuclei in matter. Their main interactions are photoelectric effect, Compton scattering and pair production. Photoelectric effect involves the absorption of a photon by an atomic electron with the subsequent ejection of the electron from the atom. Since a free electron cannot absorb a photon and also conserve momentum, the photoelectric effect always occurs on bound electrons with the nucleus absorbing the recoil momentum. Compton scattering is the scattering of photons on free electrons. Pair production involves the transformation of a photon into an electron-positron pair. In order to conserve momentum, this can only occur in the presence of a third body, usually a nucleus. Moreover, to create the pair, the photon must have at least an energy of 1.022 MeV. The x-rays and γ-rays are many times more penetrating in matter than charged particles. A beam of photons is not degraded in energy as it passes through a thickness of matter, it is only attenuated in intensity. The first feature is due to the much smaller cross-section of the three processes relative to the inelastic electron collision cross-section. The second characteristic is due to the fact that the three processes above remove the photon from the beam entirely, either by absorption or scattering. The photons which pass straight through are those which have not suffered any interactions at all. They retain their original energy. The attenuation suffered by a photon beam is exponential with respect to the thickness of the material.

Like the photons, the **neutrons** lack of an electric charge makes impossible their coulombian interactions with atomic electrons or nuclei. Their principal means of interaction is through the strong force with nuclei components. Neutrons must come within ~10^{-13} cm of the target before anything can happen. Thus it is not surprising that neutrons are very penetrating. When they interact, they may undergo a variety of nuclear processes depending on their energy. Among these are elastic scattering from nuclei for neutrons in the MeV region, inelastic scattering for energy on the order of 1 MeV or

more, high energy hadron shower production for very high energy neutrons with E greater than 100 MeV.

2.2.2 General characteristics of detectors [36, 37]

After a short summary on the detection principles, the concepts of sensitivity, energy resolution, time of response, efficiency and dead time are briefly introduced.
The detection is based on the transfer of a part or all of the particles energy to the detector which converts it into some other form more accessible to our perception. For charged particles this transfer is done through the interaction between atomic electrons and electric field produced by moving particles. This induces excitation or ionisation of the atoms. Neutral particles, on the other hand, must first undergo some sort of reaction in the detector; for instance energetic gamma will convert into electron-positron pair which will interact further with matter. The form in which the converted energy appears depends on the device and its design. Most of the modern detectors have an electronic readout in contrast to the bubble or emulsion chambers. Their information is transformed into electrical impulses which could be readout by electronics and computer means.
The **sensitivity** is the capacity of producing a usable signal for a given type of particle and of energy. A detector is designed to be sensitive to certain types of particle in a given energy range. Going outside this region usually leads to a decrease in sensitivity. The sensitivity depends on the cross section for ionising reactions in the detector, the device mass, the inherent noise and the protective material surrounding the sensitive volume. The first two determine the probability that the incident particle will leave a part or all of its energy in the detector volume. The signal lower limit is determined by the noise of the detector and of the associated electronics. The noise appears as a fluctuating voltage or current at the detector output and is always present whether there is particle or not. Obviously, in order to be used, the signal should be larger than the average noise level. Some clever signal detection techniques such as phase locked loop or stochastic resonance do not require this condition, however these are not applicable directly in this study. Another limiting factor is the material covering the detector. Here some incident particles can undergo interactions leading to possible absorption. Thus, only particles

with sufficient energy to penetrate this layer can be detected. The thickness of this material sets a lower limit on the energy which can be absorbed.

Some detectors are dedicated to energy measurement. Their most important factor is the **energy resolution**. The resolution is generally given in terms of σ, the standard deviation of the energy distribution. However, experimentally, the full width at the half maximum of the gaussian registered peak (FWHM=2.35σ) is often easier to read. If we denote this width as σ_E, then the relative resolution at the energy E is σ_E/E, usually expressed in percent.

The **time of response** is the time for the detector to form the signal after the arrival of the particle. A good timing is synonymous of a quick formation of the signal into a sharp pulse with a rising flank as close to vertical as possible. The signal duration is also of first importance. During this period the detector becomes insensitive or there is a pile-up of the electronic signals which degrades the information. This contributes to the **dead time** of the detector and limits the count rate at which it can be operated.

The detector **absolute and intrinsic efficiencies** have to be distinguished. The absolute or total efficiency is the fraction of events emitted by the source which is actually registered by the detector

$$\varepsilon_{tot} = \frac{\text{events registered}}{\text{events emitted by source}}$$

This is a function of the detector geometry and response. It can be factorised into two parts: the intrinsic efficiency, ε_{int}, and the geometric acceptance, ε_{geom}.

$$\varepsilon_{tot} \cong \varepsilon_{int} . \varepsilon_{geom}$$

The intrinsic efficiency is that fraction of events hitting the detector which is registered. This probability depends on the interaction cross section of the incident particle on the detector medium. The geometrical efficiency is that fraction of the beam which is geometrically intercepted by the detector. This, of course, depends entirely on the

geometrical configuration of the detector and of the angular distribution of the incident radiation.

In some detectors there exists a minimum time delay between two events to permit them to be recorded. Depending on the case this limitation comes from the detector itself or from the associated electronics. This minimum interval called the dead time leads to a count rate loss. Depending on the type, a detector may or may not, remain sensitive to other events during this period. If it is insensitive, any further events arriving during this period are lost. If the detector retains its sensitivity, then these events may pile-up on the first resulting in a distortion of the signal and subsequent loss of information from both events. To calculate the effects of dead time the entire detection system must be taken into account. It is often the electronics which accounts for the larger part. Concerning dead time, two fundamental cases are usually distinguished: the extendable one and the non-extendable one. In the extendable case, the arrival of a second event during a dead time period extends this period by adding on its dead time starting from the moment of its arrival. This produces a prolonged period during which no event is accepted. The non-extendable case corresponds to an element which is insensitive during the dead time period. The arrival of a second event during this period simply goes unnoticed and after a certain time the element becomes active again. Often it is necessary to define to which class, extendable or non-extendable one, the detector belongs. As it is not an easy task, a solution consists to deliberately add, in a blocking circuit, elements with a dead time larger than all others elements into the system such that the detector system can be treated by one of the two fundamental models. This slows down the system but removes the uncertainty in the dead time model. This should be done quite early in the system in order to avoid pile-up problems later.

2.2.3 Detectors of interest in this thesis

During our study of a luminosity monitor for the LHC three kinds of detector will be encountered. Secondary Emission Chamber (SEC) and Ionisation Chamber (IC) will be tested as luminosity monitor candidate while a scintillator-photomultiplier association or scintillation counter (see figure 2.4) will be used as a reference counter during the probes of the first two. The SEC and the IC will be treated in the chapter 3.

The scintillation counter uses the fact that certain materials crossed by a charged particle emit a small flash of light, i.e. a scintillation. When coupled to a converter and amplifier device such as a photomultiplier, these scintillations can be converted into electrical pulses which can then be analysed and counted electronically to give information concerning the incident particle. The **scintillation counter** consists generally of a scintillating material optically coupled to a photomultiplier (PM) either directly or via a light guide (see figure 2.4). As a particle enters the scintillator, it excites the atoms and molecules. Light is emitted and then is transmitted to the PM where it is converted into a current of photoelectrons further amplified. Scintillators are based on the phenomenon of luminescence. When exposed to certain forms of energy they absorb and reemit the energy in the form of visible or UV light. A good scintillator should have a high efficiency for conversion of exciting energy to fluorescent radiation, transparency to the fluorescent radiation to allow transmission of the light, an emission in a spectral range consistent with the spectral response of existing photomutipliers and a short decay constant to avoid dead time. **Photomultipliers** convert light into a measurable electric current. A high voltage is applied to the cathode – dynode – anode structure so that a potential is set up along this structure. When an incident photon arrives on the photocathode, an electron is emitted via the photoelectric effect. Because of the applied voltage the electron is accelerated toward the first dynode. There, upon striking, it transfers some of its energy to the electrons in the dynode. Thus secondary electrons are emitted, which in turn, are accelerated toward the next dynode where more electrons are released and further accelerated. Thus an electron cascade is generated. At the anode this cascade is collected to give a current which can be analysed. The cathode and dynode systems are assumed to be linear and the current at the output of the PM will be proportional to the number of incident photons.

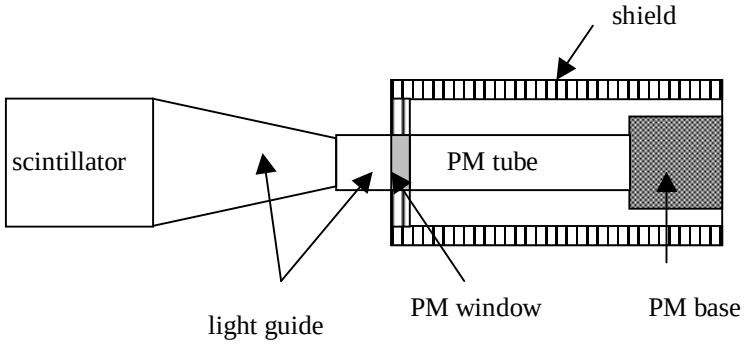

Figure 2.4 *Schematic diagram of a scintillation counter*

Chapter 3 Ionisation Chamber and Secondary Emission Chamber

Secondary Emission Chambers (SECs) have been used successfully at CERN since 1970. Our goal is to test if a detector based on the concept of SEC could be used as a luminosity monitor for the LHC. We have improved the previous technology and built a new generation of SEC prototypes. Our prototype has also been tested in Ionisation Chamber (IC) mode. The principles of IC and of SEC are introduced. Then the design and the modifications with respect to the previous technology of SEC are described.

3.1 Principle of ionisation chamber (IC) [36-40]

Ionisation chamber (IC) belongs to the family of ionisation detectors which are based on the direct collection of the ionisation electrons and ions produced by an ionising particle in gas. A basic configuration is a pair of metallic plates surrounded by gas (see figure 3.1). A voltage difference is applied between the plates and a radial electric field is thereby established. An incident particle between the plates creates along its path a number of ion-electron pairs proportional to its path length in the gas. The electric field accelerates the electrons and positive ions towards the anode and the cathode, respectively, where they are collected [36-39]. The output current signal depends on the electric field intensity. When no voltage is applied no charge is collected as the ion-electron pairs recombine under their own electrical attraction. As the voltage is increased, the recombination forces are overcome and the current begins to rise as more and more of the pairs are collected. At some point, all created pairs will be collected and further increases in voltage will show no effect. This is the IC mode in which we want to operate. Increasing the voltage beyond this region, the chamber enters the multiplication region. The electric field becomes strong enough to accelerate free electrons to an energy where they are also able to ionise the gas molecules. The electrons produced in these secondary ionisations are also accelerated to produce still more ionisation and so on. This results in an ionisation avalanche. The number of ion-electron pairs in the avalanche is

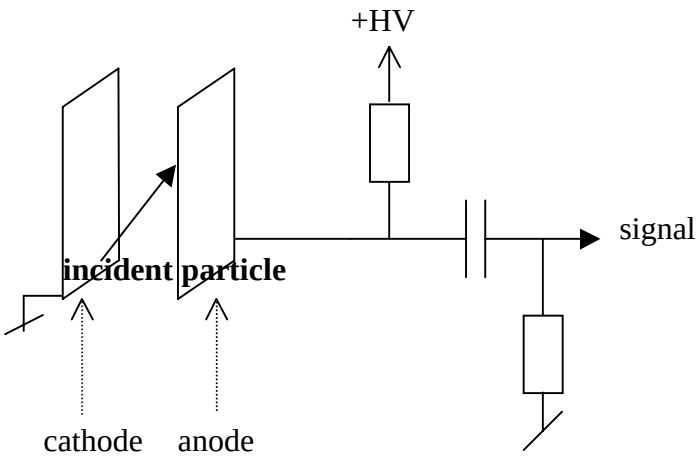

Figure 3.1 *Ionisation detector principle*

still proportional to the number of primary electrons. A detector working in this region of proportional multiplication is called ***proportional chamber***. Increasing again the voltage, proportionality is lost. The energy becomes so large that a discharge occurs in the gas. The output current becomes saturated, always giving the same amplitude regardless of the number of initial ions-electrons pair. A detector working in this region is in the so-called ***Geiger-Müller mode***. Finally, if the voltage is still increased further a continuous breakdown occurs. This region is to be avoided to prevent damage to the counter.

Ionisation detectors are widely used in physics research. It is the reason for which the ionisation process and the movement of electrons and ions in gases have been and are still studied. The electrons and ions created by the incident particle itself are known as primary ionisations. In a number of these ionisations a sufficiently large amount of energy is transferred to electrons (delta-rays) such that they also creates ion-electron pairs. These latter ionisations are known as secondary ionisations. If their energy is high enough the secondary ionisation electrons may also ionise and so on until the threshold for ionising reaction is reached. The occurrence of the process is statistical in nature thus two identical particles will not produce the same number of ion-electron pairs. The average number of primary pairs is not equal to the energy loss divided by the ionisation potential since some energy is also lost through excitation. For gases, this average turns out to be of the order of 1 ion-electron pair per 30 eV of energy lost. The surprise is that

this average value does not depend very strongly on the particle type and only weakly on the gas type. While the number of ion-electron pairs created is important for the efficiency and for the energy resolution of the detector, it is also important that these pairs remain in a free state long enough to be collected. ***Recombination*** and ***electron attachment*** hinder this collection phenomenon. As already noticed, in absence of electric field, ion-electron pairs recombine under the force of their own electric attraction. In a similar way, positive ions recombine with negative ions or with electrons. The decrease of density with time can be described by the relation

$$-\frac{dn}{dt} = \alpha n^{+} n^{-} \tag{3.1}$$

with n^+ and n^-, the positive and negative charged particles densities [m^{-3}] and α, the recombination coefficient [$m^3 s^{-1}$]. Gas molecules with several atoms are able to accumulate electrons of low energy (eV). This is called electron attachment [40]. The probability of occurrence during one collision is negligibly small for noble gases, for N_2, H_2, and CH_4, but not for electronegative gases like O_2, Cl_2^-, NH_3 and H_2O. Therefore the presence of any electronegative gases in the detector will diminish the efficiency of ion-electron collection by trapping the electrons before they can reach the electrodes.

In gases, ions and electrons experience ***diffusion*** and, in presence of electric field, ***drift motion*** [37,38]. These motions are described by the classical kinetic theory of gases. In the absence of electric field, electrons and ions liberated by crossing particles diffuse uniformly outward from their point of creation. In multiple collisions with the gas molecules they lose their energy. They thus come into thermal equilibrium with the gas and eventually recombine. The linear distribution of charges, dN/dx, after a diffusing time t can be shown to be gaussian,

$$\frac{dN}{dx} = \frac{N_0}{\sqrt{4\pi Dt}} \exp\left(-\frac{x^2}{4Dt}\right) \tag{3.2}$$

with N_0 the total number of charges, x the distance from the point of creation [m], D the diffusion coefficient [$m^2 s^{-1}$].

If three dimensions are considered, the spherical spread is given by

$$\sigma(r) = \sqrt{6Dt} \tag{3.3}$$

where r is the radial distance. The diffusion coefficient is a parameter which can be calculated from kinetic theory and can be shown to be

$$D = \frac{1}{3} v\lambda \tag{3.4}$$

with v the particle velocity [ms^{-1}], λ the mean free path of the ion or electron in gas [m]. In the presence of an electric field, the ions and electrons are accelerated along the field lines toward the cathode and the anode, respectively. Collisions with gas molecules limit their maximum average velocity which can be attained along the field direction. This limit is known as the drift velocity. It is superimposed upon the normal random movement. Compared to the thermal velocities, the drift speed of the ions is slow while for electrons this can be much higher since they are much lighter. One usually defines the mobility of a particle as

$$v^{+/-} = \mu^{+/-} \frac{E}{P} \tag{3.5}$$

with v, the particle velocity [ms^{-1}], μ, the particle mobility [$m^2 atm V^{-1} s^{-1}$], E, the electric field strenght [Vm^{-1}], P, the gas pressure [atm]. The mobility for electrons is much greater than for ions. For electrons, their gain in velocity may also affect the diffusion rate if their mean energy exceeds thermal energies. This results in an increase of the diffusion parameter causing a greater spread of the electrons cloud. Before closing this part on ionisation detectors, the phenomena occurring at electrodes are briefly mentioned. Here a two electrodes system is considered [38]. The negative charges are neutralised without problem on the anode surface. It is simply an exchange of electron with a metal. The positive ion neutralisation at the cathode surface needs an electron extraction. This phenomenon liberates some energy: the difference between the ionisation energy and

work function. This last is defined as the energy necessary to extract one electron from the metallic surface. The liberated energy could be used for example for photons emission. This ionic bombardment of the cathode produces secondary electrons that cross the sensitive volume and then are collected at the anode. However the probability of this effect is very small, it could play an important role in the proportional and Geiger-Müller counters. Another effect occurring at the cathode is the Malter effect. It happens in presence of a thin insulating or with very high resistivity layer covering the surface. If the ionic bombardment on this "dirty" wall goes over a certain threshold, some positive ions cannot be neutralised very fast. They accumulate creating an electric field across the layer. Electrons are extracted from the cathode by this electric field, go across the thin insulating layer and penetrate the sensitive volume of the counter.

The ionisation chamber can operate in a pulse or in a current mode. In the first case the pulse induced by each incident particle is measured independently. In the second case the average dc current produced by the sequence of incident particles is recorded. The average dc current is proportional to the incident flux. The value of the electric field strength must be such that the positive and negative charges formed along the crossing particle path are all collected and that no secondary ionisation due to the drifting electrons takes place. All the phenomena mentioned above apply for the ionisation chamber. The monitor that will be tested, will run in current mode when used as a ionisation chamber. For many years the ionisation chamber was the device employed to monitor beams. But it shows a limit in linearity between the primary particles flux and the collected charge. Extension of the linear range is commonly achieved by reducing both the density of the gas and the inter-electrode distance [41,42].

3.2 Principle of the secondary emission chamber (SEC)

A SEC detector was first designed, developed and used as such by G. Tautfest and H. Flechter around 1954 [43, 44]. Then for many years the SEC has been the standard intensity monitor in proton external beam lines because, in particular, of its simplicity, its radiation hardness and its linearity over many orders of magnitude. The SEC operation is

based on the secondary electron emission (SEE) process. SEE effect was discovered by Austin and Starke in 1902 in the course of studies on the reflection of fast electrons from metals[45]. In most general sense, secondary electrons emission refers to the ejection of electrons from matter (metal or insulator) bombarded by rapidly moving particles such as electrons, ions or neutral atoms. Upon increasing the angle of incidence of the primary electrons away from the normal, Austin and Starke observed that the current into the target first decreased to zero and then actually reversed. Their conclusion was that not only the incident electrons reflected but other electrons are also ejected such that the total number leaving exceeds the number arriving. The effect was found to be proportional to the number of primary electrons, more pronounced for metals of high density and to increase with the angle of incidence. In 1903, P. Lenard showed that the secondaries possess low energies of the order of a few volts independent of primary energy or target material. He noticed that the yield, or number of secondaries per incident particle, goes through a maximum at a few hundred volts. He pointed out also that the process occurs in insulators as well as metals. In 1905, J. J. Thomson demonstrated the emission of secondary electrons from solids under ion bombardment. He established that the phenomenon is very similar to the electrons bombardment case. The secondaries were again found to have energies of a few volts, essentially independent of the nature of the incident ion, its velocity or the properties of the target. In 1911, N. R. Campbell established the same characteristics for the electrons emitted with α particles.

The process of SEE could be divided into three steps[46]. First, the absorption by the target of incident particles and the inner electrons excitation. Some of these electrons receive enough energy to be knocked out from the atoms. The highest energetic ones, or delta rays, can themselves produce secondary ionisations. Second, the secondary electrons diffusion toward the target surface with energy loss through inelastic collisions. The probability of reaching the surface decreases with the depth at which the secondary electrons are created. Finally some of the secondary electrons can go over the surface potential barrier. As an example, the situation of incident electrons at low energy (200 eV) is presented (see figure 3.2). The total flow of secondaries is composed of true secondaries with an energy independent of the primary energy (mean value of about 10 eV, see figure 3.2, region I), of primaries reflected inelastically with an energy loss of some tens of electron volts (see figure 3.2, region II) and of primaries elastically scattered

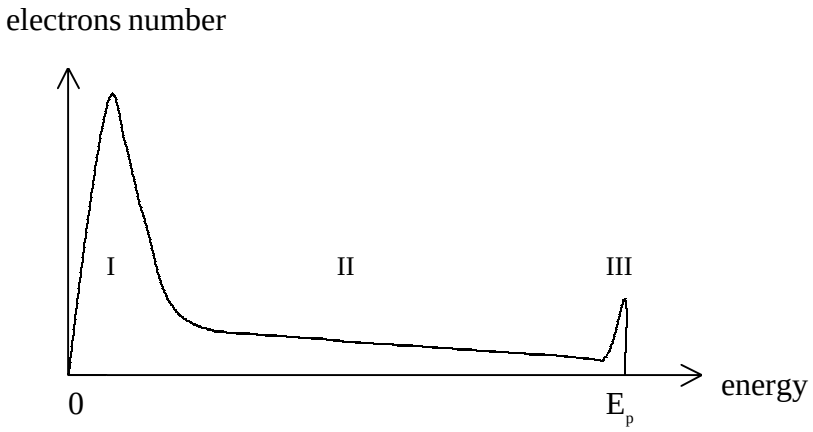

Figure 3.2 *Sketch of the secondary electrons energy distribution for electrons as incident particles.* ***Area I, (0<E<50 eV)****: "true" secondary electrons;* ***Area II, (50 eV<E<Ep):*** *electrons which have lost their energy after few inelastic collisions and excited electrons from the target; it is not possible to distinguish ones from the others;* ***Area III, (E=Ep):*** *"elastic pic"; electrons diffused elastically keeping the same energy than the incident beam; only their trajectory after the elastic collision with the crystal lattice has changed.*

(see figure 3.2, region III). Electrons with an energy up to 50 eV are usually considered to be true secondaries. For a primary beam of 200 eV, reflected electrons (~10% of all emitted electrons) have their energy near that of the bombarding beam. True secondary electrons (~90% of all emitted electrons) have their energy ~15eV [46-48]. For the general case of charged particles other than electrons as incident particles, when a particle crosses the medium it loses energy via ionisation or excitation processes (see § 2.2.1). This is described through the Bethe-Bloch formula [49]. dE/dx is independent of the mass of the incident particle, varies as $1/v^2$ at non-relativistic velocities and, after passing through a minimum, increases logarithmically with γ. The relativistic rise could be explained by the fact that the transverse electric field of the particle is proportional to γ, so that more and more collisions happen as the energy increases [49].

The estimation of the secondary electrons emission yield can be divided into two parts [46]. First, the computation of the number and of the energy distribution of the secondary electrons. Second, the analysis of the transport process which determines the movement of the secondaries and their collisions with the electrons and ions in the material. Only the electrons whose momentum component perpendicular to the surface is large enough to overcome the work function can leave the material. There are two types of energy loss that can occur in metals[50], namely inelastic and elastic collisions as mentioned above. Since, in metals, any amount of energy can be transferred to a valence electron in a single collision, it takes only a few collisions to reduce the energy of a secondary below the minimum value necessary to overcome the surface potential barrier. Thus, it is to be expected that the physics of inelastic collisions determines the depth from which the secondaries can escape from metals. The most important characteristic of a SEC is its efficiency or yield δ. It is the ratio of the total flow of secondaries to that of the primaries. δ is affected by the status of the surface. By roughening the surface δ is decreased. For pure metals δ remains below 2 while for metal oxides on a metal base it could exceed 30. The most probable energy of the escaping electron has been measured to be of the order of electronvolts (5-10 eV) and the maximum depth below the surface from where secondary electrons can escape is in the order of 10^{-8} m [42]. Therefore the SEE due to incident charged particles of high energy is a surface phenomenon independent of the foil thickness. The experimental results can be explained by the fact that a primary electron can only excite some electrons and the probability of excitation per unit length decreases with electron velocity [47]. A slow incident electron loses its energy near the surface, so the excited electrons can, if their momentum is opportunely directed, leave the material since they do not need to cover a large distance. Higher energy electrons penetrate deeper into the material and release a larger number of secondary electrons, many of which lie so deep in the material that they have no chance to reach the surface. Thus the gain decreases when the energy of primary beam exceeds a certain value. The high absorption power for electrons of metal surfaces is a consequence of partially filled metal conduction bands. Thin isolating metal oxide layers have no free states in the valence band and thus cannot absorb the excited electrons, which easily leave the material.

The principle of operation of a SEC is presented in figure 3.3. When a charged particle passes through a thin foil of metal, SEE occur. The foil surface is then an electron

emitter. Another foil positively biased will collect these electrons and at the same time those emitted from the bias foil as well. Collection is optimised when in vacuum. A sketch of a SEC previously used at CERN is presented in figure 3.4. Its conception, design and construction were based on three imposed conditions: an overall minimum mass in order to avoid too much interference of the monitor with the beam optics, the ability to be bakeable and a good resistance to radiation damage [42]. Table 3.1 gives the main characteristics of the three different models of SEC (SEC 5, SEC 20 and SEC 40) constructed previously at CERN. Hereafter we report some performances of the SEC 5 [42]. However no significant differences were observed between the SEC 5 performances and those of SEC 20 and SEC 40. Tests were performed with beam of proton of ~17 GeV/c. There is very little variation of SEC efficiency over the whole useful foil surface. There is about 2% SEC efficiency difference between the position where the protons have hit the SEC foils for a long time and the SEC efficiency of the

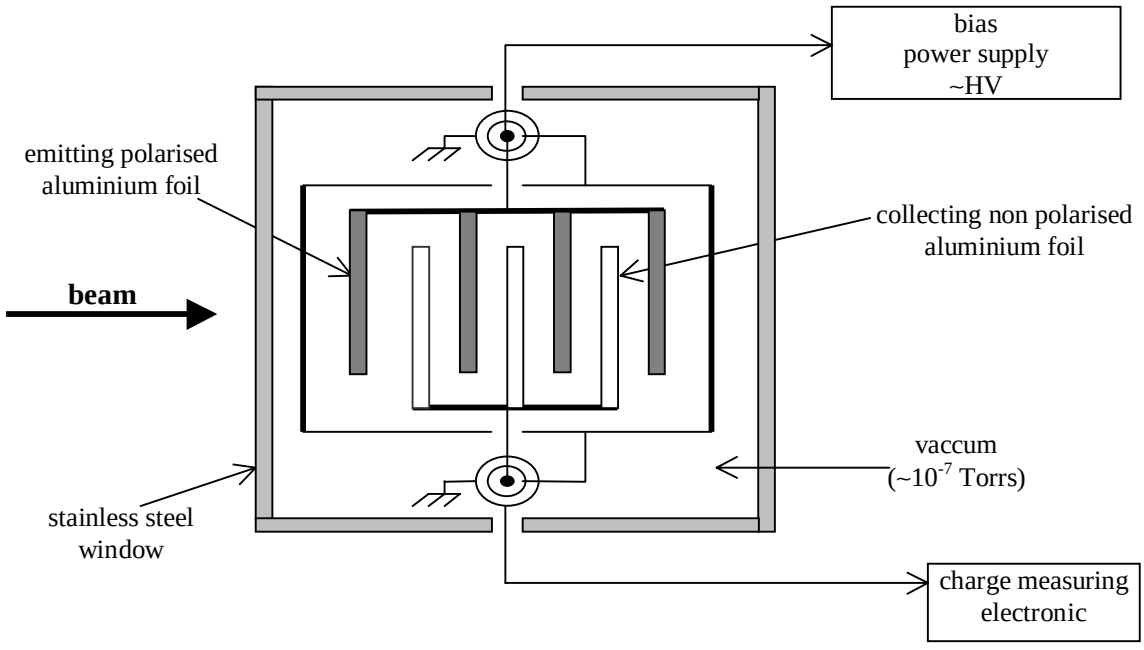

Figure 3.3 *Principle of secondary emission chamber with the triaxial configuration*

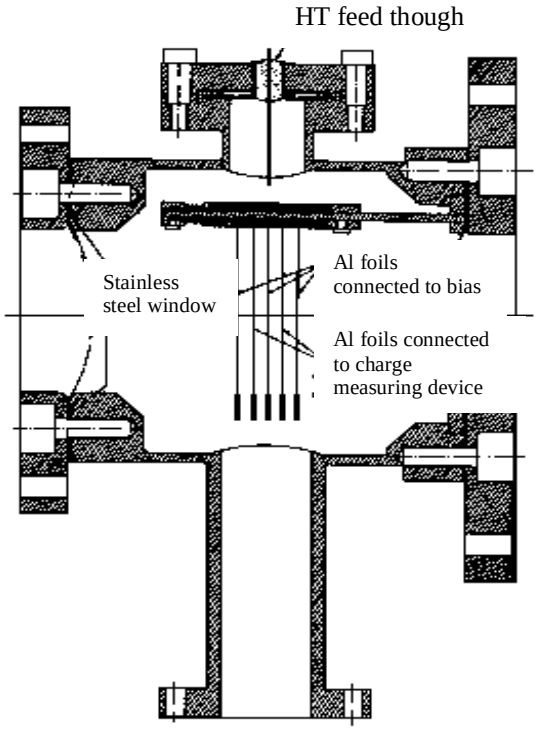

Figure 3.4 *Sketch of the previous SECs constructed at CERN* [42]

rest of the foils. The bias curve (SEC efficiency against bias voltage) shows that efficiency goes up very rapidly presenting an insignificant overshoot at ~20V for positive bias and a similar one at ~0.5 V for the negative bias. This discrepancy is believed to be a consequence of the measuring method. In our tests, this phenomenon was not observed. The "plateau" is reached at about 10 V. An excellent plateau is often reached for both positive and negative bias as high as ± 2.5 kV. A bias of 500 V is generally used for normal operation. The linearity of the SEC efficiency against the incident protons is good. No saturation was observed up to 10^{18} protons $cm^{-2}s^{-1}$ [42].

Table 3.1 *Characteristics of the three kinds of SEC previously constructed at CERN* [42]

Model or name	Number of foils		Nature and thickness of each foil	Nature and thickness of the window	Useful diameter	remarks
	Total	Emitting				
SEC 5	5	2	Al 5μm	Stainless steel 25 μm	62 mm	
SEC 20	21	10	idem	idem	120 mm	+ 20 foils with concentric holes of 40 mm diameter
SEC 40	41	20	idem	idem	62 mm	2 sets of 10 emitting foils each

3.3 Design and construction of the new prototype

We describe hereafter mechanical and electronic aspects of a monitor which has been used first as a SEC and then as an IC by filling the chamber with gas (argon at atmospheric pressure). The conception and design of the monitor are based on thoses of previous SECs used for years at CERN [42]. The overall mass of foils and windows has to be kept to a minimum. It determines, in a way, the monitor dimension, the foil material and the window material. The SEC has to be bakeable, in order to help outgassing to obtain high vacuum and clean surfaces. Finally, it has to present good resistance to radiation damage. Before presenting the monitor construction, the improvements of the new prototype are pointed out.

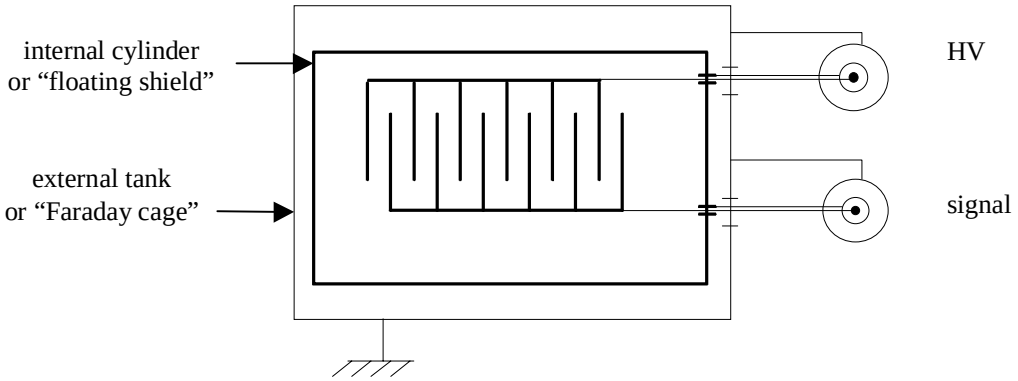

Figure 3.5 *Triaxal configuration of the new prototype*

Our prototype differs from previous SECs in two main characteristics. First, the addition of an insulated stainless steel cylinder inside the old vacuum tank (see figure 3.5) and second, the use of triaxial connections. The aim is to minimise leakage currents, mass loops and noise pick-ups. The external tank acts now as a Faraday cage, it isolates the monitor electrodes (aluminium foils) from the external electromagnetic noise while the internal cylinder acts as a “floating” shield.

Table 3.2 reports some technical specifications of the monitor. The chamber is presented at figure 3.6. It is a flanged stainless steel cylinder (see figure 3.6, flanges A and B). Flanges A and B, respectively, support an external flange (dotted lines, Abis and Bbis). Each of these two external flanges include a window foil (curved dotted line). These window foils are stainless steel, 25 μm thick. They make the vacuum sealing. The chamber components are chosen to withstand bake-out temperature of the order 300°C, however 250 °C were found sufficient for an efficient outgassing. The flange C on the top of the external tank is a “four-ways“ flange which allows the signal output, the polarisation input and the vacuum system connections. All the flanges used are Ultra High Vacuum (UHV) standard (CF flanges). All the internal parts of the SEC are assembled on a stainless steel ring, part of one side of the SEC window flange. On this

Table 3.2 *Technical specifications*

foils	21 (11 emitting electrodes,10 collecting electrodes) Al (99% purity) thickness: 10 μm used diameter: 120 mm spacing: 5 mm
insulation	ceramic (macor and alumine Al_2O_3) thickness: 3mm
other pieces	stainless steel (304 L type)

ring, six insulator cylinders are fixed (60º apart). They are made of macor, a material easy to shape with good thermic and dielectric coefficients. After backing, it presents the same structure as ceramic. On each of these insulators, stainless steel bars are screwed, serving as passive supports of the foil assembly. The 21 Al foils are mounted on circular stainless steel frames. These frames consist of two rings which, when assembled, hold the foils tightly. The parts of the frame are shown in photo 1. Insulation of the foils between themselves and the bars is assured by alumine Al_2O_3. The electrical inter-connection of each foil frame and the corresponding feed-through is by contact and free from soldering. The whole foil assembly is fixed in an internal cylinder called “screen support” acting, as already mentioned, as a “floating shield” (see figure 3.6, G).

Two prototypes have been built. They differ in the insulation mode between two consecutive electrodes (see figures 3.7a and 3.7b). In prototype 1, insulation is assured by ceramic while vacuum or gas is used in prototype 2.

The easiest way to describe the chamber is to follow the construction procedure which can be divided into four main steps. All the mechanical parts must be cleaned (considering UHV conditions) before the assembling.

The assembling procedure is the following. **Step 1**: the aluminium foils are mounted on circular stainless steel frames in clean environment. They form the monitor electrodes (see photo 1). **Step 2**: twenty one electrodes are piled up on six support bars (see photos 2 and 3). Then, each collecting electrode is surrounded by two emitting ones.

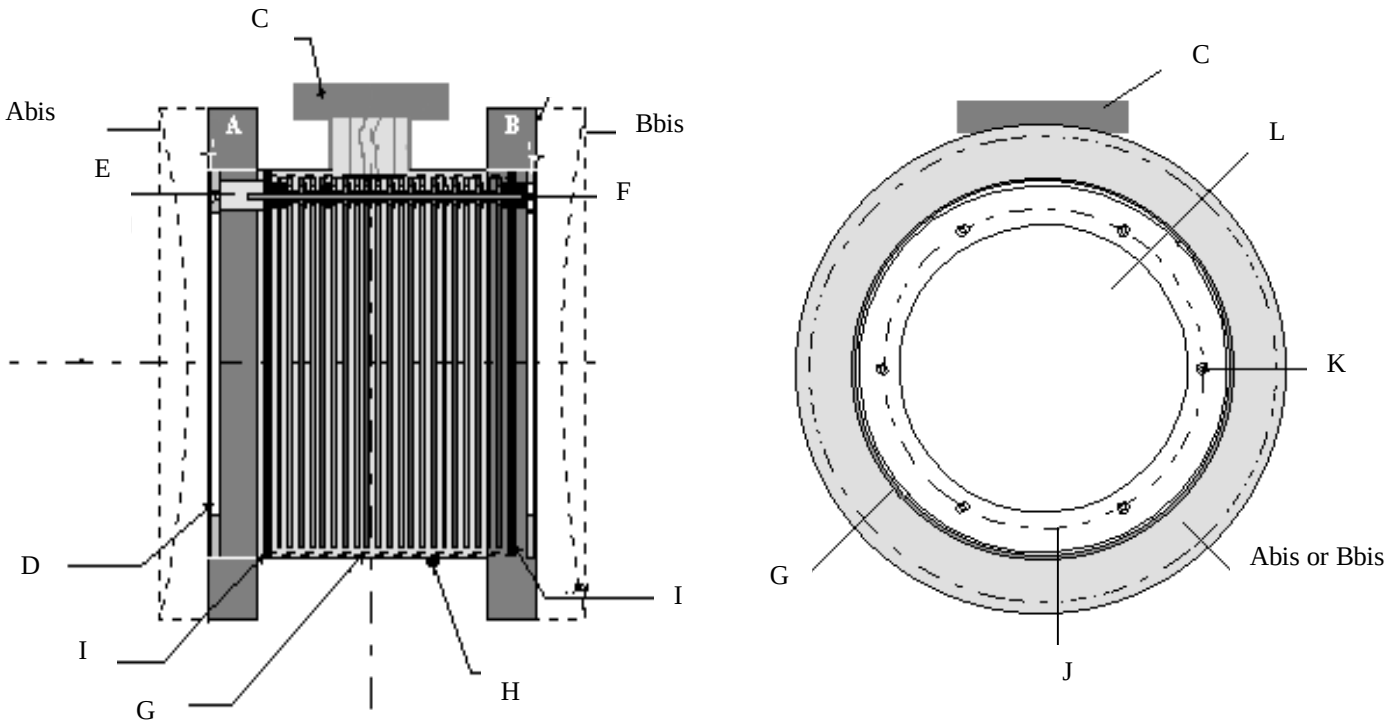

Front view **Side view**

***A, B**: internal flanges*
***Abis, Bbis**: external flanges*
***C**: "four-ways" flange*
***D**: triaxial detector support*
***E**: insulator cylinder (x 6 at 60º)*
***F**: stainless steel bar (x 6 at 60º)*
***G**: internal cylinder or "floating shield"*
***H**: external tank or "Faraday cage"*
***I**: electrodes assembly support*
***J**: Aluminium foil frame*
***K**: stainless steel bar position*
***L**: Alumimium foil*

***Figure 3.6** New prototype sketch*

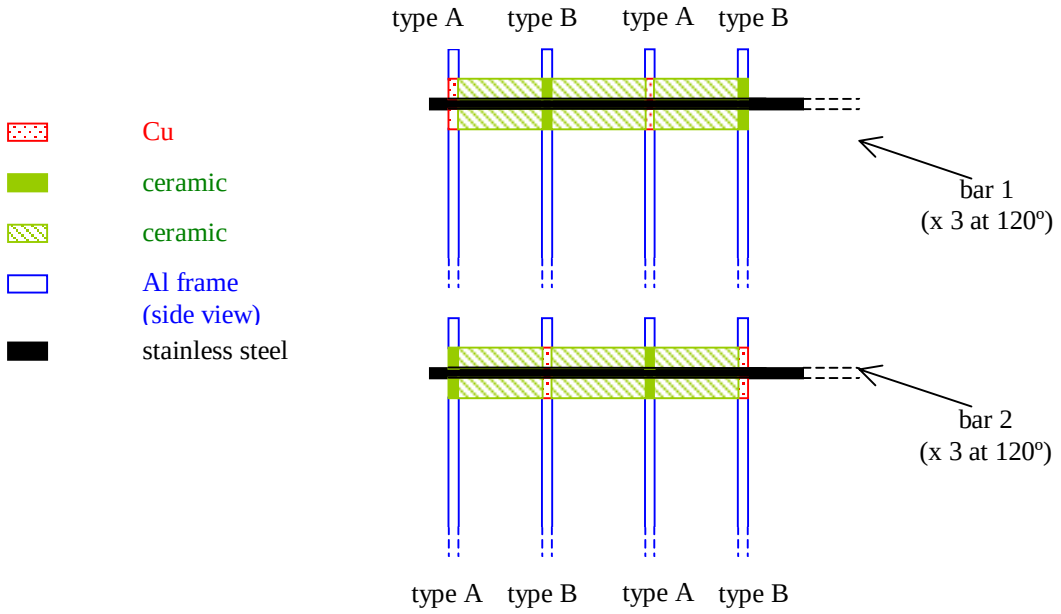

Figure 3.7a *Insulation sequence for prototype I. If the Al frame type A corresponds to the emitting electrodes then the B type stands for the collecting ones (or inverse). Bars 1 and 2 are 60º apart.*

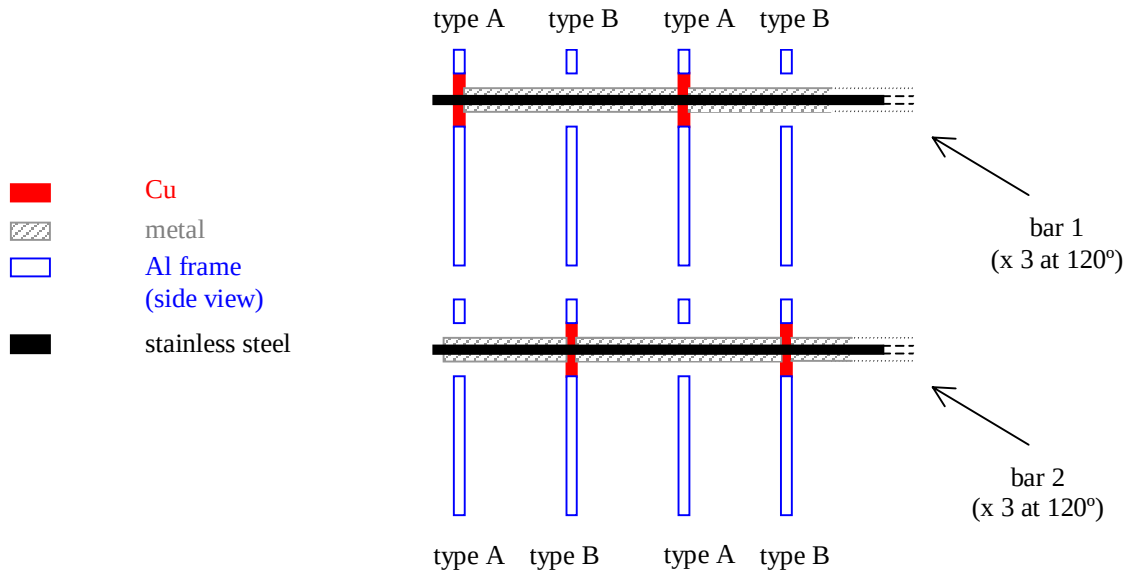

Figure 3.7b *Insulation sequence for prototype II. If the Al frame type A corresponds to the emitting electrodes then the B type stands for the collecting ones (or inverse). Bars 1 and 2 are 60º apart.*

Step 3: introduction of the "electrodes block" in a stainless steel cylinder which will act as a "floating shield" (see photo 4). **Step 4**: the overall assembly is inserted inside an external stainless steel tank which will act as a Faraday cage (see photo 5). In SEC mode, the vacuum inside the chamber will be 10^{-6}-10^{-7} Torr. The SEC was baked during 48 hours at 250 ºC. In IC mode, the chamber will be filled with argon at atmospheric pressure.

As previously explained, 11 Al foils act as emitting electrodes and are connected to the bias voltage while the other 10 foils act as collecting electrodes and are connected to the charge measuring device. The gap between two consecutive foils is 5 mm. Aluminium has been chosen as electrode material. This choice results from a compromise between radiation hardness (or ageing effect) and efficiency. Irradiation tests have been performed with different types of foils[51]: aluminium, titanium, gold, gold coated aluminium and titanium (see figure 3.8). Exposed to about 10^{20} p/cm^2, their SEE has been measured regularly. The Ti SEE is the lowest but the most stable one with a variation of only 0.5% in the range of 10^{16} p/cm^2 to 10^{20} p/cm^2 for integrated proton density while the Al SEE is the highest one but with a drop of around 40% above 10^{18} p/cm^2. The slight increase for titanium at 10^{18} p/cm^2 is not yet understood. Figure 3.8 allows to draw the conclusion that below a flux of 10^{18}p/cm^2 Al foils are good candidates because of their higher SEE. Considering that LHC will run at the nominal luminosity of 10^{34} cm^{-2}s^{-1} during 180 days each year, the incident flux of charged particles on the monitor will be after 10 years around 10^{15} particles/cm^2 [52]. Figure 3.8 shows that this number is far from the threshold of radiation effect for all materials and that they will keep their nominal efficiency. Because of this, of the facility to shape it and its low price, Al has been chosen as the electrode material. Note, however, that Ti foils are the best choice for high density flux because of their stability. As seen above, SEE is a surface phenomenon, thus, one of the important factors on SEC efficiency is the condition of the foil surface as well as the foil material itself. Large SEC efficiency drifts are observed each time a SEC is opened to air and pumped again [42]. The contamination which can derive from the pumping procedure, can be extremely harmful. For instance, in a vacuum system using diffusion pumps, there is an unavoidable oil deposit on the surface of the foils and the chamber walls. In view of these considerations, a dry vacuum system was adopted. This vacuum system is simple of operation, with small dimension and small weight. It is almost free from maintenance.

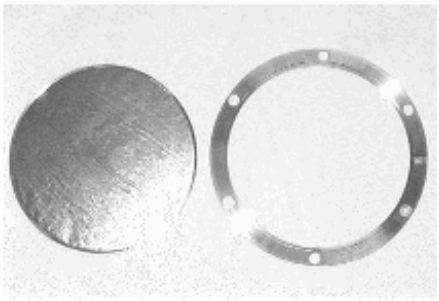

Photo 1 *Aluminium foil on stainless steel frame*

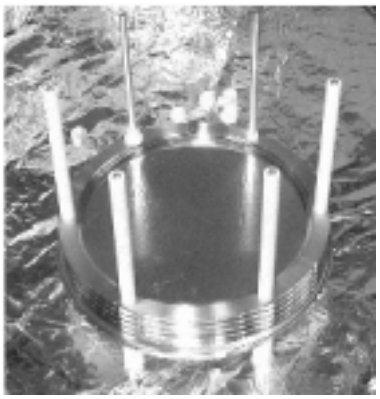

Photo 2 *Electrodes pile-up: intermediate step*

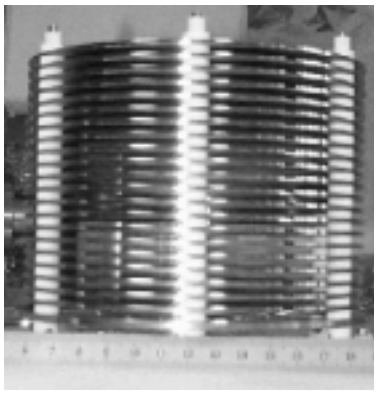

Photo 3 *Electrodes pile-up: final step*

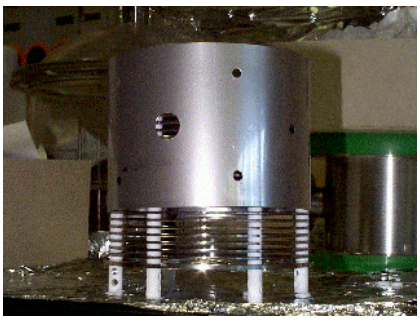

Photo 4 *Insertion inside the internal cylinder*

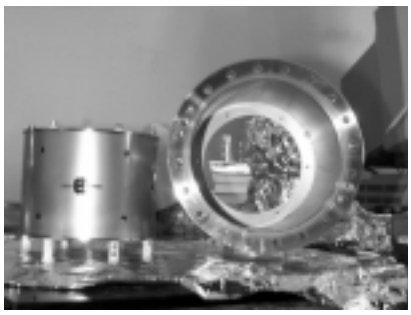

Photo 5 *Insertion inside the external tank*

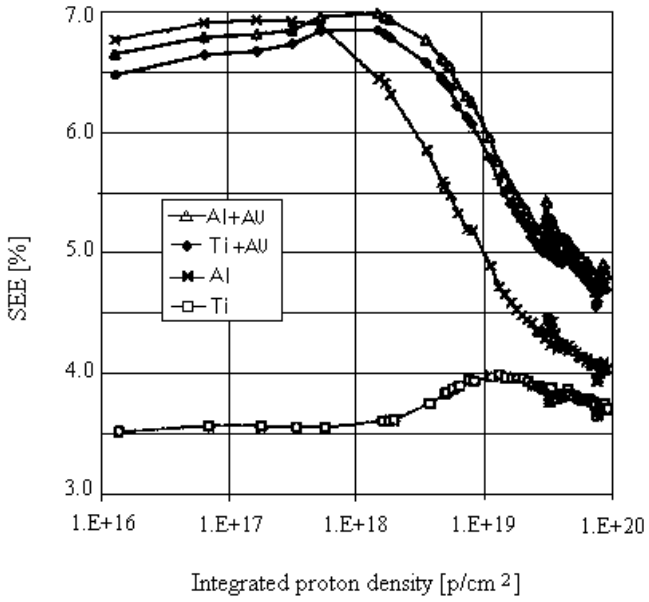

Figure 3.8 *Change in SEE with irradiation for aluminium (Al), titanium (Ti), gold coated aluminium (Al+Au) and gold coated titanium (Ti+Au)* [51]

A block diagram of our **electronic chain** is presented in figure 3.9. The detector current, I, is integrated (IVC102 integrated circuit) and the corresponding charge is transformed into a periodic signal whose frequency is proportional to the charge (AD650). After this, the number of pulses is counted during a fixed time delay. The counting time, Δt, is determined by monostables. For instance the counting is done on a window larger than the extraction time. The IVC102 is a gated integrator, it gives no signal in absence of beam. The system is not sensitive during the reading period.

As already mentioned, the luminosity monitor will work at luminosity between $10^{28}cm^{-2}s^{-1}$ and $10^{34}cm^{-2}s^{-1}$. Appendix D shows that the corresponding monitor output current (or electronic input current) will be between $10^{-15}A$ and $10^{-9}A$. The present limit for standard electronics is a measurement of current down to $10^{-12}A$. Below this threshold we face the effect of electromagnetic noise. The challenge is to measure low currents (from $10^{-13}A$ to $10^{-15}A$). The electronic components were thus chosen with the lowest intrinsic

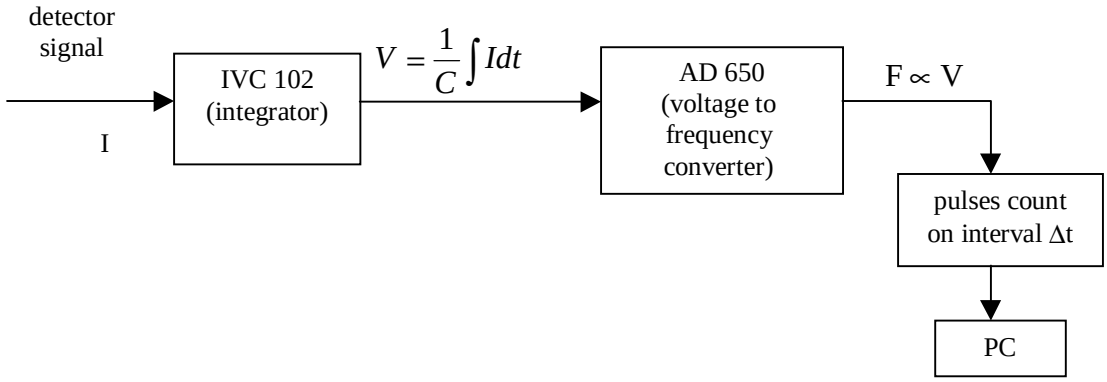

Figure 3.9 *Electronic chain sketch*

noise. The **IVC102** is a precision switched integrating amplifier with Field Effect Transistor (FET) operational amplifier, integrating capacitors and low leakage FET switches. It integrates low-level input current, I, of positive or negative charges (bipolar) for a user-determined period, t, in a capacitor, C. The output voltage is

$$V = \frac{1}{C}\int_0^t Idt = \frac{1.6 \cdot 10^{-19} N}{C} \qquad (3.7)$$

with N the number of charges at the output of the detector. Its important features are a low input bias current (100 fA), a low noise, a low charge injection when opening and closing the switches, a fast pulse integration, an important bandwidth and a good linearity (0.005% over the full range). Because of such performances and, in particular, of the very low input bias current, one has preferred the IVC102 to others integrators or operational amplifiers used as integrators. The **AD650** is a voltage to frequency converter (VFC). Its choice is linked to resolution and transmission. It provides a combination of high frequency operation and good linearity previously unavailable in monolithic circuits. The combination of these two features makes it an inexpensive solution for applications requiring analog to digital conversion. The linearity depends on the frequency. It is of

0.002% at 10 KHz and of 0.07% at 1 MHz. The maximum AD650 output frequency is 1 MHz. The AD650 digital precision is one part to 10^6. The signal can be transmitted over a long distance with just one cable. A counter gives directly the output signal value. More information on the IVC102 and AD650 characteristics are given in appendix E and F, respectively.

The **logic of the electronic chain** can be divided into two sub-circuits (A and B in the block diagram on figure 3.10; complete logic circuit is given in appendix G). The bi-directional connection between circuits A and B is assured by a coaxial cable. Synchronously with the accelerator phase, a trigger signal is sent by circuit A, physically located in the "control room", to circuit B, located in the tests beam zone. At that moment, the acquisition gate is activated (the IVC102 output voltage increases proportionally with the integrated charge). At the end of a fixed delay, the gate is closed. The IVC102 output voltage is stable and the readout is activated. The output voltage is converted into frequency by the AD650 and sent back to the counter in circuit A. At the end of the reading, the system is reset. The IVC102 output voltage is set to zero. The timing unit disables the trigger during the acquisition and the reading periods (i.e. 0.5 s at the PS and 2.5 s at the SPS). A complete acquisition and reading cycle is over after ~ 0.6 s at the PS and ~ 2.6 s at the SPS. The next one will begin with the next trigger arrival.

A possible limitation in the acquisition could come from the mismatching between the temporal distribution of the incident particles and the "slew rate" of the integrator IVC102 (see appendix E) which gives a voltage value proportional to the amount of incident particles. Its slew rate value (in general of 3V/μs but here limited to 2.5 V/μs) implies that a maximum of 1.5 10^8 particles can be integrated over 1 μs. The burst length and the burst maximal intensity are, 2.5 s and 10^8 particles, respectively, at the SPS while we have 0.35 s and 8 10^5 particles at the PS. Thus, our working range corresponds to a maximum of ~ 40 particles to be integrated over 1 μs at the SPS and a maximum of ~ 3 particles to be integrated over 1 μs at the PS. These values are far below the slew rate value. Thus no limitation is expected during our tests.

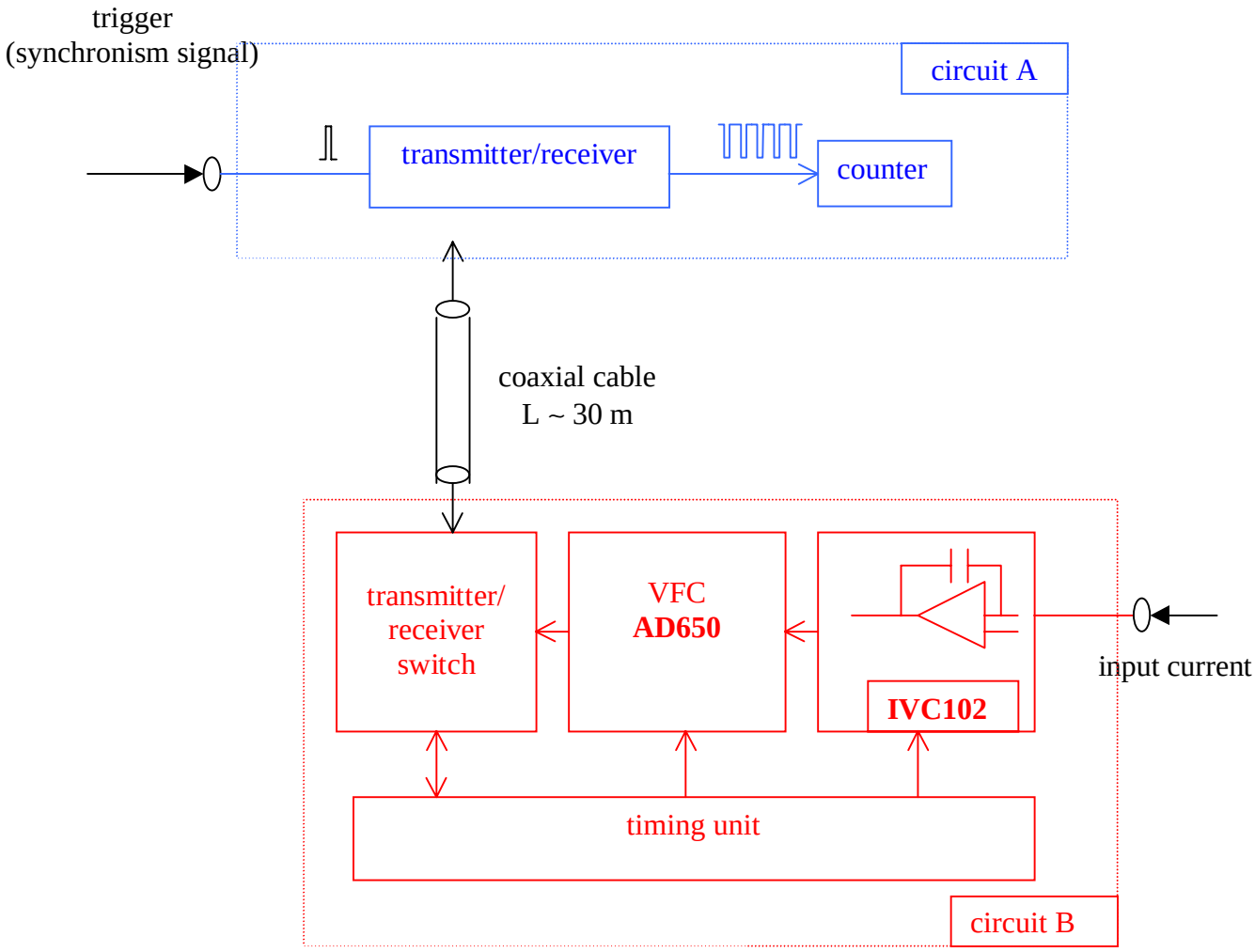

Figure 3.10 *Electronic block diagram*

Chapter 4 Experimental set-up

Tests of our prototype were performed at CERN on the PS-T11 and the SPS-H6 beam lines. We give a short description of the beam facilities before presenting our results.

4.1 Beam lines specifications

4.1.1 PS-T11 beam line

At the PS, tests have been made in the East Hall Physics area on the secondary T11 beam line (see figures 4.1). T11 is derived from a 24 GeV/c primary proton beam F61 extracted from the PS straight section 61[53]. The secondary T11 beam is mainly composed of $p^{+/-}$, $\pi^{+/-}$, $K^{+/-}$ and $e^{+/-}$ depending upon the target choice. Beam polarity, momentum and intensity may be adjusted. Our tests were made with the maximum available intensity up to 8.10^5 particles per pulse at a momentum of 1.8 GeV/c for a secondary beam of π^+ and p^+ (see figure 4.2). It should be noted that the nature of the particles cannot be chosen. Only their charge can be selected. For our studies of the monitor dynamic range, it is necessary to work in the configuration which allows the largest intensity range. Four collimators arranged into two pairs (MCV01 and MCH01, see figure 4.3), placed upstream of the experimental hall, allow to change the beam intensity. The first pair, MCV01, cuts the beam top and bottom while the second one, MCH01, cuts the left and right parts. Beam steering and focalisation are respectively performed by dipoles and quadrupoles magnets. In particular BHZ02 and BVT01 assure, respectively, horizontal and vertical steering while QFO04 and QDO05 allow to tune the beam size. Collimators and magnets are monitored from the EBCR (East Beam Control Room). This control room delivers also the timing signals. The prepulse or warning pulse is around 50 ms before the extraction spill (~ 350 ms long). Typical repetition rate is 1 to 2 spills in 14.4s (PS “super cycle”) and minimum repetition time is 2.4s (“B cycle”).

During the tests the extraction spill was not regularly spaced in time, in particular when running in parasitic mode.

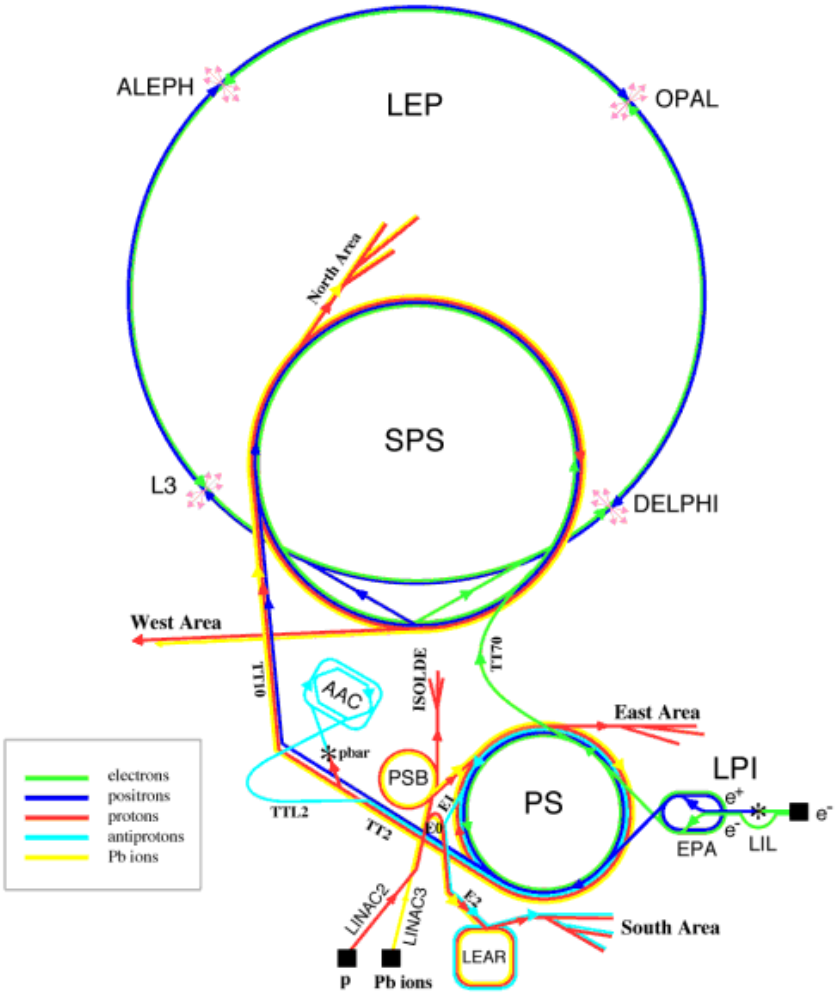

LEP: Large Electron Positron collider
SPS: Super Proton Synchrotron
AAC: Antiproton Accumulator Complex
ISOLDE: Isotope Separator OnLine Device
PSB: Proton Synchrotron Booster
PS: Proton Synchrotron
LPI: Lep Pre-injector
EPA: Electron Positron Accumulator
LIL: Lep Injector Linac
LINAC2: LINear Accelerator 2
LINAC3: LINear Accelerator 3
LEAR/LEIR: Low Energy Ion Ring

***Figure 4.1** CERN accelerators complex* [54]

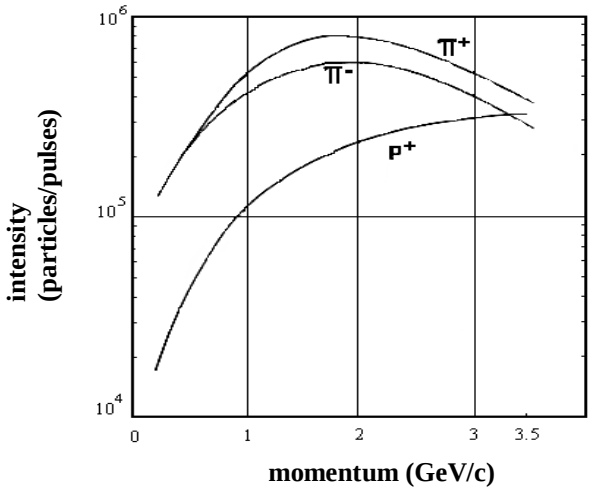

Figure 4.2 *Calculated intensity at the PS T11 beam line*[56]

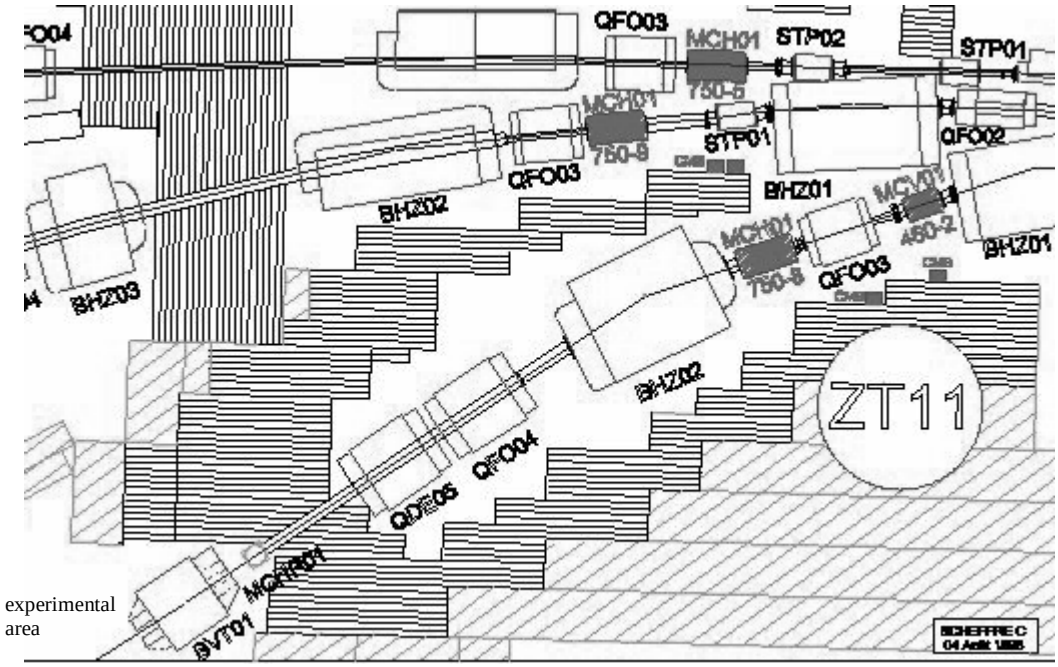

Figure 4.3 *PS T11 beam lines elements (top view)* [55]*. The experimental area is located after the last dipole BVTO1 at the bottom left of the figure.*

4.1.2 SPS-H6 beam line

At the SPS, tests have been made in the North area on the secondary H6 beam line (see figure 4.1). H6 beam is obtained from a 450 GeV/c primary proton beam extracted from the SPS and directed on the T4 primary target [57]. There are three distinct modes of operating the H6 beam: high resolution mode, high transmission mode and filter mode. For the tests, beam filter mode is used as it allows an easy change of the beam momentum by users in the control area PPE126 (see figure 4.4). Tests were made with a 120 GeV/c momentum secondary beam of positive particles (~1/3 protons and ~ 2/3 pions, with a few percent kaons). It corresponds to a maximum intensity around 10^8 particles per burst. The beam energy and composition are imposed by the machine and target characteristics. The beam intensity is adjusted by collimators monitored from the control area PPE126. Its value is confirmed by a Precision Ionisation Chamber (PIC) with an uncertainty of 4% [58]. The calibration of 2.2 10^4 particles per PIC count gives the minimal count capability of such a device. This count will be used as a reference. The beam line schematics upstream of the experimental area is given in figure 4.4. The extraction spill is 2.5 s long with a period of 14.4 s. The machine delivers a prepulse signal or "warning ejection" signal about 10 ms before each burst.

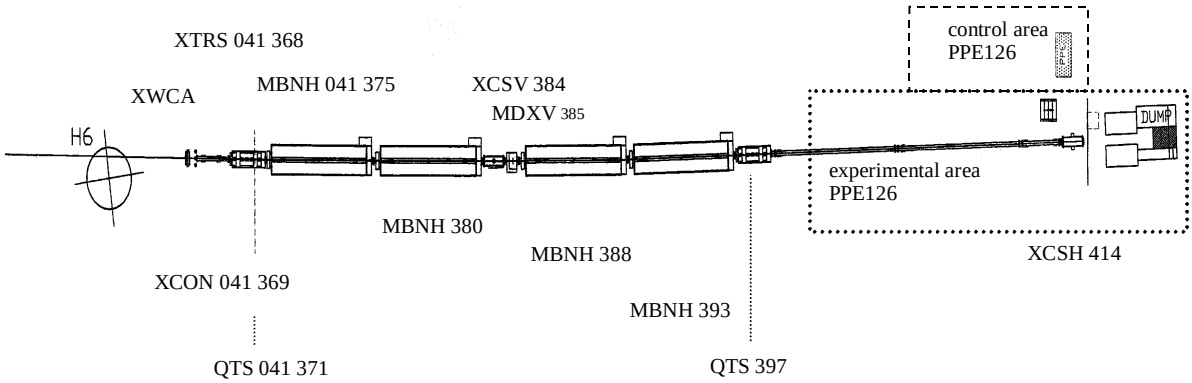

Figure 4.4 Last elements of the H6 beam line upstream of PPE 126 area (top view) [60]
XWCA: wire chamber; **XTRS 041 368**: scintillation counter; **XCON 041 369**: motorized lead absorber (always out during runs); **QTS x**: quadrupoles; **MBNH x**: bending magnets; **XCSV 384**: vertical collimator; **MDXV 385**: vertical steering**; XCSH 414**: horizontal collimator.

4.2 Experimental set-up

Our tests set-ups were essentially identical in the PS-T11 and the SPS-H6 beam lines (see figure 4.5). Two scintillators, S1 and S2 in coincidence, placed upstream of the monitor (SEC or IC) are readout by photomultipliers, PM1 and PM2. The coincidence signal is used as a reference. The scintillators surface is 10 cm^2 and their thickness, 1 mm or 10 mm, is chosen according to the beam intensity. In the PS-T11 line, a Multi-Wire Proportional Chamber (MWPC) is located upstream the scintillators in the experimental zone (see figure 4.3). This chamber is part of the beam line and cannot be removed. It allows the determination of the beam position and dimensions and makes sure that all the beam impinges on the monitor electrodes. More information on scintillators-PM assembling and on the monitor are given, respectively, in chapter 2 (see § 2.2.3) and chapter 3 (see § 3.3). In the SPS-H6, as already mentioned in the previous section, the PIC is located upstream the experimental zone (see chapter 5, figure 5.4). We have used the PIC information as a reference for the calibration of the monitor.

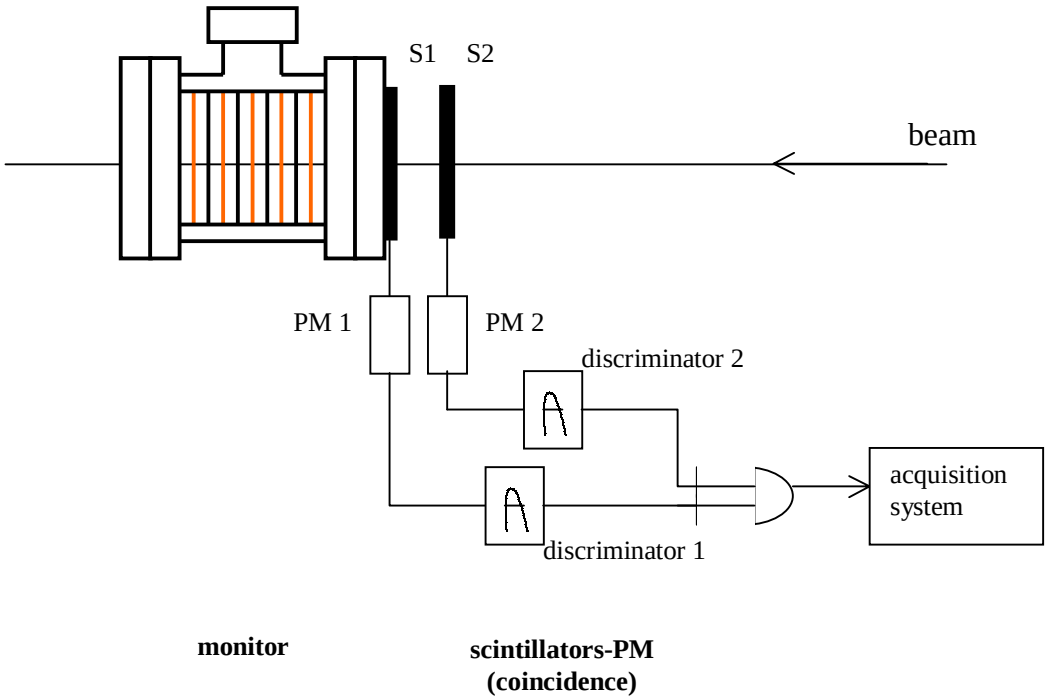

Figure 4.5 *Schematic side view of the experimental set-up*

4.3 Acquisition system

The acquisition system can be divided into two sub-systems: the electronics and the software sub-systems (see figure 4.6). The electronic sub-system adapts the data acquisition to the beam extraction characteristics (spill duration, cycle) while the software sub-unit counts and stores the data produced by the monitor and by the reference detectors (scintillators-PM or PIC). The monitor output current is converted into a pulse number (see §3.3). The reference detectors output are also converted into counts.

Our acquisition program cycle is started by a signal which is obtained by the "prepulse" delivered by the PS and the SPS and often referred as the "machine trigger" (see § 4.1 and figure 4.7). The same signal delayed by Δt is used to start an acquisition in a time window without beam. It is used for the determination of the "pedestal" of the measurement. A Keithley CTM-10 card is used to store in PC files the different signals emerging from the monitor, from the reference detectors and from the electronic sub-system. The Keithley CTM-10 is a multifunction counter-timer board with two AM9513A system timing controllers (units A and B)[61]. It performs event counting, pulse measurement, frequency measurement and pulse generation. It offers 10 independent, 16 bit, counter-timer channels with a maximum input frequency of 7 MHz. For each counter channel there are one input pin, one output pin and one gate pin (for connecting an external gate or an external trigger for event counting). It is thus possible to specify an external gate to determine when events are counted or to specify an external trigger to

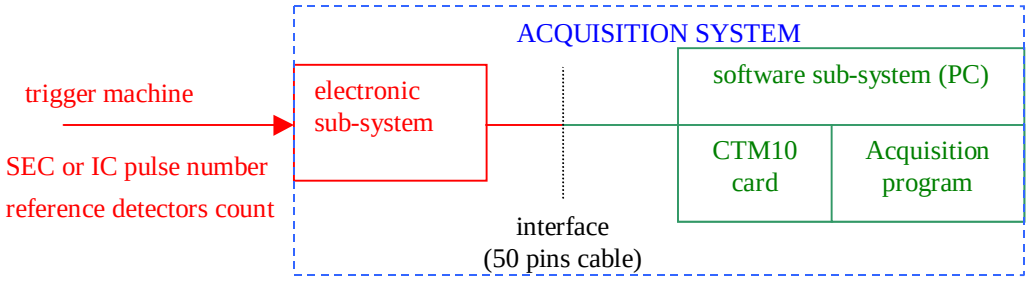

Figure 4.6 *Hard and soft systems integration*

initiate an event counting operation. The card is monitored through a program whose main steps can be summarised as follow. Each acquisition sequence (see figure 4.7) begins with a trigger coming from the electronic sub-system. **Step 1**: at the "machine trigger" arrival, $t_{trigger}$, all the CTM-10 channels are set to 0. **Step 2**: acquisition during a time, t_{window}, fixed by the electronic sub-system. **Step 3**: at t_{delay} data storage in files (t_{delay} is imposed by the software program). **Step 4**: waiting the next trigger. Note that for step 1, one of the 10 available channels is used as a "flag". Its status changes from 1 to 0 in coincidence with the trigger arrival, all the others channels are reset and enabled. Thus on the 10 available channels, 9 are used as counters and 1 as a "flag". As previously indicated, for each "machine trigger", the electronic sub-system creates a second trigger. Usually, the acquisition gate following the first trigger is centred on the beam spill while the second one registers the background (pedestal) between the end of the storage delay and the beginning of the next "machine trigger" (see figure 4.7). It allows us to have a

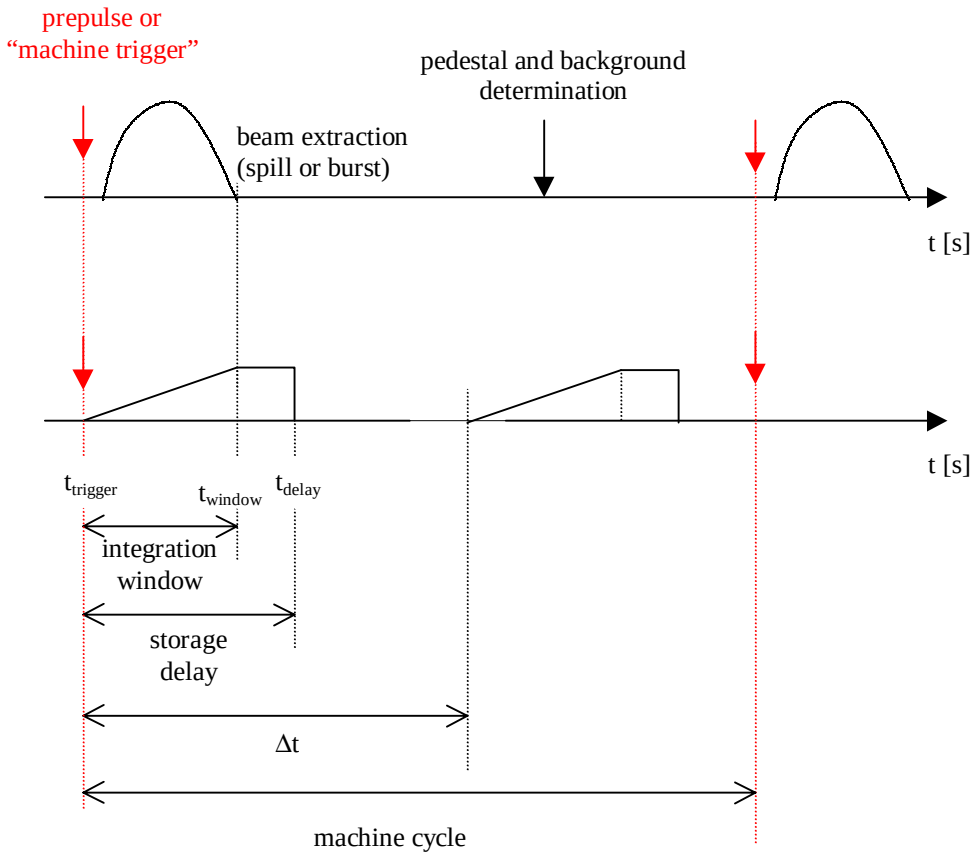

Figure 4.7 *Sequence of the data acquisition*

better estimation of the background associated to the signal. The integration window (t_{window}-$t_{trigger}$ in figure 4.7) is programmed to 0.5 s at the PS and to 2.5 s at the SPS. The stability of the window width is not important because the chosen delay covers the full spill. The synchronisation with respect to the machine trigger was at the nanosecond level.

Chapter 5 Reference detector setting up

As already mentioned during our tests, two pairs of scintillators are used in coincidence as reference detectors (see § 2.2.3 and § 4.2). Their working condition is quite critical for some of our tests. Some parameters as the PM voltage or the PM coincidence window are adjusted prior to any data acquisition. Hereafter the settings and the characteristics of the reference detectors are discussed.

5.1 The scintillation counters set-up

The scintillators are 10 mm and 1 mm thick, of plastic type developed by Nuclear Entreprises, model NE102A. The photomultipliers are the standard models used at CERN, the EMI9813KB with the alimentation base CERN-4238. The setup was done with a radioactive source (^{137}Cs of 3.5 MBq) in front of the scintillator surface. A well formed signal is obtained with a PM voltage between 1500 V and 2500 V. Our PMs are operated with negative high voltage i.e. their cathodes are at a negative potential with respect to their anodes which are at ground. This configuration allows to transmit directly the PM output signal to the read-out electronics without any decoupling device to adapt the signal level. Some ringing (i.e. small secondary pulses on the tail of the signal) is observed but their amplitude remains smaller than the threshold value of the discriminator (40 mV) used with the counter and they can be tolerated. The counter noise is measured by removing the source. Black tissue covers the counters during the tests in order to minimise light leak effects. A “plateau” measurement allows to find the best efficiency region. An experimental set-up sketch is presented in figure 5.1. The signal is generated by a radioactive source in the laboratory, whilst the beam itself is used during tests at the PS and the SPS. The figure 5.2 shows an example of a “plateau” measurement in the laboratory with a radioactive source of ^{137}Cs. At low voltages few counts are registered because the pulse heights are below the discriminator threshold. As the voltage increases, after a sharp rise, the curve enters a flat area called “plateau” where the counter

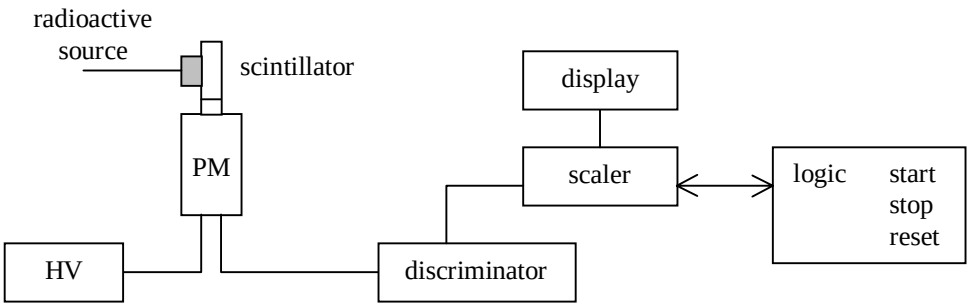

Figure 5.1 *Sketch of the experimental set-up for the "plateau" measurement in the laboratory. The radioactive source is replaced by the beam during tests at the PS and the SPS*

efficiency is optimum for polarisation between 2050 V and 2150 V. Then the curve rises again as the PM noise overtakes the discriminator threshold (both signal and noise are now recorded). Fixing the voltage on the "plateau" ensures an optimum efficiency of the counter and minimises the counting variations due to changes in the PM gain. In particular, the "plateau" depends on the threshold value of the discriminator and on the relationship between the PM gain and voltage. The "plateau" curve may vary if some changes occur in the beam conditions, in the electronics noise etc… The plateau condition is thus verified before each acquisition period. An example of such a procedure is presented in figure 5.3. In this case, the PM voltage was afterwards set at 2153 V for PM1, at 2081 V for PM2, at 2112 V for PM3 and at 2143 V for PM4.

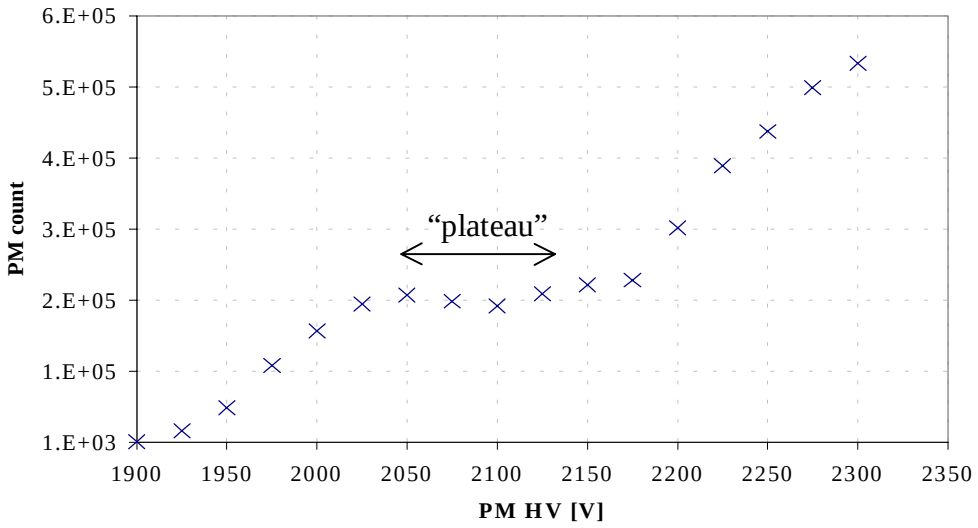

Figure 5.2 *Counter plateau measurement in the laboratory with a radioactive source of ^{137}Cs (3.5 MBq)*

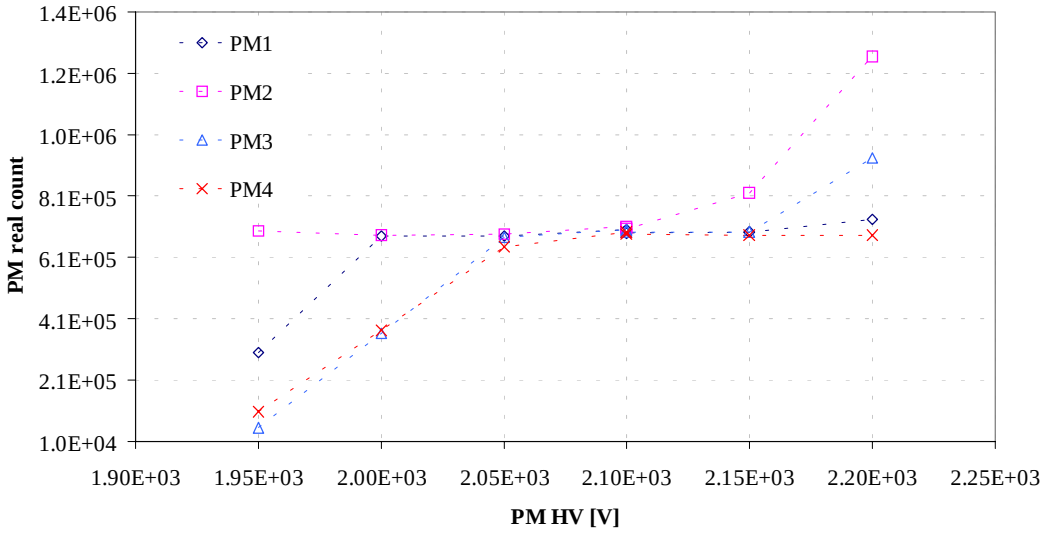

Figure 5.3 *Counter plateau measurement with beam. PM1, PM2 coupled to scintillators 10 mm thick. PM3, PM4 coupled to scintillators 1 mm thick.*

5.2 Coincidence setting

Each couple of counters is set in coincidence to reject the sources of physical or electronic background. The coincidences are adjusted with an oscilloscope using delay units which are afterwards replaced by delay cables with a 0.5 ns precision. The electronic coincidence width corresponds to the discriminator output signal width which was set to 10 ns.

5.3 Comparison between counters of different thickness

The performances of the pairs of “thick” and “thin” counters (10 mm and 1 mm, respectively) are presented as a function of the incident particles intensity and their range of linearity is verified. This measurement has been carried out at the SPS-H6 beam line with the PIC as reference detector (see § 4.1.2 and § 4.2). Figure 5.4 shows the experimental set-up. Intensity scans allow to test the linearity of each pair of counter by comparison with the PIC information. Figures 5.5 (a and b) show that below

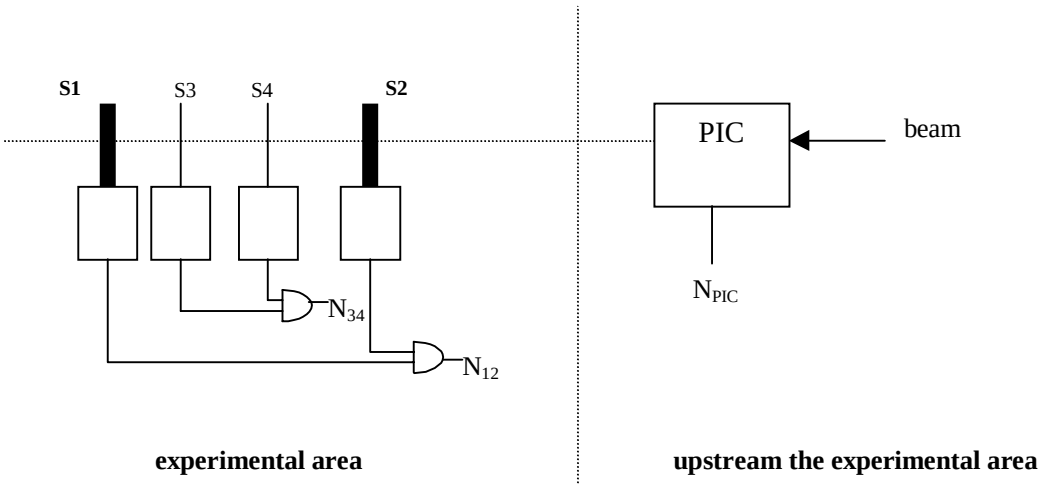

Figure 5.4 *Experimental set-up;* ***S1****,* ***S2****: 10 mm thick scintillators; S3, S4: 1 mm thick scintillators*

2 10^6 incident particles per second, both counters are linear and with similar responses. Between 2 10^6 and ~5 10^6 incident particles per second, both counters continue to rise with respect to the rate of incident particle but with different slopes. Between 3 10^6 and 4 10^6 incident particles per second the thick counters (1-2) saturate and their response drops because of the overlapping of the logic signals. The thin ones (3-4) cannot be used beyond 2 10^7 incident particles. Figure 5.5a presents the rough experimental data.

As already mentioned, the PS-T11 burst is 350 ms long and contains a maximum of 8 10^5 particles while in the SPS-H6, a maximum of ~10^8 particles are extracted during 2.5 s. This corresponds to an average rate of 2.3 10^6 particles per second and of 4 10^7 particles per second at the PS-T11 and the SPS-H6, respectively. The incident particles arrival follows a Poisson distribution. Suppose the SPS maximum intensity conditions i.e. 4 10^7 particles crossing the counter per unit time. The mean interval between each particle, Δt, is thus 25 ns. The probability, P(k), that k particles arrive in this interval Δt is

$$P(k) = \frac{\lambda^k}{k!} e^{-\lambda} \qquad (5.1)$$

with λ the mean number of particle that arrive during the interval time Δt (here λ=1). Some values are given in table 5.1.

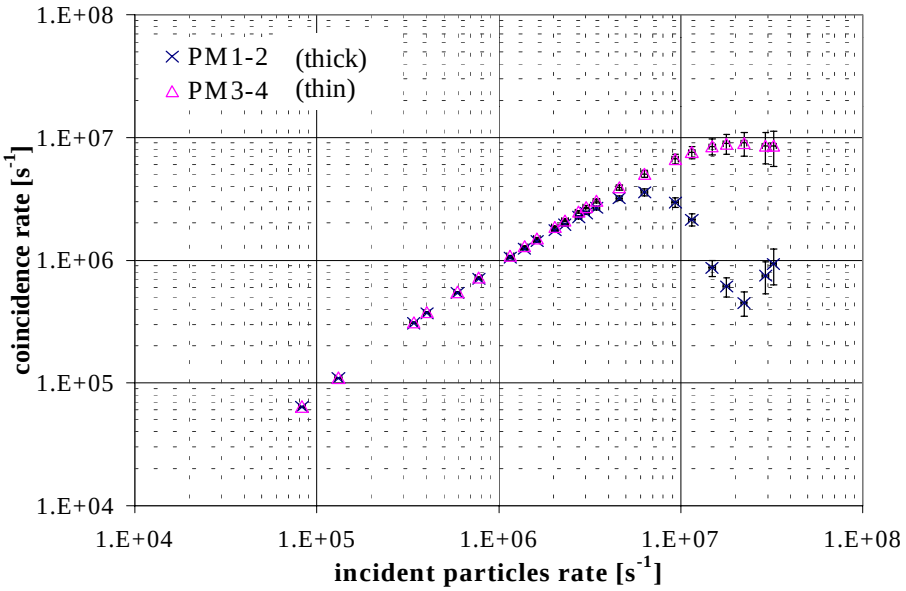

Figure 5.5a *Comparison between thin and thick reference detectors with PIC count as reference*

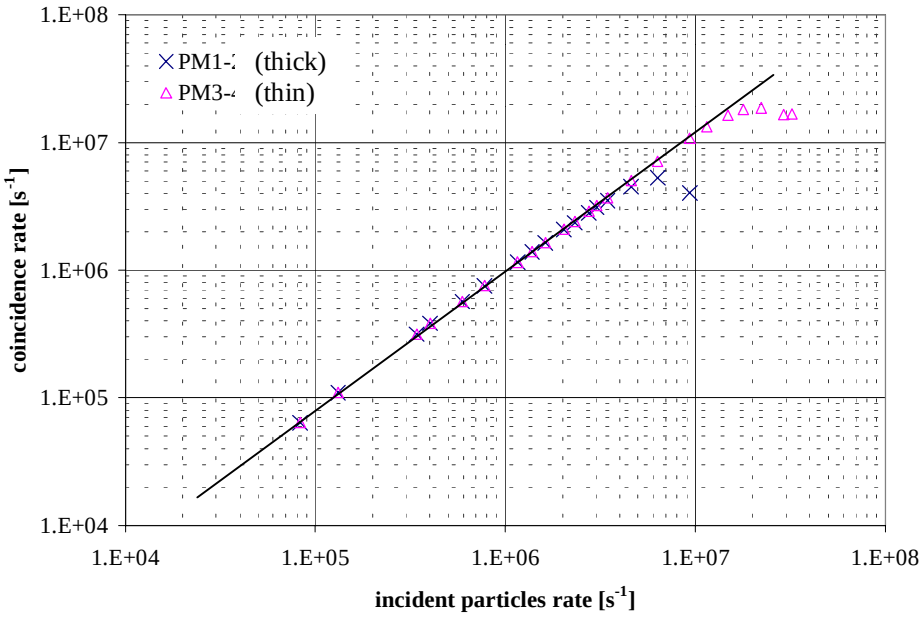

Figure 5.5.b *Comparison between thin and thick reference detectors with PIC count as reference after dead time correction (the line is to guide the eyes).*

Table 5.1 *Probability, P(k), that k particles cross the counter during an interval Δt defined as $\lambda = n\,\Delta t = 1$ with n the mean frequency of incident particles*

P(k=0)	0.368
P(k=1)	0.368
P(k=2)	0.184
P(k=3)	0.061
P(k=4)	0.015
P(k=5)	0.003

The cases with $P(k) \geq 1\%$ correspond to a maximum limit of 4 particles in 25 ns. We deduce that, at the SPS maximum rate, a non linearity beyond 1% is expected from the dead time unless $t_d \leq 5$ ns. In our case, the dead time of the counting has been estimated from a fit. It is of ~9 10^{-8} s for PM1-2 and of ~5.7 10^{-8} s for PM3-4. Figure 5.5b shows the curves corrected by these dead times. Below 10^6 incident particles per second the relative difference between the PM1-2 fit and actual responses is $\leq$ 9% while it is $\leq$ 6% for the PM3-4. We also remember that the systematic uncertainty on the PIC count is estimated to be 4% and that the response of this monitor is limited by the granularity of 2.2 10^4 particles/count [58]. The uncertainty on the PM count results from the residual non-linearity after the dead time correction and from the reading (the initial recorded counts were divided to allow a direct acquisition by the software unit). We take a value of 1% for the rate range of interest.

Chapter 6 Performances of the SEC monitor

In this chapter, a brief overlook introduces more details on Secondary Electron Emission (SEE). We then discuss the SEC optimal polarisation and the problem of noise. The monitor polarisation voltage is optimised before any experimental run. The linearity with rate is tested and the SEE yield is experimentally determined. Finally, some considerations about the SEC used as a LHC luminosity monitor are presented.

6.1 Secondary Electron Emission yield

A theory leading to the secondary electron emission from metal foils has been established for high speed incident ions with maximum energy of only a few MeV [50]. We have tentatively applied the above theory for incident protons with energy in the GeV range. The SEE is considered to be composed of two independent processes: the formation of the secondaries and their subsequent escape. Primary incident particles loss their energy through ionisation and excitation. It results the formation of secondary electrons inside the medium. Only a small fraction of these secondary electrons reach the surface with enough energy to escape from the solid. The number of such secondaries per incident particle, or **yield δ**, can be calculated as a function of primary particle energy and target characteristics. A fast ion losses its energy in distant and close collisions. In the distant ones, the ion produces only a small perturbation in the atoms of the material so that small amounts of energy are transferred in each collision. The close collisions result in large amounts of energy transferred to individual atomic electrons. The distant collision type accounts for the slow secondaries formed in a direct primary process whereas the close collision type gives rise to relatively rare energetic knock-on electrons (δ rays) which, in turn, produce secondaries in higher order collisions. For high ion velocities, the δ rays contribution is usually neglected. The motion of the secondaries is assumed to be a diffusive process. It leads to an exponential form in x/L_s for the

probability, P(x), that a secondary electron formed at a depth x below the surface is able to reach the surface and escape;

$$P(x) = TAe^{-\frac{x}{L_s}} \qquad (6.1)$$

where T and A are constants (TA~0.5) and L_s is of the order of the mean free path for the inelastic collisions.

The SEE yield, δ, is calculated knowing E_0, the mean energy loss per secondary formed (for solids E_0~25 eV), E_i, the energy of the incident particle, $\left(\frac{dE_i}{dx}\right)_{av}$, the mean energy loss of the incident particle per unit distance, M, the mass of the incident particle, m_0, the electronic mass and L_s, of the order of the mean free path for inelastic collision inside the foil (for Al L_s~2 10^{-7} cm).

$$\delta = \frac{1}{2\ E_0}\left(\frac{dE_i}{dx}\right)_{av} TA\ L_s\left(1+\frac{1}{1+\frac{E_{eq}}{100}}\right) \qquad \text{with} \quad E_{eq} = \frac{m_0}{M}E_i \qquad (6.2)$$

The above theory applied to incident protons with energy in the GeV range gives a yield δ ~1% for aluminium foil. This result is below the experimental values presented in table 6.1 from the reference [51]. We have determined experimentally δ for aluminium and found a value identical to the one in the table (new foil), as will be presented in section 6.4. For a luminosity of 10^{34} $cm^{-2}s^{-1}$ the calculation shows that, for the SEC in the LHC experimental conditions, the electrodes' SEE yield decreases of 1% after ~ 2 10^3 years. We conclude that, at the LHC, the SEE yield will remain constant.

Table 6.1 *The SEE yield, δ, per Al foil as a function of the total charge irradiation in protons/cm*^{2} [51]

total irradiation [p.cm^{-2}]	foil yield [%]
0 (new foil)	6.8
10^{18}	6.5
10^{20}	4.0

6.2 SEC polarisation

In a SEC, the polarisation voltage applied between two consecutive electrodes determines the collection efficiency of the secondary electrons. An optimum voltage must be chosen to allow a complete collection. The polarisation voltage necessary to collect all the emitted secondary electrons is obtained experimentally by a "plateau" measurement. An estimate of the optimal polarisation value could be done considering the energy distribution (or spectrum) of the secondary electrons emitted from the aluminium electrodes. Previous measurements show that the secondary electrons are mostly emitted from metal surfaces with an energy, ε, around 2-4 eV[62]. Charged particles crossing a non polarised SEC induce SEE from each electrode surface. They create two currents in opposite directions between the consecutive electrodes. These currents compensate each other and no signal appears at the SEC output. When a polarisation voltage is applied, the electric field between the consecutive electrodes tends to annihilate the current emerging from the high potential electrodes. The polarisation voltage must be such that the potential energy compensates the initial kinetic energy, ε, of the secondary electrons so that they cannot leave the surface of the positive potential electrodes. Then, only secondary electrons emerging from the negative potential electrodes are collected. The applied polarisation voltage must be larger than ε. However the polarisation must be high enough to avoid any effect from the creation of space charge between consecutive electrodes. For a polarisation of ~5 Volt (the minimum polarisation voltage used during our tests) and for an aluminium foil yield of ~7% [51], a total collection and no saturation

effects are expected at the PS and the SPS maximum intensity conditions (see appendix H).
A constant SEE current ("plateau") has been found during our measurements for polarisation voltages between 5 V and 20 V which confirms the previous prediction of a complete collection of the secondary electrons for a polarisation close to ε.

6.3 Sources of noise

The SEC response could be limited by leakage currents and by several sources of electronic noise related to the experimental conditions. We give hereafter the results of their measurement and we describe our attempts to minimise them.

6.3.1 SEC leakage current

The SEC sensitivity is limited by the input bias current of about 100 fA of the operational amplifier in the IVC102 and by the monitor leakage current, I_{leak}. The resistivity between electrodes induces the leakage current, I_{leak}, which adds to the SEC output current. A resistivity of 10^{14} Ω has been measured between the signal and the polarisation electrodes of our first monitor prototype. For a polarisation voltage of 10V, this leads to a leakage current $I_{leak}=10^{-13}$ A. This value is of the same order of the input bias current of the IVC102. In the second prototype, the resistivity has been increased by removing the ceramic spacers used in the previous version for insulation between electrodes (see § 3.3). The insulation is thus ensured by vacuum instead of ceramic and the resistivity of the second prototype is above 10^{15} Ω, the highest value that can be read with our measuring device. The amplifier bias current constitutes the main limitation for the response of the second prototype.

6.3.2 Electronic noise

The electronic noise can be estimated from the width of the "pedestal" i.e. the monitor response in the absence of signal, integrated over a specific interval of time. A periodic contribution to the pedestal width could come from a "ripple" of the power supply for instance. Moreover, the high impedance of the electronics makes it very sensitive to the surrounding electromagnetic disturbances as the measuring system is "floating" and non differential. In the low frequency range, a drift can be due to "day-night" temperature variations for instance.

Before continuing we should recall the sequence of data acquisition in the present system (see chapter 4 figure 4.7 and figure 6.1). During a machine cycle, a first measurement of charges is done by the integration of the SEC current over a period of time, Δ_I which covers the spill (or extraction pulse) while a second one, with same duration, is taken "off spill". The monitor response is estimated as the difference of the two sets of data. The signal "off spill" corresponds to the "pedestal" and can be considered to result from the superposition of a constant offset and a fluctuation (or noise). In order to understand the noise we have analysed the "off spill" data in detail. Two behaviours have been considered. First, a white noise with a standard deviation σ. Second, a periodic signal with a frequency $\nu<1/\Delta_I$ and with an amplitude which corresponds to a standard deviation σ_0. For the first hypothesis, the offset can be estimated as the average value "off spill" because the long integration time averages out the fluctuations. The standard deviation $\tilde{\sigma}$ gives the residual noise. For the second hypothesis, we have attempted a power spectrum estimation by the Maximum Entropy Method (MEM) [91] .MEM has the very cute property of being able to fit sharp spectral features. An example of such analysis is presented hereafter.

Two pathological sets of data are discussed for illustration (see figures 6.2 and 6.3) while the general conclusion is reported later. A formal expression for representing 'true' power spectra (up to normalisation) is

$$P(f) = \left| \sum_{k=-\infty}^{\infty} c_k z^k \right|^2 \quad \text{with } z = e^{2\pi i f \Delta} \qquad (6.3)$$

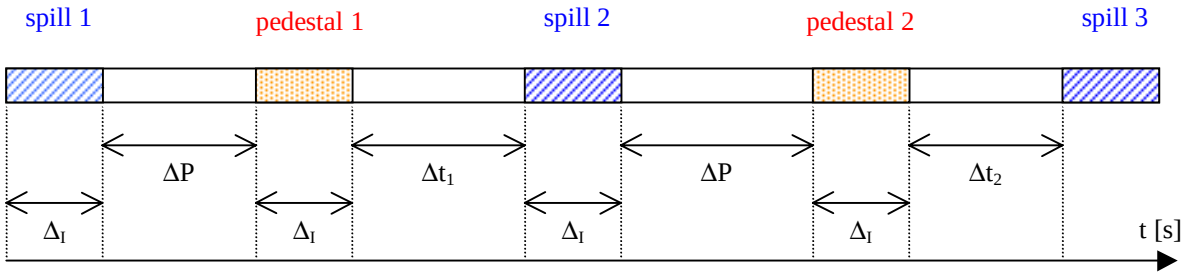

Figure 6.1 *Time repartition of successive data acquisitions in and off spill (Δ_I is the acquisition duration corresponding to the spill and to the pedestal, ΔP is the duration between the spill and the first following pedestal and Δt is the duration between a pedestal and the next spill.*

where Δ is the sampling interval in the time domain. This is an infinite Laurent series wich depends on an infinite number of values c_k. It turns out that there are some advantages in an approximation of P(f) whose free parameters all lie in the denominator, namely,

$$P(f) \cong \frac{a_0}{\left|1 + \sum_{k=1}^{M} d_k z^k\right|^2} \qquad (6.4)$$

which brings in a new set of coefficients d_k's. Equation 6.4 has poles corresponding to infinite power spectral density, on the unit z-circle. Such poles provide an accurate representation of the underlying power spectra that have sharp, discrete 'lines' or delta-functions. This approximation (equation 6.4) is called the 'Maximum Entropy Method' (MEM).

Figures 6.2 and 6.3 present data "off spill" recorded the same day, in a time interval of 30 minutes, at the SPS-H6 beam line. The power spectral density corresponding to the data of figure 6.2 is presented in figure 6.4. In this example, the total acquisition time is 432 s (ω_0=0.015 s^{-1}). Three frequencies are emerging: f_1= 0.0064 s^{-1}, f_2=0.0134 s^{-1} and f_3=0.0201 s^{-1}. However the dominant one is f_1. The corresponding period is T_1=157s.

Indeed, figure 6.2 exhibits a clear periodicity of 2 – 3 minutes which corresponds to T_1. It was explained by some electric disturbances from the magnets surrounding the experimental area. Three frequencies also emerge from the spectral analysis presented in figure 6.5 (from the data of figure 6.3): f_a=0.0079 s^{-1}, f_b=0.0153 s^{-1} and f_c=0.0274 s^{-1}. The dominant frequency is f_a with corresponding period T_a=126 s which could be explained as previously by some electric disturbances from the surrounding magnets. Random signals generated around the recorded signal allows to make sure about the significance of the values found for the emerging frequencies.

This analysis has been performed for several sets of data taken from different runs at the PS and at the SPS. No periodicity has been observed in most of the data. Runs with pathological behaviour have been discarded.

We have attempted to determine the quality of the data after the pedestal subtraction. The pedestal determined "off spill" corrects efficiently for slow drifts of the baseline. However, the subtraction adds a new noise contribution. The total fluctuation after subtraction can be measured from the histogram of the SEC data obtained without beam (beam off). Figure 6.6 presents such an histogram for a set of data taken at the PS. When considering the raw counts, the rms is 146. It decreases to 76 when subtracting the pedestal values to the raw counts. Thus, in this example the pedestal subtraction leads to a better estimation of the data.

A rough estimate has also been done for some runs by the comparison of successive pedestal values (see figure 6.1). For example, we report here the results obtained from an analysis of data taken at the SPS. During this run the mean value of the pedestal values is 7500 raw counts while the standard deviation is σ= 139 raw counts. First we consider the difference between two consecutive pedestal values, ~15 s apart. Their standard deviation is σ_{p1-p2} =187 raw counts. For the same run, we skip one SPS cycle and consider pedestal values ~30 s apart. In this case σ_{p1-p3}= 219 raw counts. Assuming a linear behaviour in time, we estimate at σ= 163 raw counts the fluctuation at 4 s which is, at the SPS, the value of ΔP, the delay between the spill and the pedestal acquisition time. We can also infer the intrinsic noise of each measurement to be $\sigma/\sqrt{2} \approx 163/\sqrt{2}$

These studies have been done for different set of data. In general, the electromagnetic noise has been kept under control and the pathological cases have been discarded.

In conclusion, the pedestal to be subtracted from each “in spill” measurement was estimated from the next “off spill” value.

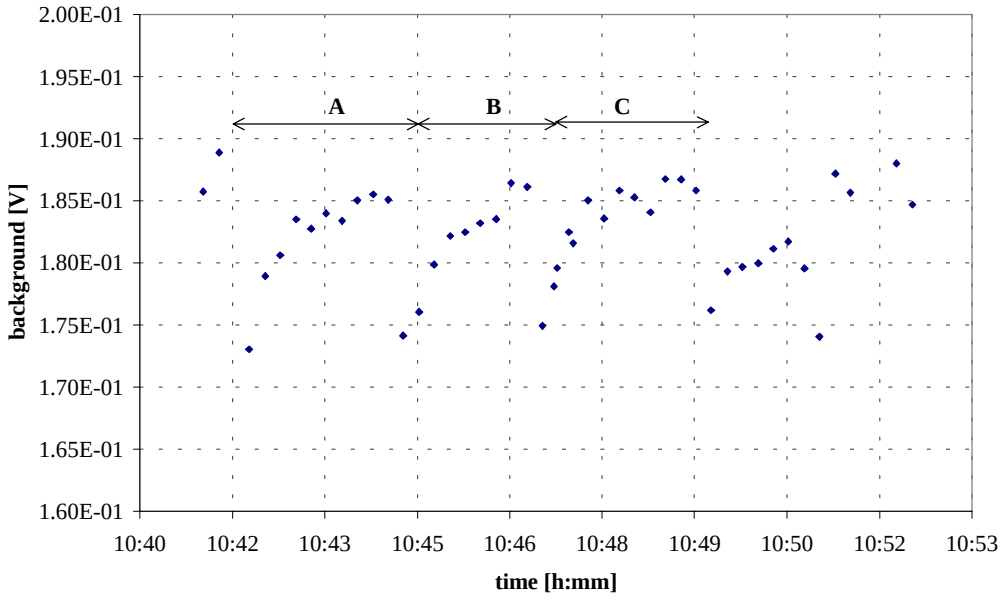

Figure 6.2 *Evolution of the pedestal (example 1)*

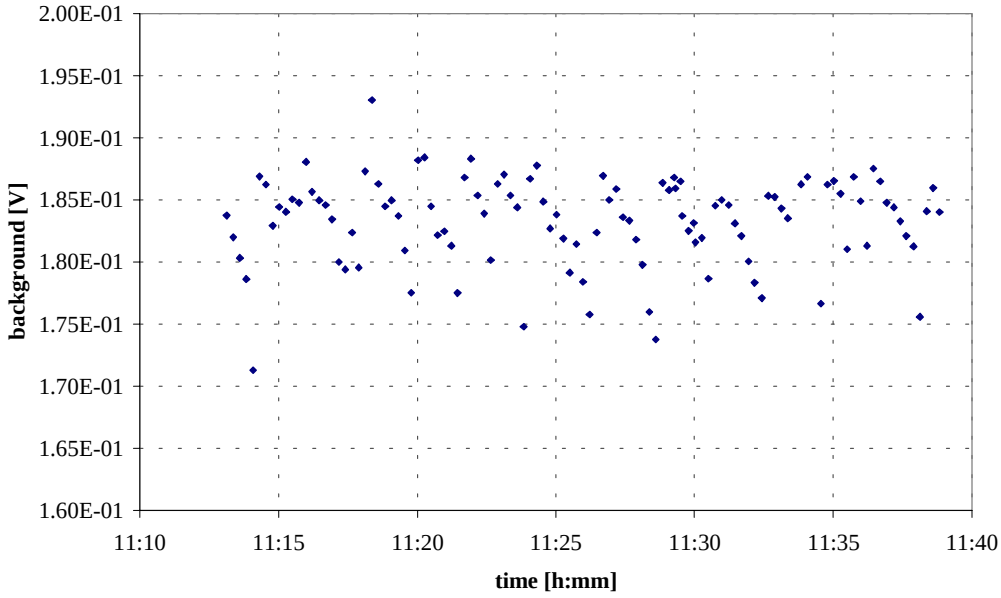

Figure 6.3 *Evolution of the pedestal (example 2)*

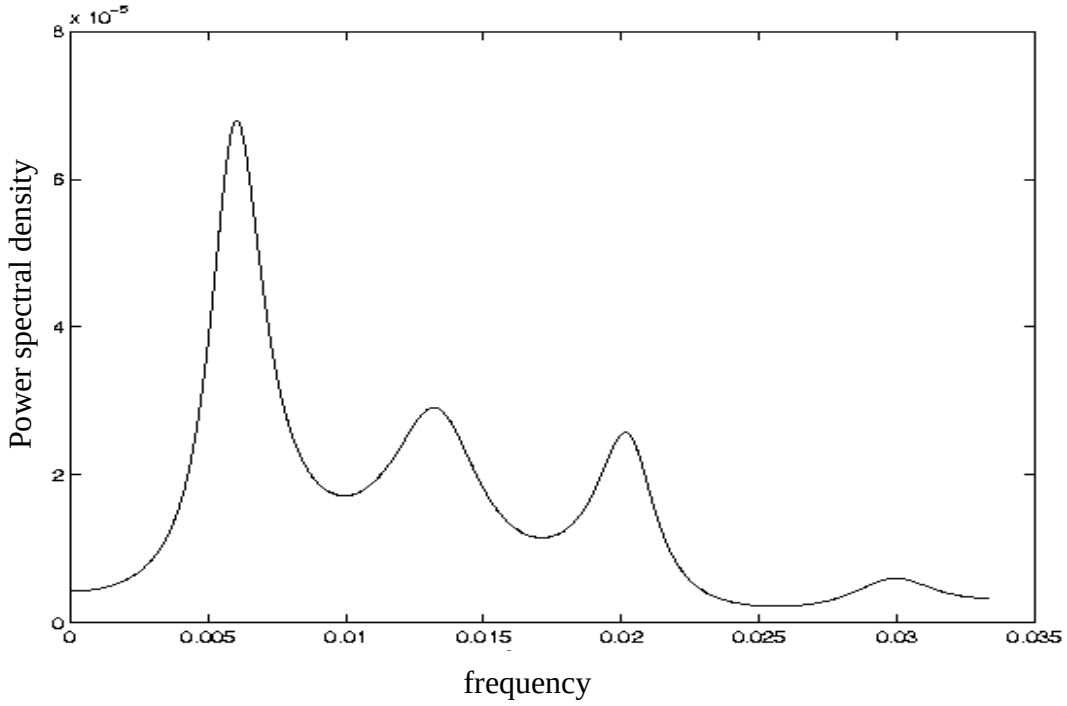

Figure 6.4 *Power spectral density corresponding to figure 6.2 (example 1)*

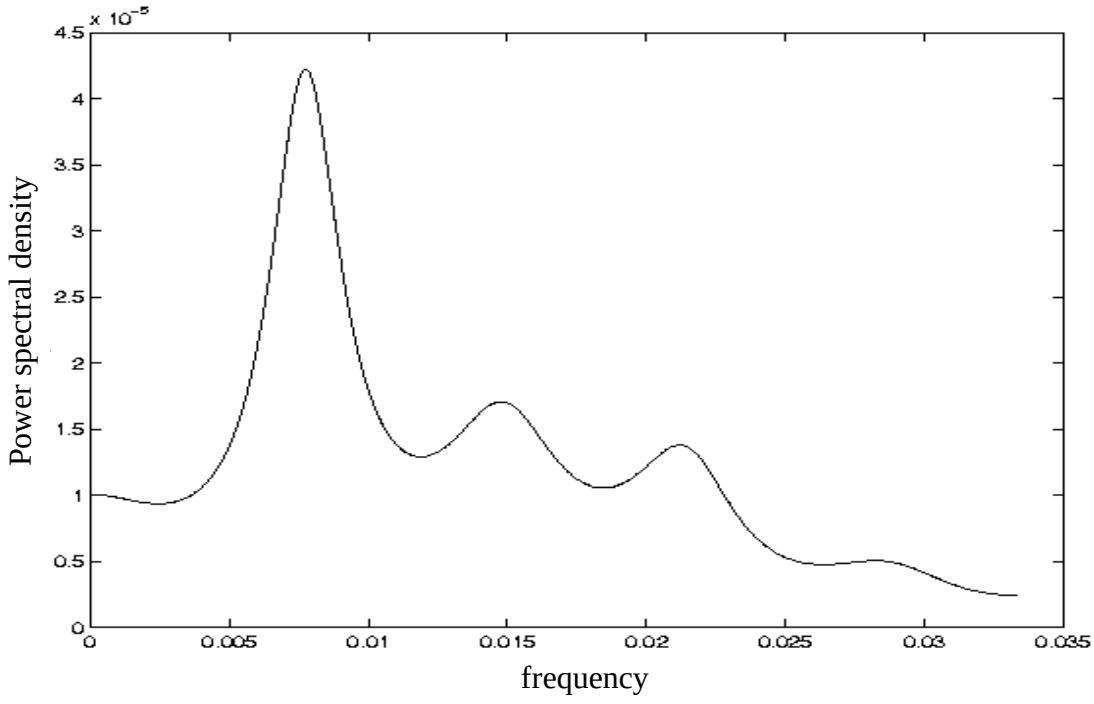

Figure 6.5 *Power spectral density corresponding to figure 6.3 (example 2)*

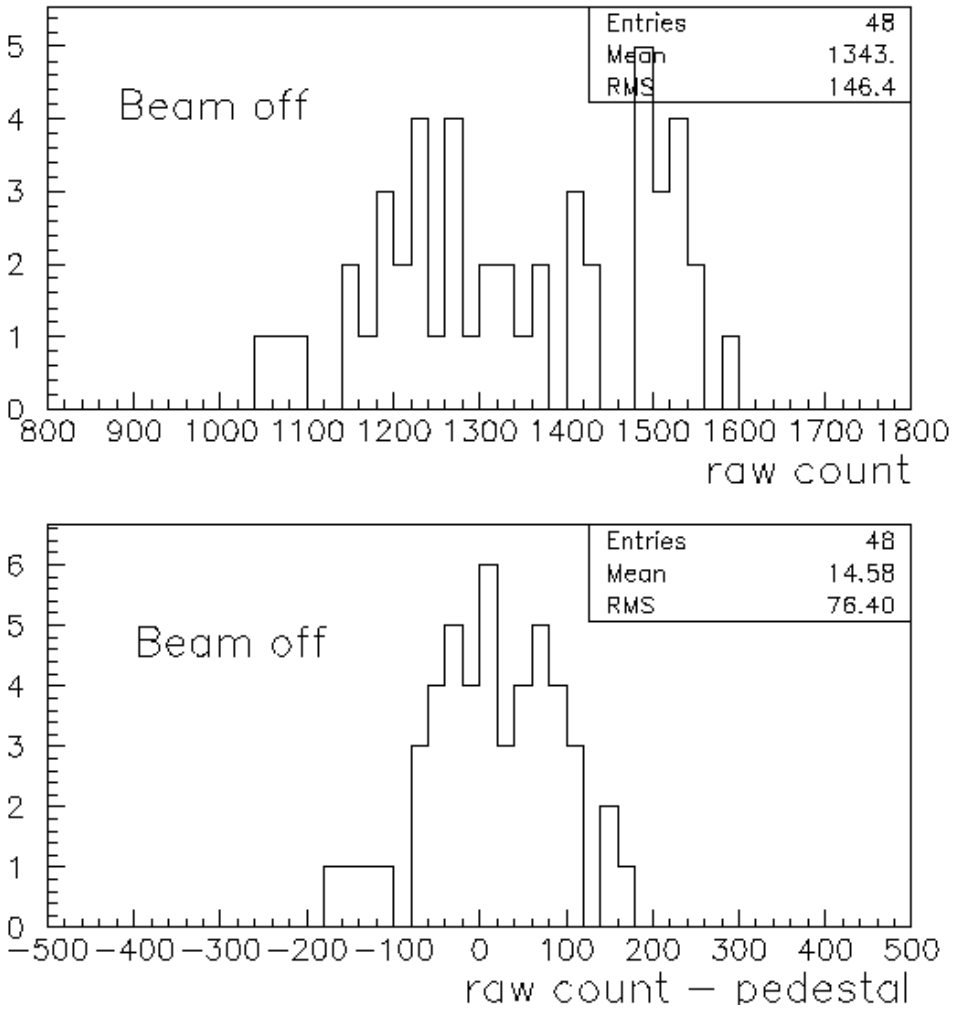

Figure 6.6 *Histogram of the SEC data obtained without beam (beam off) at the PS. The top figure corresponds to the raw counts while the pedestal has been subtracted in the bottom figure.*

6.4 Performances of the SEC

These tests were carried out at CERN on the PS-T11 and SPS-H6 beam lines by comparison to scintillation counters (SC) and to PIC (see chapter 4) with intensities ranging from 5 10^5 particles per burst to 6 10^7 particles per burst. The linearity tests of the SEC and its SEE yield determination are presented.

6.4.1 SEC linearity test and calibration

Before presenting the linearity and calibration of the SEC we want to discuss the systematic effects. Two categories of systematic errors need to be considered for our tests: the normalisation error from the reference counter and the SEC measurement uncertainty due to electronics.

As already mentioned, in the experimental set-up, two kinds of reference detectors have been used: a scintillation counter (SC) and a Precision Ionisation Chamber (PIC). In the dynamic range under consideration at the PS (maximum of 8 10^5 incident particles per burst), the SC count uncertainty is 1% from non linearity over the full range. For tests carried out at the SPS, the reference detector is always the PIC whose error is reported to be ~ 4% [58]. We assume that also in this case the non linearity measurement is 1%.

The SEC systematic uncertainty related to the electronics is bounded to be lower than 1% (deduced from the electronics components characteristics). An additional systematic uncertainty of 5% comes from the capacitance of the IVC102. It does not affect the linearity of the system and has no impact on the relative comparison between SEC measurements. As will be discussed later, a SEC measurement is obtained as the average over several following bursts.

Figures 6.7a and 6.7b report the linearity tests of the SEC prototype. The monitor signal in volt is given as a function of the number of incident particles per burst measured by the reference detector. Each point corresponds, in general, to the average over more than 50 measurements (see table 6.2). Each measurement corresponds to the integral over one spill.

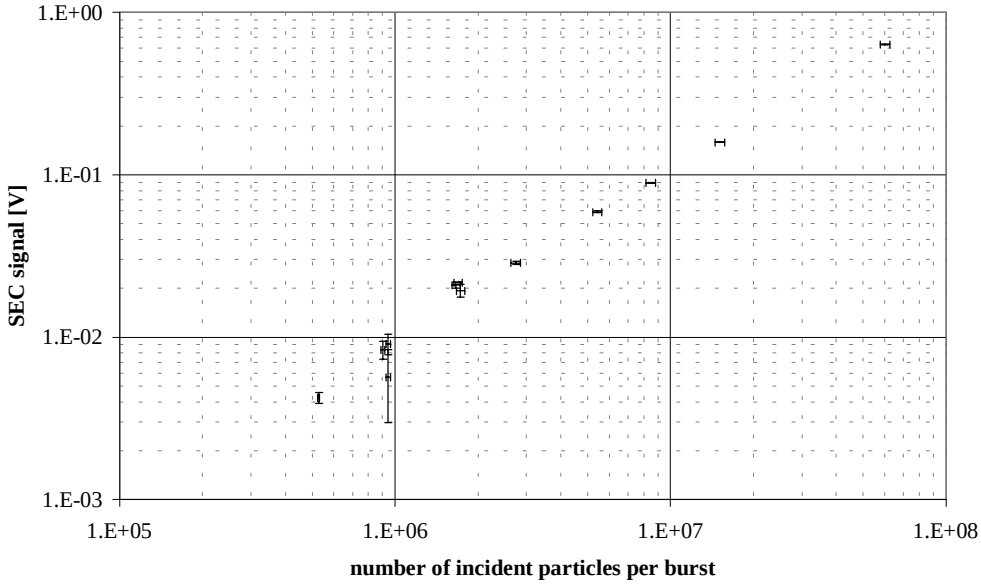

Figure 6.7a *SEC signal versus the number of incident particles per burst*

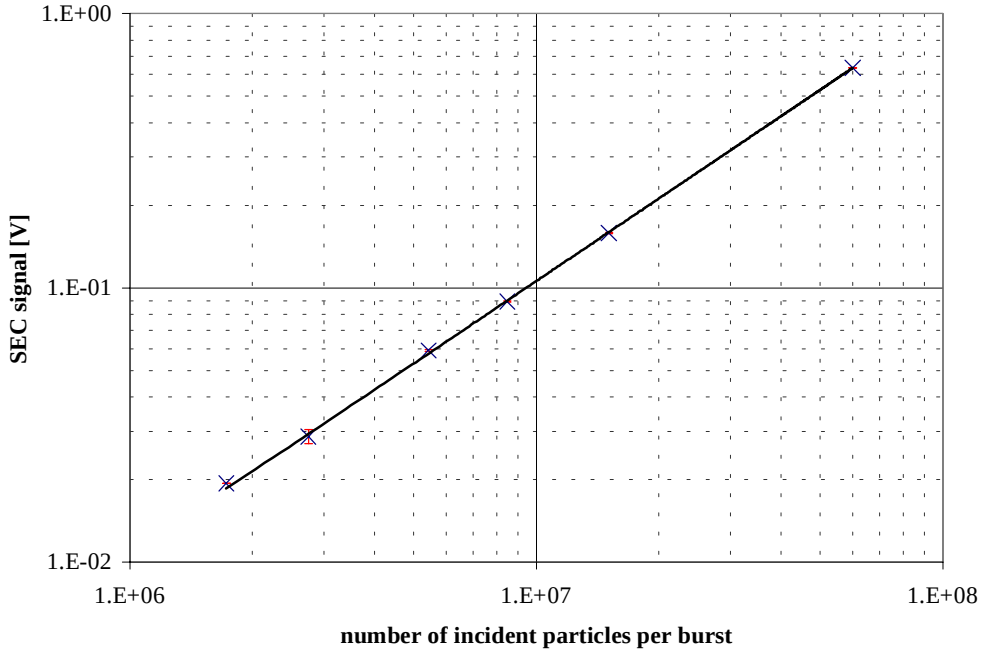

Figure 6.7b *SEC signal versus the number of incident particles per burst (zoom at high intensity)*

Table 6.2 *Study of the SEC linearity. The 2nd column gives the average number of incident particles per burst as measured by the scintillator counters or the PIC. The 3rd and 4th columns give the incident current and the SEC response. The 5th column reports the r.m.s. over a number of measurements N (6th column). The statistical precision on the average estimate is the 7th column. The last column combines statistical and systematic precision (in quadrature).*

Reference monitor	Average number of incident particle per burst ± (absolute error + digits error)	Incident particles current [A]	SEC response [mV]	σ_{SEC} [mV]	Number of measures, N	$\sigma_{SEC} \times N^{-0.5}$ [%]	σ_{tot} [%]
SC	528800 ± (1+0) %	$1.7\ 10^{-13}$	4.2	9	731	7.8	8
SC	903000 ± (1+0) %	$2.9\ 10^{-13}$	8.3	10.7	106	12.5	12.5
SC	944400 ± (1+0) %	$3\ 10^{-13}$	9	8.9	46	14.5	14.5
SC	$1.67\ 10^{6}$ ± (1+0) %	$5.3\ 10^{-13}$	20.9	8.5	115	3.8	3.9
PIC	$2.75\ 10^{6}$ ± (4+0.8) %	$1.8\ 10^{-13}$	28.7	5.3	60	2.4	2.6
PIC	$5.43\ 10^{6}$ ± (4+0.4) %	$3.5\ 10^{-13}$	59.1	4.4	40	1.2	1.5
PIC	$8.49\ 10^{6}$ ± (4+0.23) %	$5.4\ 10^{-13}$	89.2	5.5	64	0.8	1.3
PIC	$1.5\ 10^{7}$ ± (4+0.14) %	10^{-12}	158.5	3.1	51	0.3	1
PIC	$6\ 10^{7}$ ± (4+0) %	$3.8\ 10^{-12}$	634.3	4	44	0.1	1

Below ~ 1.7 10^6 incident particles per burst, the monitor response has some fluctuations. The linearity is well determined above 1.7 10^6 incident particles per burst. The TOTEM collaboration expects to give to CMS the luminosity with an uncertainty of ~ 2%. From table 6.2 we see that an uncertainty of ~ 3% is achieved above ~ 3 10^6 incident particles per burst. The fluctuations at low intensity are mainly due to the noise of the electronics. If, in the future, better operational amplifiers will be available, the SEC lower detection threshold corresponding to a precision of ~ 3% might be shifted below 3 10^6 incident particles. In such a situation, the influence of the contribution of the leakage current in the SEC response should be reconsidered.
In the hypothesis of the use of the monitor for calibration in the SPS environment the figure 6.7b gives a zoom over 10^6 incident particles per burst. From the error on the slope of the linear regression we obtain a contribution to the calibration precision of ~0.2%. The calibration could be expressed as

$$N=9.5\ 10^7\ V \pm 0.2\%$$

with N the number of incident particles per burst and V the SEC signal in volts.

6.4.2 SEC yield

The SEC yield, δ, is determined experimentally as the ratio between the number of emitted secondary electrons, N_e, and the number of incident particles on the monitor, N_p,

$$\delta = \frac{N_e}{N_p} \qquad (6.5)$$

The number of secondary electrons is estimated from the count, N_{count}, given at the output of the electronic measuring system which can be transformed into a charges number. We obtain with the same precision as before

$$N_e = \frac{VC_{int}}{1.6 \cdot 10^{-19}} \qquad (6.6)$$

where V is the SEC response [V] and C_{int} is the IVC102 capacitance [F]. The sources of error on N_e are the electronic noise and the statistics while for N_p it is related to the reference detector (PIC or scintillation counter) as discussed above.

δ has been calculated only for the acquisition runs with a number of incident particles above 3 10^6 which insures ~ 3% of uncertainty on the SEC response. The results are presented in table 6.3. The SEC yield is estimated to be (66 ± 3) %. As the SEC is made of 10 emitting aluminium foils, the secondary electrons emission yield per foil is $1/10$ of this value i.e. (6.6 ± 0.3) %. This result agrees with the previous measurements carried out by Ferioli and Jung (see table 6.1) for almost new aluminium foils [51].

Table 6.3 *The SEC yield estimation*

Number of incident particle per burst, N_p	SEC yield, δ [%]
6.10^7	66±3.3
15.10^6	65.6±3.3
8.10^6	65±4
5.10^6	68±3.3

6.5 The SEC as a LHC luminosity monitor

According to our estimates (see appendix D), LHC luminosities of 10^{34} $cm^{-2}s^{-1}$ and 10^{28} $cm^{-2}s^{-1}$ correspond, respectively, to incident particles currents of 1.3 10^{-9} A and 1.3 10^{-15} A. We can calculate the acquisition time necessary to achieve ~3% precision from the SEC as function of the LHC luminosity. Just scaling the results of table 6.2, we obtain an integration duration below 1 ms for $L=10^{34}$ $cm^{-2}s^{-1}$ and about 6 minutes at $L\sim10^{28}$ $cm^{-2}s^{-1}$. We achieve a precision of ~ 3% within 1 s for $L\sim10^{31}$ $cm^{-2}s^{-1}$. These results assure in particular that the long term drift is well kept under control by the method of the pedestal subtraction previously described. As LHC luminosity monitor the SEC will be used above $L \sim 10^{31}$ $cm^{-2}s^{-1}$.

Chapter 7 The ionisation chamber mode

A conversion of the detector into an Ionisation Chamber (IC) is proposed to cover the LHC low luminosity region. We transform the SEC into IC by filling the chamber with Ar at 1 atm. The IC has a gain of the order of 10^3 and should allow to measure luminosities down to 10^{28} $cm^{-2}s^{-1}$. After a judicious choice of the polarisation voltage, some parameters and the recombination rate are calculated. The monitor performances, particularly its linearity versus the number of incident particles, its gain and noise determination are presented. The transition from SEC to IC mode is also discussed.

7.1 Optimal polarisation of the IC

Incident charged particles ionise the gas of the IC and produce a number of ion-electron pairs proportional to their path length in the gas. The electrons and positive ions move, under the influence of the applied electric field, toward the anode and the cathode where they are collected, respectively. The electric field, E, must be large enough to avoid any loss of signal due to the recombination of the created charges before they reach the collecting plates. The recombination effects can be overcome by applying a large enough voltage $V>V_{min}$. A quasi complete collection of the ions and electrons produced by ionisation in argon at atmospheric pressure is obtained for [65] (see appendix I)

$$V_{min} = \frac{d^2}{2}\sqrt{\frac{J}{\varepsilon_0 k^+}} \qquad (7.1)$$

with d the inter-electrodes distance [m], J the current density [Am^{-3}], k^+ the positive ions mobility [$m^2V^{-1}s^{-1}atm$] and ε_0, the vacuum permitivity [$AsV^{-1}m^{-1}$] (see appendix I). The expression of the current density, J, is

$$J = e\phi G \qquad (7.2)$$

with e the electronic charge [C], ϕ the flux of incident particle on the IC [$m^{-2}s^{-1}$] and G the IC gain [m^{-1}] defined as the number of ion-electron pairs created per crossing particle. J is calculated for the experimental conditions corresponding to the plateau curves 7.1a and 7.1b i.e for 10^7 particles per SPS burst and 5.2 10^5 particles per PS burst. With G ~ 10^4 [m^{-1}] [63], we obtain values of 2 10^{-5} [Am^{-3}] for J_{SPS} and of 7.6 10^{-6} [Am^{-3}] for J_{PS}. Equations 7.2 and 7.3 predict minimal potential values of 2.6 V at the SPS and 1.5 V at the PS. The "plateau" measurement should confirm this prediction.

Figures 7.1a and 7.1b show the monitor response as a function of the polarisation voltage for the IC installed in the SPS and the PS beam lines, respectively. Each point is an average value over the number N of measurement. The standard deviation divided by $\sqrt{N}$ is used as the statistical uncertainty. The difference between the plateau values of figures 7.1a and 7.1b (i.e. ~ 1.3 V and ~ 0.4 V, respectively) could in principle be related to the difference between the numbers of incident particles used to perform the tests at the PS and the SPS (a difference of about a factor 3). For the SPS, the signal is almost constant above a potential of 2.5V. For the PS, the plateau was reached for a potential between 1V and 2V.

This confirms the previous predictions for the complete collection inside the IC. The polarisation voltage between consecutive electrodes was subsequently set always above 5V.

We now want to estimate the residual recombination rate in the plateau region. The recombination rate, ξ, per unit time and per unit volume is defined as [38]

$$\xi = \frac{dn}{dV_{ol}dt} = \alpha_r N^+ N^- \qquad (7.3)$$

with n, the number of recombination, V_{ol} the inter-electrode volume [m^{-3}], α_r the recombination coefficient [$m^{-3}s^{-1}$] (α_r=3 10^{-7} for Ar). $N^{-/+}$, the electrons and positive ions densities [m^{-3}], can be calculated from the flux of incident particles, the IC gain, G, and

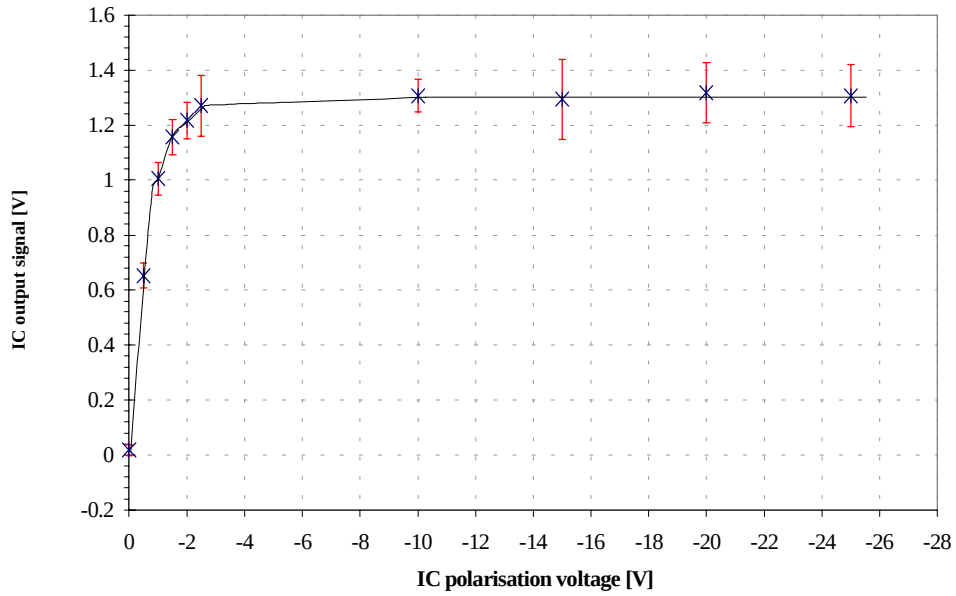

Figure 7.1a *Plateau curve for the IC at the SPS (the line shown is to guide the eyes)*

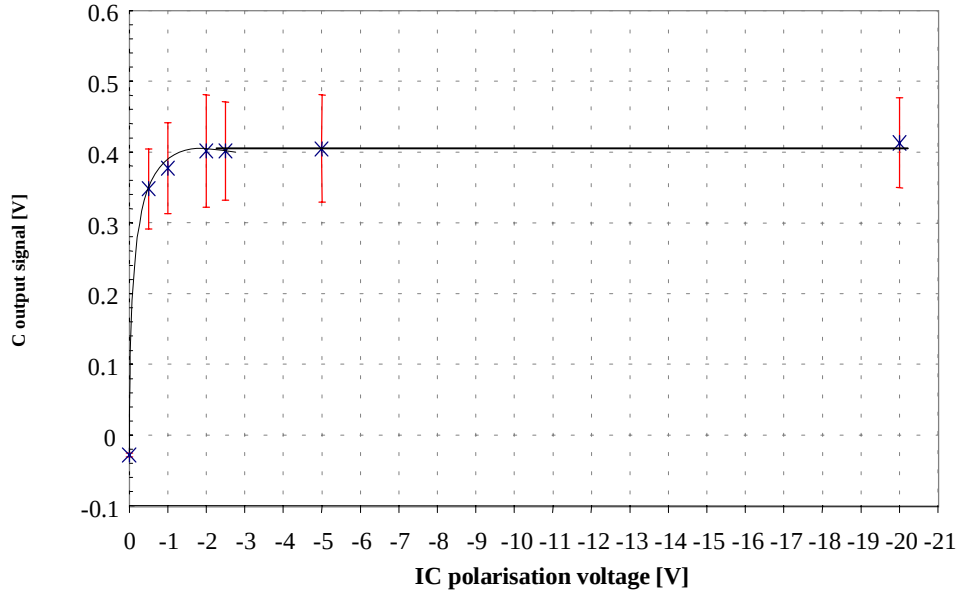

Figure 7.1b *Plateau curve for the IC at the PS (the line shown is to guide the eyes)*

the drift velocity, $v^{-/+}$, of electrons and positive ions for the IC polarisation voltage of interest, V.

$$N^{+} = \frac{NG}{S_{beam} T_{burst}} \frac{d}{v^{+}} \quad \text{and} \quad N^{-} = \frac{NG}{S_{beam} T_{burst}} \frac{d}{v^{-}} \tag{7.4}$$

with N the number of incident particles per burst, S_{beam} the beam surface [m^{-2}], T_{burst} the extraction time [s], d the distance between two consecutive electrodes [m]. For polarisation voltage lower than 25 Volts, the electrons velocity, v^{-}, is estimated three hundred times larger than the velocity of the positive ions and can be expressed at atmospheric pressure as

$$v^{-} \cong 300 v^{+} \quad \text{with} \quad v^{+} \cong \frac{k^{+} V}{d}, \tag{7.5}$$

with k^{+}, the positive ions mobility [$m^2 s^{-1} V^{-1}$] (in Ar, $k^{+}=1.7\ 10^{-4}$). Above 25 Volts, v^{-} has been deduced from the graphs of the reference [38]. The table 7.1 reports values of N^{+} and N^{-} for different polarisation voltages when 10^3 particles are incident on the IC per unit time. We introduce now the relative recombination rate, r,

$$r = \frac{1}{N} V_{ol}\ T_{burst}\ \xi \tag{7.6}$$

with N the number of incident particles per burst. The figure 7.2 shows r as a function of the number of incident particles per second, N/T_{burst} . As expected, it increases linearly with the number of incident particles and is inversely proportional to the polarisation voltage. The recombination rate corresponding to the PS maximum intensity (i.e. $8\ 10^5$ particles per burst or $1.6\ 10^6$ particles per second) is always lower than 1%. In the worst case, i.e. with the highest intensity achieved at the SPS of $6.22\ 10^7$ particles per burst (i.e. $\sim 2\ 10^7$ particles per second) a maximal relative recombination rate of ~ 3% is obtained for a polarisation voltage of 5 V. In conclusion, the recombination effect is considered negligeable for all the data presented.

Table 7.1 *N^+ and N^-, the positive ions and electrons densities, in the PS and the SPS for a rate of 10^3 incident particles per second as a function of the polarisation voltage.*

	Polarisation voltage [V]	N^+ [m^{-3}]	N^- [m^{-3}]
PS	-5	$2.7\ 10^9$	$9\ 10^6$
	-10	$1.3\ 10^9$	$4.5\ 10^6$
	-50	$2.7\ 10^8$	$2.3\ 10^5$
	-150	$9\ 10^7$	$1.2\ 10^5$
	-250	$5.4\ 10^7$	$9.8\ 10^4$
SPS	-5	$3.8\ 10^8$	$1.2\ 10^6$
	-10	$1.9\ 10^8$	$6.3\ 10^5$
	-50	$3.8\ 10^7$	$3.2\ 10^4$
	-150	$1.2\ 10^7$	$1.7\ 10^4$
	-250	$7.6\ 10^6$	$1.3\ 10^4$

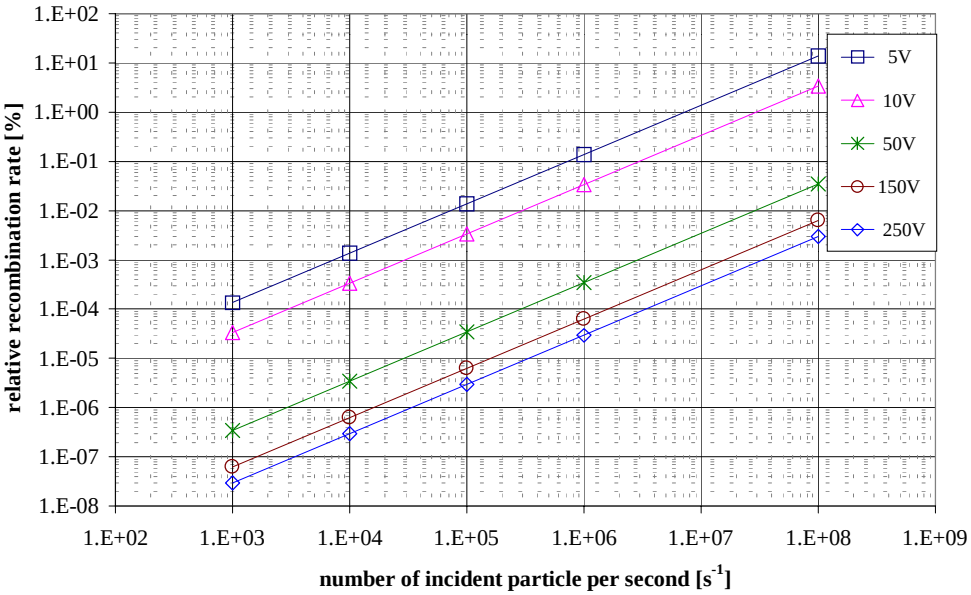

Figure 7.2. *Relative recombination rate inside the IC*

Neglecting the recombination and the contribution of the electrons we obtain[65,66] for the maximum intensity used during our tests i.e. ~ 6 10^7 incident particles/ SPS burst

$$\frac{\delta E}{E_0} \cong \frac{1}{2E_0^2}\frac{Jd^2}{\varepsilon_0 k_+} \leq 10\% \text{ at 15 V} \qquad (7.7)$$

with $\delta E=E-E_0$ the electric field due to space charge, E_0 the initial electric field at the cathode [Vm^{-1}], J the density of charges produced per unit time and per unit volume ($J\sim10^{-4}$ [$Cs^{-1}m^{-3}$]), ε_0 the space permitivity [$AsV^{-1}m^{-1}$], k_+ the positive ions mobility ($k_+=1.7\ 10^{-4}$ [$m^2V^{-1}s^{-1}$atm]). This correction will shift our estimates by a small amount when the voltage is above 15 V.

7.2 Performances of the IC

As in the case of the SEC mode, the monitor signal is pedestal corrected by the subtraction of the "off spill" values. The electronic noise is the same that for the SEC case.

Figure 7.3 shows the IC response versus the number of incident particles per SPS burst. The IC values have a statistical uncertainty lower than 2%. The linearity over the full experimental range (3 decades) is within 0.1 %. With an appropriate polarisation voltage, at the SPS intensities, no physical process seems to alter the linearity of the IC. In this case the calibration of the monitor gives

$$N=5.1\ 10^7\ V \pm 0.1\ \%$$

with N the number of incident particles per burst and V the IC signal in volts. The linear regression gives an error of ~0.1% to which we have to add the systematic on the reference detector (4% for the PIC and 1% for the SC counter).

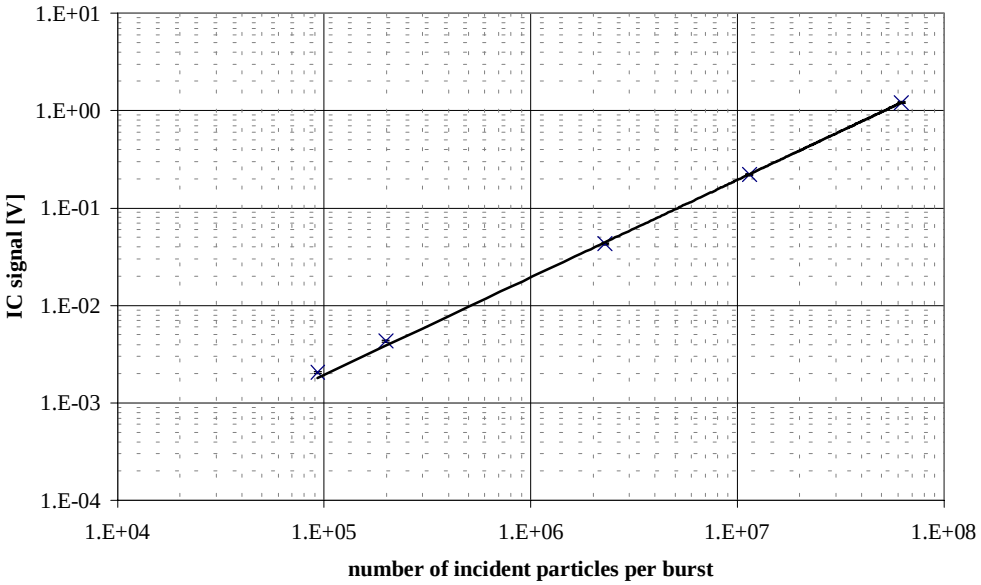

Figure 7.3 *Signal of the IC versus the number of incident particles per burst*

The gain, G, of the IC is the number of ion-electron pairs created per particle crossing the detector. This depends on the nature and pressure of the inner gas detector. Prediction using the Bethe-Bloch formula to estimate the energy loss rate, dE/dx, gives for argon at atmospheric pressure [63]

$$G = \frac{\rho_{Ar} \left.\frac{dE}{dX}\right|_{Ar}}{W_i} = 9700 \left[m^{-1} \right] \qquad (7.8)$$

with the argon ionisation energy W_i=26 [eV], the energy loss rate, dE/dX=1.52 [$MeVg^{-1}cm^{-2}$], the density of argon at 294 K and at atmospheric pressure, ρ_{Ar}=1.66 10^{-3} [gcm^{-3}]. Experimentally, the IC gain is determined as the SEC yield (see § 6.4.2) taking the gain as the ratio between the number of collected electrons, N_e and the number of incident particle, N_p,

$$G = \frac{N_e}{N_p} \qquad \text{with } N_e = \frac{VC_{int}}{1.6 \cdot 10^{-19}} \tag{7.9}$$

The uncertainties have already been discussed in chapter 6 (see §6.4.1). The results are presented in table 7.2. All the acquisitions were carried out at the SPS. The 3 upper points of table 7.2 (corresponding to the 3 higher incident intensities) have an IVC102 gain ~ 110 times larger than the other points. This was achieved by changing the value of C_{int} used during the tests. The measured absolute IC gain average value is 1064 ± 75. The yield is ~ 1600 larger compared to the monitor in SEC mode. As the IC active region is 11 cm long, the gain of the chamber is thus 9675 ± 677 [m^{-1}] in agreement with the predicted value of 9700 from equation 7.8.

In conclusion, with its present geometry and electronics, the monitor working in IC mode can be used to measure luminosity 3 orders of magnitude lower than in SEC mode.

Table 7.2 *Experimental determination of the IC gain*

Reference monitor	Average number of incident particles per burst, $\overline{N}$	Error on $\overline{N}$ [%] absolute+digits	Incident particles current [A]	IC response [V] ± σ_{tot}	IVC102 relative gain	IC gain [m^{-1}]
PIC	6.22 10^7	4	4 10^{-12}	1.21 ± 1%	110	10050 ± 5%
PIC	1.14 10^7	4+0.2	7 10^{-13}	0.22± 1%	110	10000 ± 5.2%
PIC/*SC*	2.28 10^6 / *2.27 10^6*	4+1 / *1*	1.4 10^{-13}	4.3 10^{-2}± 1%	110	10339 ± 6%
SC	*1.98 10^5*	*1*	1.6 10^{-14}	4.3 10^{-3}± 1%	1	9309 ± *2%*
SC	*9.3 10^4*	*1*	5.8 10^{-15}	2 10^{-3}± 1.1%	1	8673 ± *2%*

7.3 The IC as a LHC luminosity monitor

We have shown (see § 7.2) that the IC monitor is linear over the full experimental range of incident particles i.e. from ~9 10^4 to ~6 10^7 particles per SPS burst or from 5.8 10^{-15} A to 4 10^{-12} A. As the beam area is estimated to ~ 4 cm^2 during our tests, it leads to incident current densities of ~ 1.4 10^{-15} [Acm^{-2}] and 10^{-12} [Acm^{-2}] which correspond, respectively, to LHC luminosity between ~ 10^{30} $cm^{-2}s^{-1}$ and ~ 10^{33} $cm^{-2}s^{-1}$. With the actual electronics, we deduce from our tests that the IC could be used as a LHC luminosity monitor from 10^{28} $cm^{-2}s^{-1}$. At high intensity, the LHC radiation may activate the inner gas and distort the IC response[68]. IC should not be used as luminosity monitor at high intensities.

7.4 Transition from SEC to IC mode

Some runs were dedicated to the transition from SEC mode to IC mode allowing the observation of the evolution of the monitor gain with the internal pressure.
The SEC inner pressure is about 10^{-7} mbar. The transition is performed by progressively filling the SEC with argon. As soon as argon is injected inside the SEC, the detector becomes an IC. To avoid the deterioration of the external monitor window the maximum pressure reached is 800 mbar. The gain is proportional to the gas density (see equation 7.9) which is proportional to the pressure. Several scans in pressure have been carried out with consistent results. The results of one set of measurements taken at the PS are shown in figure 7.4. The uncertainty of the gain is determined as previously described while the pressure measurement has a systematic uncertainty of 10 %. The lower point reported on figure 7.4 corresponds to a pressure of 10±1 mbar. With the incident beam intensity of ~10^5 incident particles per PS burst, the signal was too weak to be measured for P<10 mbar. As expected the gain is linear with the internal pressure. The detector can be adjusted to a desired gain by choosing this parameter.
In our proposal, the monitor will be used in both ionisation and secondary emission modes. It will be calibrated at low LHC luminosity (~10^{28} $cm^{-2}s^{-1}$) by the TOTEM

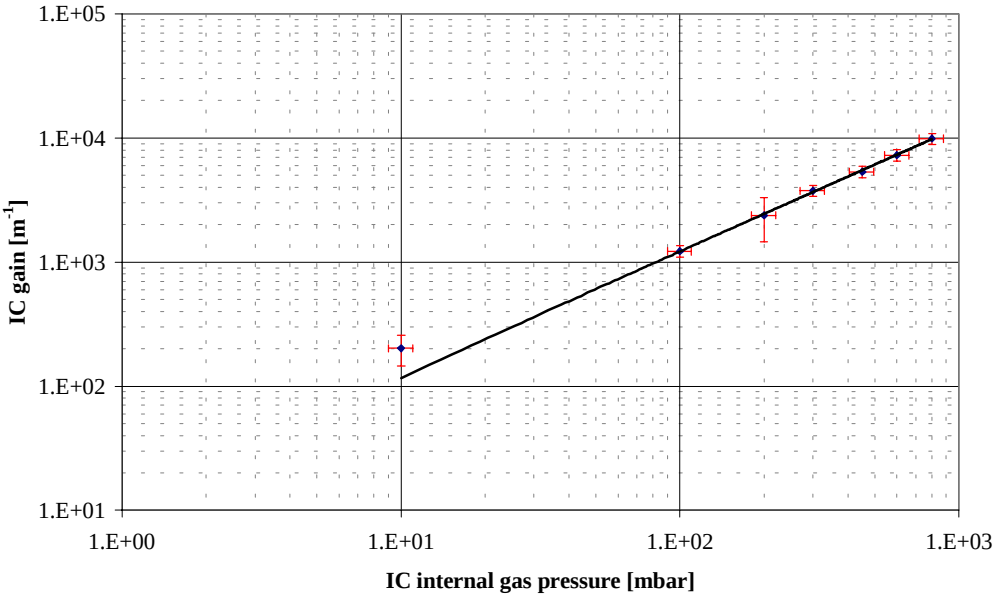

Figure 7.4 *Gain of the IC versus the internal pressure*

experiment (see §1.3.3). To extend the calibration's result to the full working range of the monitor, the continuity between the responses in IC mode and in SEC mode must be verified. Our experimental results ensure the linearity of the monitor in IC mode on all the tested range (i.e. from 9 10^4 to 6 10^7 incident particles per burst; see § 7.2) and above 2.7 10^6 incident particles per burst in SEC mode (see § 6.4). After correction for the IVC102 gain in IC and SEC mode and for the SEC yield and IC gain, the combined data are shown in figure 7.5.

The switch between IC and SEC mode is foreseen at L~ 10^{31} $cm^{-2}s^{-1}$ where a precision of ~ 3% for the SEC response is achieved within 1 s of integration. We should notice that at the LHC the pedestal subtraction will not be simple as during our tests. This is related to the bunches repartition around the LHC (i.e. the LHC beam structure along the orbit) which will be governed by the injection scheme. A period without collisions has to be found.

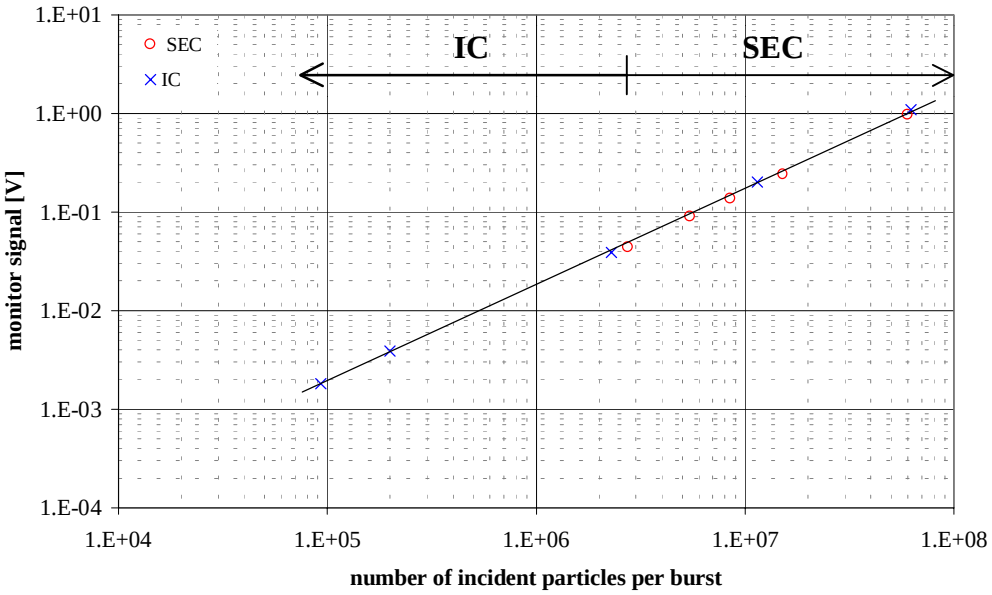

Figure 7.5 *Comparison between the SEC and the IC output signals after gain correction*

We propose the following calibration method at the LHC keeping in mind that the monitor response in SEC and IC modes is linear with the incident intensity. The monitor is calibrated at low luminosity (10^{28} $cm^{-2}s^{-1}$) when running in IC mode by the TOTEM experiment. It leads to the determination of the proportionality coefficient α_{IC}

$$V=\alpha_{IC}L+V_0$$

where V and V_0 are the monitor responses at the luminosity L and L=0, respectively. The monitor response in IC mode is then calculated for L=10 $^{31}cm^{-2}s^{-1}$. Its value is V_{31}. Then we increase the LHC intensity until $V=V_{31}$. At that moment the luminosity of the LHC is 10^{31} $cm^{-2}s^{-1}$, we switch the monitor from IC to SEC mode and determine the proportionality coefficient α_{SEC} The calibration of our luminosity monitor on all its dynamic range is thus achieved.

A summary of experimental results obtained for the monitor in IC and SEC modes is presented in table 7.3.

Table 7.3 *Summary of the experimental results for the monitor in IC and SEC modes*

Monitor mode	Beam line	Reference monitor	Average number of incident particles per burst, N	Error on N [%]	I_{incdt} [A]	I_{out} [A]	Monitor response [V]	σ_{tot} [%] for montor response
IC	SPS H6	PIC	$6.2\ 10^{7}$	4	$4\ 10^{-12}$	$4.25\ 10^{-9}$	1.21	1
IC	SPS H6	PIC	$1.1\ 10^{7}$	4.2	$7\ 10^{-13}$	$7.5\ 10^{-10}$	0.22	1
IC	SPS H6	SC	$2.2\ 10^{6}$	1	$1.4\ 10^{-13}$	$1.5\ 10^{-10}$	$4.3\ 10^{-2}$	1
IC	SPS H6	SC	$1.98\ 10^{5}$	1	$1.2\ 10^{-14}$	$1.3\ 10^{-11}$	$4.3\ 10^{-3}$	1
IC	SPS H6	SC	$9.25\ 10^{4}$	1	$5.8\ 10^{-15}$	$6\ 10^{-12}$	$2\ 10^{-3}$	1
SEC	SPS H6	PIC	$2.75\ 10^{6}$	4.8	$1.8\ 10^{-13}$	$1.2\ 10^{-13}$	$2.8\ 10^{-2}$	2.6
SEC	SPS H6	PIC	$5.43\ 10^{6}$	4.4	$3.5\ 10^{-13}$	$2.3\ 10^{-13}$	$5.9\ 10^{-2}$	1.5
SEC	SPS H6	PIC	$8.49\ 10^{6}$	4.2	$5.4\ 10^{-13}$	$3.6\ 10^{-13}$	$8.9\ 10^{-2}$	1.3
SEC	SPS H6	PIC	$1.5\ 10^{7}$	4.1	10^{-12}	$6.6\ 10^{-13}$	$1.5\ 10^{-1}$	1
SEC	SPS H6	PIC	$6\ 10^{7}$	4	$3.8\ 10^{-12}$	$2.5\ 10^{-12}$	$6.3\ 10^{-1}$	1

Conclusions and perspectives

The main challenge for a luminosity monitor at the LHC is a dynamic range of six orders of magnitude which extends from 10^{28} $cm^{-2}s^{-1}$ to 10^{34} $cm^{-2}s^{-1}$. The TOTEM collaboration has proposed to the CMS experiment to measure the luminosity within ~ 2% of uncertainty.

This work initially consisted in the evaluation of a luminosity monitor based on the concept of Secondary Emission Chamber (SEC), to be installed at ~19 meters from the Interaction Point 5 (IP5) surrounding the vacuum tube and covering the pseudo-rapidity range between 5 and 7. Our calculations have shown that to be efficient at such a position the SEC should be able to measure currents between about 10^{-15}A and 10^{-9}A. Tests with an existing SEC gave a detection threshold of about 10^{-12} A. New prototypes have been developed with the aim to improve this parameter by lowering the operational range. In particular, our goal was to minimise leakage currents and various sources of electronic noise.

The main upgrades are the addition of a ground insulated stainless steel cylinder inside the vacuum tank and the use of triaxial connections (see chapter 3). With this set-up the external tank acts as a Faraday cage isolating the electrodes from the external electromagnetic noise while the internal cylinder acts as a “floating” shield. In a recent prototype the insulation between consecutive electrodes was improved minimising the leakage current to a value lower than 10^{-15} A (see § 6.2.1), negligible in comparison to the input bias current of ~10^{-13} A of our electronics. The actual electronics is thus the main limitation of the SEC response.

The performances of the new SEC prototype were determined comparing its response with a reference detector. Tests were carried out at CERN on the PS and the SPS extraction beam lines with intensities ranging from 5 10^5 particles per burst to 6 10^7 particles per burst. The polarisation voltage is determined with a view to allow a complete collection of the charges. Experimental data obtained through “plateau” measurement confirm the prediction of a complete SEC collection for a polarisation above ~5 V (see § 6.1.3). Above ~ 3 10^6 incident particles per burst the SEC response is a

linear function of the number of incident particles within 1%. The secondary electron emission yield is defined as the ratio between the number of emitted secondary electrons and the number of incident particles on the SEC. It was measured to be (66 ± 4) %. At the LHC, we have shown that the SEC will be able to measure the luminosity with a precision of ~ 3 % for an integration time of 1 s, for luminosity above 10^{31} $cm^{-2}s^{-1}$.

A conversion of the SEC into an Ionisation Chamber (IC) is proposed to cover the LHC low luminosity region where the calibration will be done by TOTEM. We have transformed the SEC into IC by filling the chamber with argon at atmospheric pressure. The performances of the IC monitor have been determined in the similar experimental conditions as for the SEC. The minimum polarisation voltage allowing a complete collection of the positive ion-electron pairs created by ionisation was experimentally measured by a "plateau" technique and found to be in agreement with the theoretical predictions of a complete collection for 2.6 V at the SPS and 1.5 V at the PS. The ratio between the electric field due to the space charge and the initial one due to the polarisation voltage has been estimated for the maximum intensity used during all the tests i.e. 6 10^7 incident particles per burst. It is lower than 10 % for a polarisation voltage of 15 V. Space charge could lead to the recombination of some electrons and positive ions before they reach the collecting plates. It results in a loss of signal. Our calculations show that for a polarisation voltage above 5 V the recombination rate is always lower than 3 % in the experimental conditions and thus it can be neglected for all the data presented (see § 7.1.1). The IC response is also linear at the 1% level over the full experimental range of incident particles available i.e until 6 10^7 incident particles per burst. Its uncertainty during our tests is < 2%. The gain of the IC is defined as the number of ion-electron pairs created per particle crossing the detector. The absolute gain of the chamber is 1064 ± 75 which is ~1600 larger than for the monitor in SEC mode.

At high intensity, the LHC induced radiation may activate the inner gas which will result in the distortion of the IC response.

The working ranges of the SEC and the IC well overlap in such a way that a relative calibration can be achieved.

Some runs were dedicated to the transition from SEC to IC mode allowing the observation of the linear evolution of the monitor gain with its internal pressure.

In conclusion, for the LHC, we propose that TOTEM calibrates the monitor in IC mode at low intensity. After extrapolation of the response, the monitor can be used up to $L=10^{34}$ $cm^{-2}s^{-1}$ with a switch from IC to SEC mode at $L\sim10^{31}$ $cm^{-2}s^{-1}$. We expect a precision in the measure of the luminosity of ~ 3 % for an integration time of 1 s.

The integration of the monitor around the LHC machine and the optimisation of its geometry have to be studied. Two ideas are proposed. First we could surround the vacuum tube with SEC and IC monitors working independently from each other. Their responses might be collected simultaneously. Depending on the luminosity, the SEC or the IC response would be considered. Second we could use monitors working in IC mode at low luminosity and in SEC mode at high luminosity. On the other hand, in the future, electronics with lower noise will be perhaps available. In this case, new electronics should be developed and some of the present conclusions should be reconsidered.

Our SEC new prototype is actually used as a reference to replace progressively all the previous SECs installed for years around the PS machine at CERN.

Appendix A Collider luminosity formula

The centred normalised distribution density in a gaussian beam plane is

$$d(x,y) = d(x) \times d(y) = \frac{1}{\sigma_x \sqrt{2\pi}} e^{\frac{-x^2}{2\sigma_x^2}} \frac{1}{\sigma_y \sqrt{2\pi}} e^{\frac{-y^2}{2\sigma_y^2}} \quad (1)$$

In the case of the LHC, at the interaction point the beam will be circular such that $\sigma_x \sim \sigma_y \sim \sigma$ thus we can use polar coordinates. Equation 1 becomes

$$d(r,\varphi) = \frac{1}{2\pi\sigma^2} e^{\frac{-r^2}{2\sigma^2}} = d(r) \quad (2)$$

which depends only on the radial coordinate, r. Consider two beams, 1 and 2, crossing each other, their particle distributions density being, respectively, $d_1(r,\varphi)$ and $d_2(r,\varphi)$, the probability that one particle of beam 1 could interact with one particle of beam 2 is

$$P = \iint d_1(r,\varphi) d_2(r,\varphi) r d\varphi dr \quad (3)$$

Inserting equation 2 in equation 3 and considering N_1 particles per bunch for beam 1 and N_2 particles per bunch for beam 2 leads to the following expression P_{bunch} for the interaction probability of one bunch of beam 1 with one bunch of beam 2

$$P_{bunch} = \int_0^{\infty} \int_0^{2\pi} N_1 N_2 \frac{1}{4\pi^2\sigma^4} e^{\frac{-2r^2}{2\sigma^2}} r d\varphi dr = N_1 N_2 \frac{1}{4\pi\sigma^2} \int_0^{\infty} \frac{2r}{\sigma^2} e^{\frac{-r^2}{\sigma^2}} dr$$

thus

$$P_{bunch} = \frac{N_1 N_2}{4\pi\sigma^2} \quad (4)$$

Then the total luminosity, L_{tot}, at one interaction point will be

$$L_{tot} = P_{bunch} kf \tag{5}$$

with k the number of bunches in beams 1 and 2, f the revolution frequency. The rms size of the beam, σ, and the normalised emittance, ε_n, are related by

$$\sigma = \sqrt{\varepsilon\beta} \quad \text{and} \quad \varepsilon_n = \varepsilon\gamma \quad \text{i.e.} \quad \sigma = \sqrt{\frac{\varepsilon_n \beta}{\gamma}} \tag{6}$$

with β the betatron function and γ the relativistic factor (see chapter 2).This leads to the total luminosity

$$L_{tot} = \frac{N_1 N_2 \gamma k f}{4\pi\varepsilon_n \beta} \tag{7}$$

Assuming the number of particle per bunch is the same for the two beams $N_1=N_2=N$, equation 7 becomes

$$L_{tot} = \frac{N^2 \gamma k f}{4\pi\varepsilon_n \beta} \tag{8}$$

At the LHC the two beams will cross with an angle. This implies the correction of equation 8 by a factor F~0.9 related to the crossing angle of the beams. The luminosity formula for the LHC becomes

$$L_{tot} = \frac{N^2 \gamma k f}{4\pi\varepsilon_n \beta} F \tag{9}$$

Appendix B Effective beam height and Van der Meer method [21]

At the ISR collider, Van der Meer proposed to measure the effective beam height with a simple method that does not require any equipment mounted in the vacuum chamber. Once determined, the effective beam height allows the estimation of the absolute cross section. It permitted to measure the luminosity with an error of 0.3% [20]. Consider two beams, 1 and 2, with, respectively, N_1 and N_2 particles crossing each other. Their distribution densities as a function of the y coordinate are $S_1(y)$ and $S_2(y)$.They can be deduced by integration on x from the equation 1 in appendix A. Thus

$$N_1 = \int S_1(y)dy \quad \text{and} \quad N_2 = \int S_2(y)dy \tag{1}$$

The interaction probability L of the two beams is

$$L = \int S_1(y)S_2(y)dy \tag{2}$$

We define the effective height, h_{eff}, as

$$L = \frac{N_1 N_2}{h_{eff}} \tag{3}$$

Thus equations 2 and 3 leads to

$$\int S_1(y)S_2(y)dy = \frac{N_1 N_2}{h_{eff}} \tag{4}$$

Insertion of equation 1 in equation 4 gives

$$h_{eff} = \frac{\int dyS_1(y)\int dyS_2(y)}{\int dyS_1(y)S_2(y)} \tag{5}$$

The Van der Meer method [14,21] consists of displacing one of the two beams in the y direction with respect to the other one. Then, the counting rate R in a monitor, proportional to the rate of beam-beam collisions, is plotted versus the relative displacement of the beams, h.

$$R = B\int S_1(y)S_2(y-h)dy \tag{6}$$

where B is an unknown constant. It includes the interaction cross section and the acceptance of the counting monitor. Then the area, A, under the curve (see § 1.3.2 figure 1.4) is

$$A = \int [B\int S_1(y)S_2(y-h)dy]dh = B\int [S_1(y)\int S_2(y-h)dh]dy \tag{7}$$

and the rate R_0 for h=0 is

$$R_0 = B\int S_1(y)S_2(y)dy \tag{8}$$

Since the integrals are taken over the entire region where the integrands are not zero

$$\int S_2(y-h)dh = \int S_2(y)dy$$

and therefore dividing equation 7 by equation 8

$$\frac{A}{R_0} = \frac{B\int [S_1(y)\int S_2(y)dy]dy}{B\int S_1(y)S_2(y)dy} = \frac{\int S_1(y)y\int S_2(y)dy}{\int S_1(y)S_2(y)dy} \tag{9}$$

Comparing equations 5 and 9 leads finally to

$$h_{eff} = \frac{A}{R_0}$$

Appendix C The "luminosity independent method"

Before introducing the "luminosity independent method", the differential cross section of the elastic scattering in the centre of mass is determined. For an exhaustive demonstration and in particular the determination of the optical theorem, the reader should refer to the literature [69-72].

The differential cross section of the elastic scattering in the centre of mass

For the elastic scattering the differential cross section in the centre of mass at zero degree is

$$\left(\frac{d\sigma_{el}}{d\Omega^*}\right)_{\theta=0} = \left|f(0)\right|^2 = \left(\mathrm{Im}\, f(0)\right)^2 + \left(\mathrm{Re}\, f(0)\right)^2 \qquad (1)$$

where Im f(0) and Re f(0) are the imaginary and the real part of the forward elastic scattering, respectively.
Introducing in equation 1

$$\rho = \frac{\mathrm{Re}\, f(0)}{\mathrm{Im}\, f(0)} \qquad (2)$$

and using the optical theorem [69] standing that

$$\sigma_{tot} = \frac{4\pi}{p^*}\,\mathrm{Im}\, f(0) \qquad (3)$$

leads to

$$\left(\frac{d\sigma_{el}}{d\Omega^*}\right)_{\theta=0} = \left(1+\rho^2\right)\left(\mathrm{Im}\, f(0)\right)^2 = (1+\rho^2)\left(\frac{p^*\sigma_{tot}}{4\pi}\right)^2 \qquad (4)$$

where p* is the momentum in the centre of mass.
Changing to the differential cross section $d\sigma_{el}/dt$ defined as [72]

$$\frac{d\sigma_{el}}{dt} = \frac{\pi}{p^{*2}} \frac{d\sigma_{el}}{d\Omega^{*}} \tag{5}$$

where t is the 3-momentum transfert gives

$$\left(\frac{d\sigma_{el}}{dt} \right)_{t=0} = \frac{\sigma_{tot}^2}{16\pi} (1+\rho^2) \tag{6}$$

The "luminosity independent method"

This method is based on the simultaneous measurement of the elastic scattering at small angle and the total inelastic rate [10, 22]. The total cross section, σ_{tot}, and the integrated luminosity, L, of the machine are related by

$$N_{el}+N_{inel}=L\sigma_{tot} \tag{7}$$

where N_{el} and N_{inel} are the elastic and inelastic observed rates, respectively. By definition,

$$N_{el}=L\sigma_{el} \quad \text{thus} \quad \left(\frac{dN_{el}}{dt} \right)_{t=0} = L \left(\frac{d\sigma_{el}}{dt} \right)_{t=0} \tag{8}$$

Combining equations 6, 7 and 8 gives

$$\left(\frac{dN_{el}}{dt} \right)_{t=0} = (1+\rho^2)\ \sigma_{tot} \left(\frac{N_{el}+N_{inel}}{16\pi} \right) \tag{9}$$

The total cross section could thus be expressed as

$$\sigma_{tot} = \frac{16\pi}{(1+\rho^2)} \frac{\left(dN_{el}/dt\right)_{t=0}}{N_{el}+N_{inel}} \tag{10}$$

The TOTEM collaboration will measure with the “Roman pots system” dN_{el}/dt at small t and N_{el} whilst measuring N_{inel} with the forward inelastic detector (§ 1.1.3 see figure 1.2). The determination of the parameter ρ is more complex [74-86]. It is obtained by measuring the differential cross section, $d\sigma_{el}/dt$, in the region where strong and Coulomb interactions interfere. Elastic events are detected by a system of telescopes placed symmetrically on both sides of the interaction region. Knowing the proportionality between the observed elastic rate and the differential cross section, the data are then fitted using the theoretical form of $d\sigma/dt$. In this fit ρ is one of the free parameters. Its value is small at high energy, about 0.1-0.2, so that it has not to be known with high precision to get an accurate value of σ_{tot}. For the LHC, ρ is estimated to be ~0.14 [85]. Knowing ρ, N_{el}, N_{inel} and dN_{el}/dt leads through equation 10 to the total cross section, σ_{tot}, then through equation 7 to the integrated luminosity, L. This determination of the luminosity will be used to calibrate our future monitor at the LHC.

Appendix D Calculation of the density of incident particles on the first foil of the monitor

The calculation is based on the pseudorapidity distribution of charged particles. Note that pseudorapidity, η, expresses angles with the formula

$$\eta = -\ln \operatorname{tg}(\theta/2) \qquad (1)$$

where θ [rad] is the polar angle from the interaction point (IP) in the frame of the centre mass (see figure1). For the calculation, the pseudorapidity distribution of charged particles for non-single diffractive events at the LHC is used [10] (see figure 2).

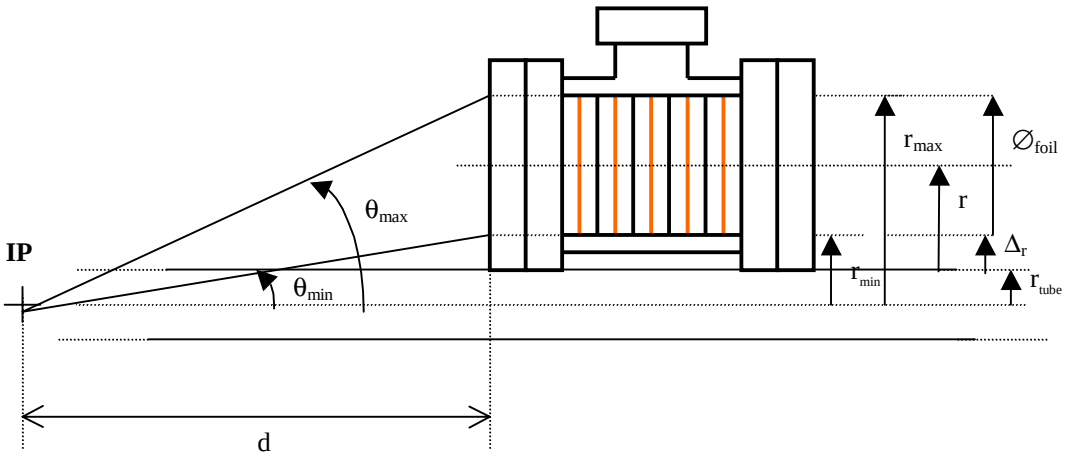

d=19 m

$r_{tube}=26\ 10^{-3}$ *[m]*

$r=11\ 10^{-2}$ *[m]*

$\varnothing_{foil}=122\ 10^{-3}$ *[m]*

r_{min}, r_{max}, θ_{min} *and* θ_{max} *: to be determined (see text hereafter)*

Figure 1 *Monitor layout sketch*

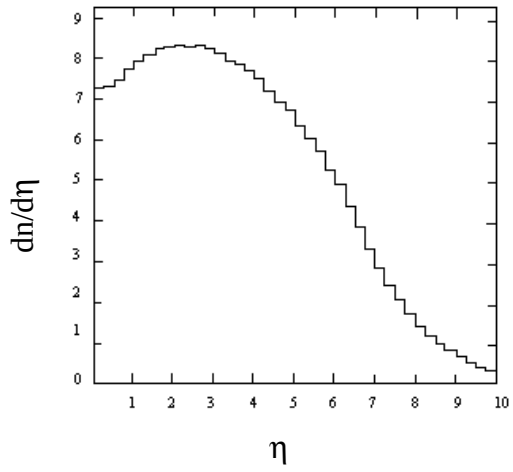

Figure 2 *Pseudorapidity distribution of charged particles for non-single diffractive events at the LHC from Monte-Carlo simulation at* $\sqrt{S} = 14\ TeV$ *.*[10]

The polar angle's range of charged particles incident on the first monitor foil is obtained from the following formula.

$r_{min} = r_{tube} + \Delta r$ and $r_{max} = r_{min} + \varnothing_{foil}$ with $\Delta r = r - (\varnothing_{foil}/2)$

$\sin\theta_{min} = r_{min}/d$ and $\sin\theta_{max} = r_{max}/d$

With the values of figure 1 it leads to r_{min}=7.5 10^{-2} [m], r_{max}=19.7 10^{-2} [m] and $\theta_{[rad]} \in$ [3.946 10^{-2}; 1.049 10^{-1}] which corresponds to the range of a pseudorapidity window $\eta \in$ [2.96; 3.93] using equation 1. Knowing from figure 2 that on 1 pseudorapidity unit centred at 2.96 the number of charged tracks is 8.27 while it is 7.72 on 1 unit pseudorapidity centred at 3.93, the average number of charged tracks per interaction is found to be 8.

To summarise:

$$\left.\begin{array}{l} \eta \in [2.96;3.93] \Rightarrow \Delta\eta \approx 1 \\ \langle dn/d\eta \rangle = 0.5(7.72 + 8.27) = 7.995 \cong 8 \end{array}\right\} \ \langle n \rangle \approx 8x1 = 8$$

with $\langle n \rangle$ the average number of charged tracks per interaction.

The average density $\langle d \rangle$ of charged tracks per interaction is given by

$$\langle d \rangle = \frac{\langle n \rangle}{A_f} \cong 0.068 \quad \text{tracks} \cdot \text{cm}^{-2} \tag{2}$$

where A_f, the foil area is 116.9 cm^2.

At the LHC maximum luminosity, L= 10^{34} $cm^{-2}s^{-1}$, the interaction rate is

$$dn/dt = L.\sigma_{tot} = 10^9 \text{ [interaction.s}^{-1}\text{]} \tag{3}$$

with σ_{tot}, the total cross section (at $\sqrt{S} = 14$ TeV σ_{tot}=100 mb). Thus the average density of charged tracks per unit time, $\langle \text{density per unit time} \rangle$ is estimated to be 6.84 10^7 particles.$cm^{-2}.s^{-1}$. At the LHC minimum luminosity, L= 10^{28} $cm^{-2}s^{-1}$, there are 10^3 interactions per second leading to an average density of charged tracks per unit time of 68.4 particles.$cm^{-2}s^{-1}$.

Finally the current, I, at the entrance of the monitor can be expressed as

$$I = \langle \text{density} \rangle A_f \text{ x1.6.10}^{-19} \tag{4}$$

Using the relation (4) and the precedent results it is found to be between 1.3 10^{-15} A and 1.3 10^{-9} A corresponding respectively to 10^{28} $cm^{-2}s^{-1}$ and 10^{34} $cm^{-2}s^{-1}$. If the monitor efficiency is ~1 then the input current at the entrance of the electronic is in the same range. The challenge is to measure 6 decades of intensity from a minimum corresponding to femto-amper currents.

Appendix E IVC102 specifications [87]

PARAMETER	CONDITIONS	IVC102P, U MIN	IVC102P, U TYP	IVC102P, U MAX	UNITS
TRANSFER FUNCTION			$Vo= -I_{in} xT_{int}/C_{int}$		
Gain error	$C_{int} = C_1 + C_2 + C_3$		-5	25/-17	%
vs Temperature			-25		ppm/°C
Nonlinearity	Vo = +-10 V		-0.005		%
Input Current Range	I_{in} = 0, C_{in} = 50 pF		-100		µA
Offset Voltage (2)			-5	-20	mV
vs Temperature	Vs = 4.75/-10 to 18/-18V		-30		µV/°C
vs Power Supply			150	750	µV/V
Droop Rate, Hold Mode			-1		nV/µs
OP AMP					
Input Bias Current	S_1, S_2 open		-100	-750	fA
vs Temperature			see typical curve		
Offset Voltage (Op Amp Vos)			-0.5	-5	mV
vs Temperature	Vs = 4.75/-10 to 18/-18V		-5		µV/°C
vs Power Supply	f = 1kHz		10	100	µV/V
Noise Voltage			10		$nV/(Hz)^{1/2}$
INTEGRATION CAPACITORS					
$C_1 + C_2 + C_3$		80	100	120	pF
vs Temperature			-25		ppm/°C
C_1			10		pF
C_2			30		pF
C_3			60		pF
OUTPUT					
Voltage Range, Positive	R_L = 2 kΩ	(V+)-3	(V+)-1.3		V
Negative	R_L = 2 kΩ	(V-)+3	(V-)+2.6		V
Short-Circuit Current			-20		mA
Capacitive Load Drive			500		pF
Noise Voltage			see typical curve		
DYNAMIC CHARACTERISTIC					
Op Amp Gain-Bandwidth			2		MHz
Op Amp Slew Rate			3		V/µs
Reset					
Slew Rate			3		V/µs
Setting time, 0.01%	10 V step		6		µs
POWER SUPPLY					
Voltage Range, Positive		4.75	15	18	V
Negative		-10	-15	-18	V
Current, Positive			4.1	5.5	mA
Negative			-1.6	-2.2	mA
Analog Ground			-0.2		mA
Digital Ground			-2.3		mA
TEMPERATURE RANGE					
Operating Range		-40		85	°C
Storage		-55		125	°C

NOTES:
(1) Standard test timing: 1ms integration, 200µs hold, 100 µs reset.
(2) Hold mode output voltage after 1 ms integration of zero input current. Includes op amp offset voltage, integration of input current and switch charge injection effects.

All these specifications are for IVC102 at 25 °C, Vs= +/- 15V, R_L= 2kΩ, $C_{int}=C_1+C_2+C_3$ 1 ms integration period (1), unless otherwise specified.

Appendix F AD650 specifications [88]

Model	AD650J/AD650A Min	Typ	Max	AD650K/AD650B Min	Typ	Max	AD650S Min	Typ	Max	Units
DYNAMIC PERFORMANCE										
Full Scale Frequency Range			1			1			1	MHz
Nonlinearity [1] f_{max} = 10 kHz		0.02	0.005		0.02	0.005		0.02	0.005	%
100 kHz		0.005	0.02		0.005	0.02		0.005	0.02	%
500 kHz		0.02	0.05		0.02	0.05		0.02	0.05	%
1 MHz		0.1			0.05	0.1		0.05	0.1	%
Full Scale Calibration Error [2], 100 kHz		-5			-5			-5		%
1MHz		-10			-10			-5		%
vs Supply[3]	-0.015		0.015	-0.015		0.015	-0.015		0.015	% of FSR/V
vs Temperature										
A,B, and S Grades										
at 10 KHz			-75			-75			-75	ppm/°C
at 100 KHz			-150			-150			-150	ppm/°C
J and K Grades										
at 10 KHz		-75			-75			-75		ppm/°C
at 100 KHz		-150			-150			-150		ppm/°C
BIPOLAR OFFSET CURRENT										
Activated by 24 kΩ between pins 4 and 5	0.45	0.5	0.55	0.45	0.5	0.55	0.45	0.5	0.55	mA
DYNAMIC RESPONSE										
Maximum Settling Time for Full Scale	1 pulse of new			1 pulse of new			1 pulse of new			
Step Input	Frequency Plus 1 µs			Frequency Plus 1 µs			Frequency Plus 1 µs			
Overload Recovery Time	1 pulse of new			1 pulse of new			1 pulse of new			
Step Input	Frequency Plus 1 µs			Frequency Plus 1 µs			Frequency Plus 1 µs			
ANALOG INPUT AMPLIFIER (V/Fconversion)										
Current Input Range	0		0.6	0		0.6	0		0.6	mA
Voltage Input Range	-10		0	-10		0	-10		0	V
Differential Impedance		2MΩ-10pF			2MΩ-10pF			2MΩ-10pF		
Common Mode Impedance		100MΩ-10pF			100MΩ-10pF			100MΩ-10pF		
Input Bias Current										
Noninverting Input		40	100		40	100		40	100	nA
Inverting Input		-8	-20		-8	-20		-8	-20	nA
Input Offset Voltage										
(Trimmable to Zero)			-4			-4			-4	mV
vs. Temperature (T_{min} to T_{max})		-30				-30			-30	µV/°C
Safe Input Voltage		V_s			V_s			V_s		C
COMPARATOR (F/V Conversion)										
Logic '0' level	- Vs		-1	- Vs		-1	- Vs		-1	V
Logic '1' level	0		Vs	0		Vs	0		Vs	V
Pulse Width Range[4]	0.1		$0.3xt_{OS}$	0.1		$0.3xt_{OS}$	0.1		$0.3xt_{OS}$	µs
Input Impedance		250			250			250		kΩ
AMPLIFIER OUTPUT (F/V Conversion)										
Voltage Range (1500Ω min load resistance)	0		10	0		10	0		10	V
Source Current (750Ω max load resistance)	10			10			10			mA
Capacitive load (Without oscillation)			100			100			100	pF
POWER SUPPLY										
Voltage, Rated Performance	-9		-18	-9		-18	-9		-18	V
Quiescent Current			8			8			8	mA
TEMPERATURE RANGE										
Rated Performance -N Package	0		70	0		70	0		70	°C
D Package	-25		85	-25		85	-25		85	°C
Storage -N Package	-25		85	-25		85	-25		85	°C
D Package	-65		150	-65		150	-65		150	°C

NOTES

[1] Nonlinearity is defined as deviation from a straight line from zero to full scale, expressed as a function of full scale.

[2] Full scale error ajustable to zero.

[3] Measured at full scale output frequency of 100 kHz.

[4] Refer to F/V conversion of the text.

[5] Refered to digital ground.

D=Ceramic DIP; N=Plastic DIP

All these specifications are for AD650 at 25°C with Vs=+/- 15V unless otherwise noted.

Appendix G Logic of the electronic circuit [89]

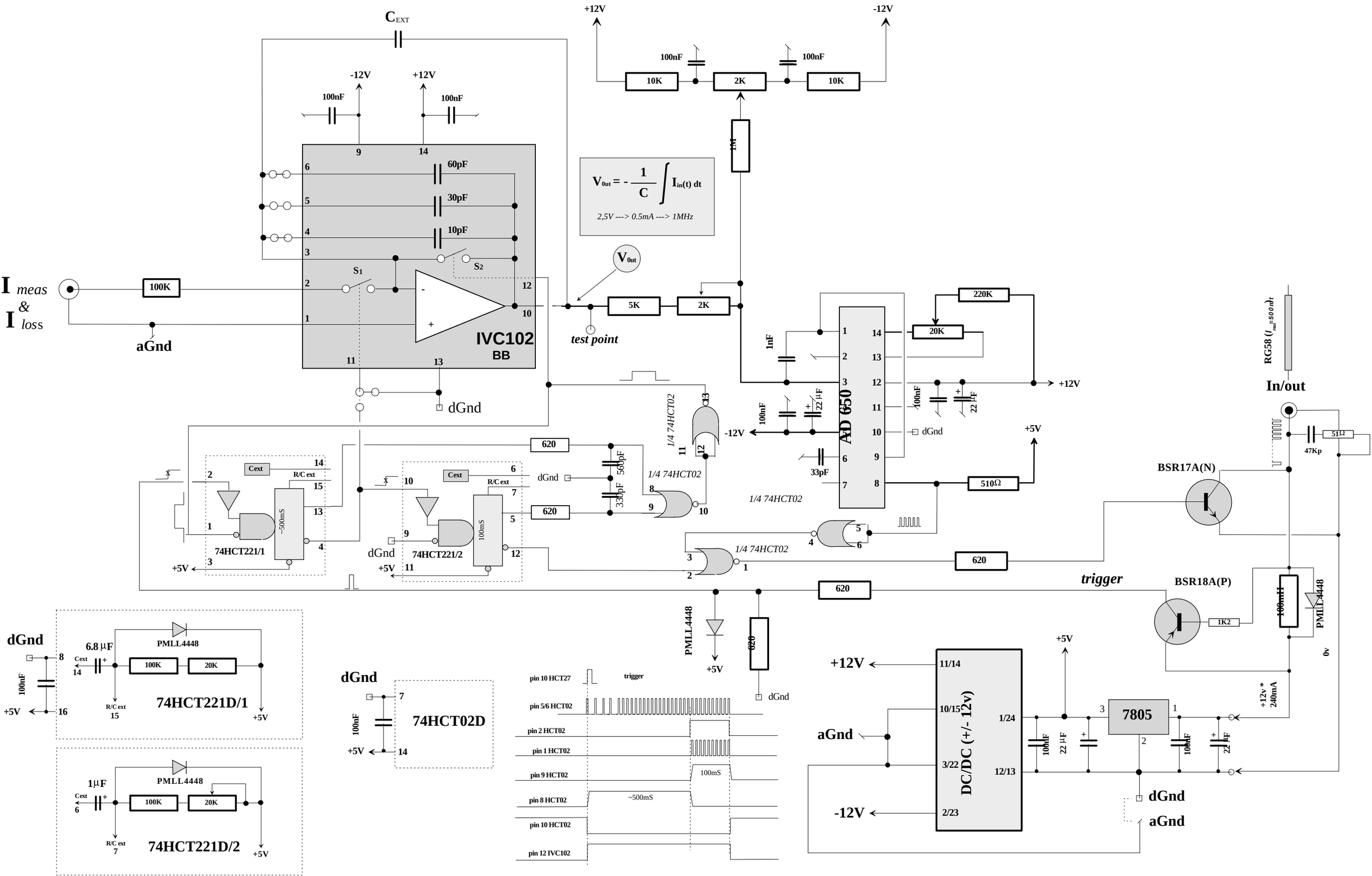

Appendix H The Langmuir and Child relation

Consider a simple layout with two parallel plates, the cathode and the anode [90]. The electrons are emitted from the cathode by heating for instance. The potential between the cathode and the anode may be changed. The density of the electrons, ρ, and the potential, V, at any point on the inter-electrodes space are related by the Poisson's equation

$$\frac{d^2V}{dx^2} = \frac{\rho(x)}{\varepsilon_0} \tag{1}$$

where V is in Volt, ρ in Cm^{-3} and ε_0, the permitivity of vacuum in $AsV^{-1}m^{-1}$. There is an explicit relation between the collected electrons current and the potential V. The electron current density, J, is a measure of the rate at which the electrons pass through the unit area per unit time in the direction of the field

$$J(x) = Nev = \rho(x)v \tag{2}$$

with J [$A\ m^{-2}$], N the electrons density [m^{-3}], e the electron charge [C] and v the electrons velocity [$m\ s^{-1}$]. For a zero initial velocity of the emitted electrons, their velocity, v, at any point of the inter-electrodes space is related to the potential by energy conservation

$$\frac{1}{2}mv^2 = eV \tag{3}$$

Combining the last three equations leads to

$$\frac{d^2V}{dx^2} = \frac{J}{\varepsilon_0}\sqrt{\frac{m}{2eV}} \tag{4}$$

Assuming $K = cst = -\frac{J\sqrt{m}}{\varepsilon_0\sqrt{2e}}$, V=y , $p = \frac{dy}{dx}$

gives $pdp = \frac{K}{\sqrt{y}}dy$ (5)

After integration and considering the boundary conditions [92] standing that for x=0, we have V=0 and $\frac{dV}{dx} = 0$, the solution of the differential equation (4) is

$$J = \frac{4\varepsilon_0}{9}\left(\frac{2e}{m}\right)^{1/2}\frac{V_0^{3/2}}{d^2} \quad (6)$$

with J the current density [A m^{-2}], ε_0 the vacuum permitivity [A s V^{-1} m^{-1}], e the electronic charge [C], m the electron mass [kg], V the applied voltage [V] and d the inter-electrodes distance [m]. For d in cm, J is expressed in Acm^{-2}. A numeric application gives

$$J = 2.34\cdot 10^{-6}\frac{V^{3/2}}{d^2} \quad (7)$$

known as **the Langmuir and Child relation**. It should be noted, however, that the derivation given depends upon the assumption that $\frac{dV}{dx} = 0$ at x=0. The expression gives results in good agreement with experiment[92].

This equation could be used to estimate the saturation threshold of the SEC. For a polarisation voltage of 5 V, knowing that the inter-electrodes distance is 5 mm, it leads to a current density, J, between two consecutive electrodes of ~10^{-4} Acm^{-2}. Assuming for the yield of the aluminium foil a value of ~7% [51], a polarisation of 5 V gives a saturation of the SEC for an incident current of ~10^{-3} A per unit area. The maximum intensities available at the PS and the SPS correspond to currents per unit area of 2 10^{-14} A and 5 10^{-14} A, respectively. These values are several orders of magnitude far below the estimated SEC saturation current. Thus no saturation of the SEC is expected during the tests at the PS and the SPS.

Appendix I Electric field in the ionisation chamber [65]

The electric field strength is supposed low enough to avoid gas amplification that might occur when the ionisation electrons gain enough energy to themselves produce ionisation. Below 1.5 $kVcm^{-1}$ it could be neglected for argon at atmospheric pressure.

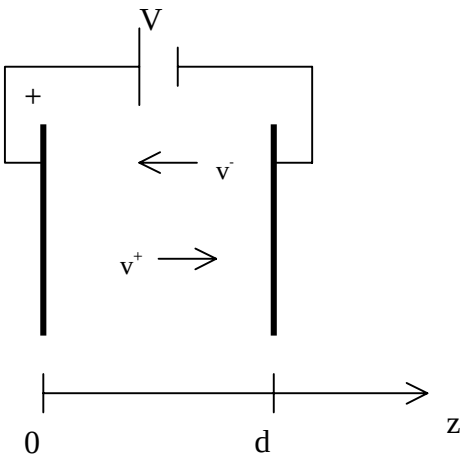

Figure 1. *Movement of the charges between two consecutive electrodes*

Consider two consecutive electrodes d apart (see figure 1). A polarisation voltage, V, is applied between the parallel plates. An incident particle between the electrodes creates along its path a number of ion-electron pairs proportional to its path length in the gas. The produced electrons and ions move toward the anode and the cathode, where they are respectively collected. For the derivation, the charge's migration direction is taken parallel to the z-axis. The electric field, E, between plates could be expressed from the Poisson equation

$$\frac{\partial^2 V}{\partial z^2} = -\frac{\rho}{\varepsilon_0} \quad \text{with} \quad E = -\frac{\partial V}{\partial z}$$

then

$$\frac{\partial E}{\partial z} = \frac{\rho}{\varepsilon_0} = \frac{1}{\varepsilon_0}(\rho_+ + \rho_-) \qquad (1)$$

where ε_o is the vacuum permitivity [$AsV^{-1}m^{-1}$], ρ_+, ρ_- and ρ stand, respectively, for the positive, negative and total charge densities between the plates [Cm^{-3}]. The continuity equations for the positive and negative charges, in a quasi steady state, assuming the charge densities low enough to neglect recombinations are

$$\frac{\partial \rho_+}{\partial z} = \frac{J}{v^+} \quad \text{and} \quad \frac{\partial \rho_-}{\partial z} = \frac{J}{v^-} \tag{2}$$

where J is the number of positive and negative charges created per unit time and unit volume [$Cs^{-1}m^{-3}$] and $v^{+/-}$ is the drift velocity [ms^{-1}] expressed as

$$v^{+/-} = k_{+/-}\frac{E}{P} \tag{3}$$

with $k_{+/-}$ the charge mobility [$m^2V^{-1}s^{-1}atm$] and P, the inner gas pressure [atm]. Combining the three last equations with P=1 atm leads to

$$\frac{\partial^2 E^2}{\partial z^2} = \frac{2J}{\varepsilon_0 k_r} \text{ with } k_r^{-1} = k_+^{-1} + k_-^{-1} \tag{4}$$

After successive integrations and with the boundary conditions that ρ^+ and ρ^- are, respectively, zero at the anode and at the cathode, the electric field is

$$E(z)^2 = \frac{J}{\varepsilon_0 k_r} z^2 + E_0^2 \qquad \text{with } E_0 = \frac{V}{d} \tag{5}$$

where E_0 is the electric field at the anode. This equation reveals that for low current density, J, the electric field is almost constant while for high J it is linear in z. The condition that all the positive and negative charges reach the collection plates before recombining is

$$E_0^2 \geq \frac{J}{\varepsilon_0 k_r} z^2 \qquad (6)$$

As the electrons mobility is higher than the positive ions mobility, it leads within a factor of 2 to the following criterion of a quasi complete collection of the created charges

$$d \leq 2\left(\frac{V}{d}\right)\sqrt{\frac{\varepsilon_0 k_+}{J}} \qquad (7)$$

The factor 2 is determined by a more rigorous mathematical derivation which is out of scope here [65]. The minimum polarisation voltage, V_{min}, in view to avoid recombination is thus

$$V_{min} = \frac{d^2}{2}\sqrt{\frac{J}{\varepsilon_0 k^+}} \qquad (8)$$

Bibliography

Chapter 1 Introduction to experimental environment

[1] cern web site ‘http://www.cern.ch/public’
[2] cern web site ‘http://www.lhc01.cern.ch/’
[3] The LHC study group, *Design Study of the Large Hadron Collider (LHC)*, CERN 91-03, p1, 1991.
[4] F. Ruggiero, *A review of new manifestations of collective effects*, CERN SL-98-032.
[5] cern web site ‘http://www.cern.ch’
[6] The LHC study group, *LHC Conceptual Design*, CERN/AC/95-05 (LHC), p5-6, p43, 1995.
[7] CMS collaboration, *CMS Technical proposal*, CERN/LHCC 94-38, LHCC/P1, p1, 1994.
[8] web site ‘http://cmsinfo.cern.ch’
[9] CMS collaboration, *CMS Technical design report*, CERN/LHCC 97-33, CMS TDR4, pC21.
[10] The TOTEM collaboration, *Letter of intent*, CERN/LHCC 97-49, LHCC/I11, p1, p30-31, fig.1 p9, fig.14 p32.
[11] The TOTEM collaboration, *Technical proposal*, CERN/LHCC 99-7, LHCC/P5, p3-5, fig.17 p26, 1999.
[12] Eur. Phys. J. C3, 1-794, Springer-Verlag, p138, 1998.
[13] K. Piotrzkowski, *Experimental aspects of the luminosity measurement in the Zeus experiment*, internal report DESY F 35D–93-06, 1993.
[14] K. Potter, *Luminosity measurements and calculations*, Proc. Of the CERN accelerator school, vol. I, CERN 94-01, p117-127, 1994.
[15] T. Suzuki, *General formulas of the luminosity for various types of colliding beam machines*, KEK-76-3, 1976.
[16] Private discussion with G. Molinari, CERN-PS/BD, 1998.
[17] D. Decamp et al., ALEPH collaboration, Zeit. f. Phys. C53, p376, 1992.
[18] G. Arison et al., UA1 collaboration, Phys. Lett. B128, p336, 1983.
[19] S. White et al., *CDF collaboration, Measurement of the antiproton-proton total cross-section at* $s^{1/2}$*=1800GeV*, Fermilab–Conf. 91-268-E, 1991.
[20] C. Carboni et al., Nucl. Phys. B254, p697, 1985.
[21] S. van der Meer, *Calibration of the effective beam height in the ISR*, CERN-ISR-PO/68-31, 1968.
[22] M. Bozzo et al, *Measurement of the proton-antiproton total and elastic cross-sections at the CERN SPS collider*, Phys. Lett. 147B, p392, 1984.
[23] Cohen-Tannoudji, Quantum mechanics, vol II, chap. VIII, p940-945, Hermann, 1992.
[24] D. H. Perkins, *Introduction to the high energy physics*, 2nd edition, p138.
[25] A. Bay, *course on “Réactions nucléaires”*, Université de Lausanne, IPHE, 1997
[26] Rapport préliminaire de sûreté du LHC, 1999.
[27] CMS collaboration, *CMS technical proposal*, CERN/LHCC 97-32, pC14.
[28] CMS collaboration, *CMS technical design report*, CERN/LHCC 97-33, pC22.

[29] Report on I5 telescope – November 1974, ISR-OP/FL/svw
[30] F. Lemeilleur, *ISR standard monitors – status report*, ISR-op/fl/sw.
[31] E. Rossa and G. von Holtey, *Compteurs de luminosité*, SPS/ELE/Note 82-9.
[32] J. – Y. Hémery, F. Lemeilleur, R. Olsen and K. Potter, *Background and luminosity monitoring at the CERN ISR*, CERN-ISR-OP-CO-ES/81-12.

Chapter 2 General characteristics of accelerators and detectors

[33] E. J. N. Wilson, *Series of lectures on introduction to the physics of accelerators*, Joint Universities Accelerators School (JUAS), 1996.
[34] H. Koziol, *Some physics aspects of beam diagnostics*, CERN-PE-ED-001-92 (revised Nov. 1994), p87-89.
[35] L. Vos, *Understanding accelerators*, CERN-PE-ED-001-92 (revised Nov. 1994), p22-23.
[36] W. R. Leo, *Techniques for Nuclear and particle physics experiments*, Spring-Verlag, chap.2, p107-118.
[37] W. R. Leo, *Techniques for Nuclear and particle physics experiments*, Spring-Verlag, chap.6, p119-127.

Chapter 3 Ionisation Chamber and Secondary Emission Chamber

[36] W. R. Leo, *Techniques for Nuclear and particle physics experiments*, Spring-Verlag, chap.2, p107-118.
[37] W. R. Leo, *Techniques for Nuclear and particle physics experiments*, Spring-Verlag, chap.6, p119-127.
[38] J.-F. Loude, *Cours sur les détecteurs de particules ionisantes*, section physique, faculté des sciences, université de Lausanne, ed. 1993, chap3.
[39] M.-T. Trân, *Cours sur les détecteurs de particules*, section physique, faculté des sciences, université de Lausanne, 1997-1998, chap3
[40] K. Kleinknecht, *Detectors for particle radiation*, Cambridge University Press, chaps.1 and 2.
[41] Dr Minh-Tâm Trân, *Cours sur les détecteurs de particules*, Université de Lausanne, IPHE, 1997-1998, chap.2.
[42] V. Agoritsas, *Secondary Emission Chambers for monitoring the CPS ejected beams*, Symposium on beam intensity measurement, Daresbury, proceedings edited by V. W. Hatton and S.A. Lowndes, DNPL/R1, 22-26 April 1968.
[43] V. Agoritsas and R. L. Witkover, *Tests of SEC stability in high flux proton beams*, IEEE Transactions on Nuclear Science, vol. NS-26 No 3, June 1979.
[44] G. W. Tautfest and H.R. Fechter, *A nonsaturable high-energy beam monitor*, Rev. Sci. Instrum. Vol. 26, p229, 1955.
[45] The encyclopedia of physics, 2nd ed., edited by Robert M. Besançon, Van Nostrand Reinhold Company, p825.
[46] J. Arianer, *Cours sur les sources de particules chargées*, D.E.A. Physique et technologie des grands instruments in2p3, 1997.
[47] Miroslav Sedlacek, *Electron physics of vacuum and gaseous devices, secondary emission*, chap2, p70

[48] E. Mercier, *Mesure de la distribution en énergie des électrons secondaires pour le LHC*, rapport de stage, CERN, LHC/VAC-SL, juin 1999, p18,.
[49] D. H. Perkins, *Introduction to high energy physics*, Addison-Wesley, 2nd ed., chap.2.
[50] E. J. Sternglass, *Theory of secondary electron emission by high speed ions*, Phys. Rev. second series, vol. 108, no 1, oct.1957.
[51] G. Ferioli, R. Jung, *Evolution of the Secondary Emission Efficiencies of various materials measured in the CERN SPS secondary beam lines*, CERN-SL-97-71 (BI), 1997.
[52] private communication with M. Huhtinen.

Chapter 4 Experimental set-up

[53] D.J. Simon, L. Durieu et al, *Secondary beams for tests in the PS east Experimental area*, PS/PA-EP note 88-26, revised 25.1.93, p5-11
[54] http://cern.web.cern.ch/CERN/Divisions/PS/PSComplex/CERNAcc.html
[55] http://padata.web.cern.ch/psdata/www/eastareaop/index.htlm
[56] http://cern.web.cern.ch/CERN/division/Psreports/PA9321/figures/Fig27.gif
D.J. Simon, L. Durieu et al, *Secondary beams for tests in the PS east Experimental area*, PS/PA-EP note 88-26
[57] http://nicewww.cern.ch/sl/eagroup/eahome.html
[58] K. Elsener, M. Heilmann and M. Silari, *Verification of the calibration factor of the CERF beam monitor*, TIS-RP/TM/98-22, August 1998.
[59] http://sl.web.ch/SL/eagroup/synoptic.html
[60] Drawing by Gimenez, *TIS-RP-H6-H8.dwg*
[61] KEITHLEY, *CTM-10 and CTM-05/A User's guide*, revision B, August 1996, p1-1

Chapter 6 performances of the SEC monitor

[50] E. J. Sternglass, *Theory of secondary electron emission by high speed ions*, Phys. Rev. second series, vol. 108, no 1, oct.1957.
[51] G. Ferioli, R. Jung, *Evolution of the Secondary Emission Efficiencies of various materials measured in the CERN SPS secondary beam lines*, CERN-SL-97-71 (BI), 1997.
[62] *Particle induced electrons emission secondary*, Springer in modern physics, volume 122
[63] W.C. Turner, *A neutral beam absorber beam-beam centering and luminosity monitor for the high luminosity insertions of the LHC*, Lawrence Berkeley National Laboratory, CPB note 251, &3.2
[64] The LHC study group, *LHC Conceptual Design*, CERN/AC/95-05 (LHC), 1995, p168

Chapter 7 The ionisation chamber mode

[38] J.-F. Loude, *Cours sur les détecteurs de particules ionisantes*, section physique, faculté des sciences, université de Lausanne, ed. 1993, chap3.

[63] W.C. Turner, *A neutral beam absorber beam-beam centering and luminosity monitor for the high luminosity insertions of the LHC*, Lawrence Berkeley National Laboratory, CPB note 251, &3.2

[65] W.C. Turner, *A neutral beam absorber beam-beam centering and luminosity monitor for the high luminosity insertions of the LHC*, Lawrence Berkeley National Laboratory, CPB note 251, appendix B

[66] J.W. Boag and T. Wilson, *The saturation curve at high ionisation intensity*, Brit. J. of App. Phys., 3, 222 (1952)

[67] F. Sauli, *Principles of operation of multiwire proportional and drift chambers*, CERN 77-09, p19

[68] Private communication with P. Carbonez, CERN/TIS radioprotection group

[91] William H. Press, William T. Vetterling, Saul A. Teukolsky and Brian P. Flannery, *Numerical Recipes in C, the Art of Scientific Computing*, 2nd edition, Cambridge University Press, chap.13

Appendix C The "luminosity independent method"

[69] D. H. Perkins, *Introduction to high energy physics*, 2nd edition, 1982, Addison-Wesley publishing company, p138-141

[70] Martin, L. Perl, *High energy hadron physics*, a Wiley–Interscience publication, John Wiley & Sons, NY, chap.6

[71] C. Cohen-Tannoudji, B. Diu, F. Laloë, *Mécanique quantique*, Hermann, éditeur des sciences, 1993, tome II, chap.8 p893-926 et complément B_{VIII} p940-945

[72] A. Bay, *cours sur la théorie de la diffusion*, section physique, faculté des sciences, université de Lausanne, 1999.

[73] Martin, L. Perl, *High energy hadron physics*, New York Wiley, Ed. 1974, p8-19

[74] G. G. Beznogikh et al., *Small angle proton-proton elastic scattering from 9 to 70 GeV/c*, Phys. Letters 39B (1972) 411

[75] U. Amaldi et al., *Measurement of the proton-proton cross section by means of Coulomb scattering at the CERN intersecting storage rings*, Phys. Letters 43B (1973) 231

[76] V. Bartenev et al., *Real part of the proton-proton forward scattering amplitude from 50 to 400 GeV*, Pys. Rev. Letters 31 (1973) 1367

[77] U. Amaldi et al., *The real part of the forward proton-proton scattering amplitude measured at the CERN intersecting storage rings*, Phys. Letters 66B (1977) 390

[78] M. Bozzo et al., UA4 collaboration, *Measurement of the proton-antiproton total and elastic cross sections at the CERN SPS collider*, Phys. Letters 147B (1984) 392

[79] N. Amos et al., *Measurement of small angle antiproton-proton and proton-proton elastic scattering at the CERN intersecting storage rings*, Nuclear Physics B262 (1985) 689

[80] D. Bernard et al., UA4 collaboration, *The real part of the proton-antiproton elastic scattering amplitude at the centre of mass energy of 546 GeV*, Phys, Letters B198 (1987) 583

[81] N. A. Amos et al., E710 collaboration, *A luminosity independent measurement of the* $\bar{p}p$ *total cross section at* $\sqrt{s}$ *=1.8 TeV,* Phys. Letters B243 (1990) 158

[82] C. Augier et al., UA4/2 collaboration, *Predictions on the total cross section and real part at LHC and SSC,* Phys, Letters B315 (1993) 503

[83] C. Augier et al., UA4/2 collaboration, *A precise measurement of the real part of the elastic scattering amplitude at the S* $\bar{p}p$ *S,* Phys, Letters B316 (1993) 448

[84] G. Matthiae, *Hadron-nucleon cross sections at high energy,* ROM2F/94/04

[85] TOTEM collaboration, *Letter of intent,* CERN/LHCC 97-49, LHCC/I11, chap. 2 p10-20, fig.4 p 14

[86] N. Mâu Chung, Sections efficaces de production de γ directs dans les interactions $\bar{p}p$ et pp à $\sqrt{s}$ =24.3 GeV et le couplage fort α_s, Thèse de doctorat présentée à la Faculté des Sciences de l'Université de Lausanne, 1998

Appendix D Calculation of the density of incident particles on the first foil of the monitor

[10] The TOTEM collaboration, *Letter of intent*, CERN/LHCC 97-49, LHCC/I11, fig.14 p32.

Appendix E IVC102 specifications

[87] Burr-Brown catalogue, *Precision switched integrator transimpedance amplifier IVC102,* 1996

Appendix F AD650 specifications

[88] ANALOG DEVICES catalogue, *Voltage-to-Frequency and frequency-to-Voltage Converter AD650,* 3-15

Appendix G Logic of the electronic circuit

[89] G. Molinari, *Sec_al.dsf,* CERN- PS/BD 1998

Appendix H The Langmuir and Child relation

[90] S. Seely, *Electron tube circuits,* Mc Graw-Hill electrical and electronic engineering series, Mc Graw-Hill book Company, inc. 1950, chap.2

Appendix J Electric field in the ionisation chamber

[65] W.C. Turner, *A neutral beam absorber beam-beam centering and luminosity monitor for the high luminosity insertions of the LHC*, Lawrence Berkeley National Laboratory, CPB note 251, §3.2 and appendix B

List of figures

List of tables

List of photos

Acknowledgments

This work has been carried out in a collaboration between the Institut de Physique des Hautes Energies (IPHE) of the Lausanne University and the European organisation for nuclear research (CERN) though the doctorate student program.

I wish to express my thanks to Prof. Aurelio Bay (IPHE, University of Lausanne), my thesis director and to Dr. Sylvain Weisz, my supervisor at CERN for their helpful advices and discussions throughout the course of this work. I would also like to thank Keith Potter, CERN/EST-LEA group leader, and Werner Kienzle of the TOTEM collaboration for giving me the opportunity to follow a research project at CERN and for their encouragement and stimulation during these three years.

I am specially grateful to Gianni Molinari (CERN/PS-BD) for his friendly collaboration, for his explanations and his helpful work on the Secondary Emission Chambers and Ionisation Chambers. I would like to thank for many useful suggestions, interesting discussions and ideas on my work Jacques Bosser (CERN/PS-BD) as well as all the CERN/PS-BD team for its assistance and help in the construction, setting-up and performance tests of the monitor.

A special thanks to Erika Luthi (IPHE, University of Lausanne) for her kindness and help during these three years.